

Computational Aeroacoustic Prediction of Propeller Noise  
Using Grid-Based and Grid-Free CFD Methods

by

**Jason Hambrey, BAsc.**

A thesis submitted to the Faculty of Graduate and Postdoctoral Affairs in partial fulfillment of the requirements for the degree of

**Master of Applied Science**

in

Ottawa-Carleton Institute for Mechanical and Aerospace Engineering

Carleton University  
Ottawa, Ontario

© 2016, Jason Hambrey

## **Abstract**

Two CFD codes are used to simulate noise data for a tandem cylinder experiment and two scaled NASA SR-2 propeller tests. The first code, STAR CCM+, is a grid-based commercial CFD code while the second code, SmartRotor, is an in-house grid-free CFD code which uses a panel method coupled with a discrete vortex method. Good comparison to experiment is achieved, with STAR CCM+ predicting the vortex shedding of the tandem cylinder case within 3 Hz and 10 dB while also predicting first propeller harmonics within 20 and 11 dB for the first and second propeller simulations, respectively. SmartRotor predicted first propeller harmonics within 6 and 37 dB for the first and second experiments, respectively. A parametric study on the influence of blade count on propeller noise was then performed using both codes to simulating the noise of 7-, 8-, and 10-bladed propellers finding quieter operation with increasing blade count.

## **Acknowledgements**

I would like to thank Professor Daniel Feszty for his support throughout this project and for the many stories shared along the way. I would also like to thank Dr. Sid-Ali Meslioui and Dr. Jong Park at Pratt and Whitney Canada for their time and support in shaping and completing this project. Finally, I would also like to extend thanks to David Boots for his work in the parallelization of SmartRotor and making it simpler to use – much time has been saved as a result!

This work was financially supported by a research grant provided by Pratt & Whitney Canada and the Green Aviation Research and Development Network (GARDN).

# Table of Contents

<b>Abstract.....</b>	i
<b>Acknowledgements .....</b>	ii
<b>Table of Contents .....</b>	iii
<b>List of Tables .....</b>	vi
<b>List of Figures.....</b>	viii
<b>List of Appendices.....</b>	xii
<b>List of Symbols .....</b>	xiii
<b>List of Abbreviations .....</b>	xv
<b>Chapter 1: Introduction .....</b>	1
<b>    1.1    Motivation.....</b>	1
<b>    1.2    Literature Review .....</b>	3
1.2.1    Historical Evolution of Propeller Research .....	3
1.2.2    Development of Computational Noise Models for Propellers .....	4
1.2.3    Propeller Noise Sources .....	5
1.2.4    Impact of Design Parameters on Propeller Noise.....	6
<b>    1.3    Experimental and CFD Studies on Propeller Aeroacoustics .....</b>	13
<b>    1.4    Research Objectives.....</b>	16
<b>    1.5    Approach .....</b>	18
<b>Chapter 2: Test Cases Selected for Validation.....</b>	19
<b>    2.1    Tandem Cylinder Test Case.....</b>	20
<b>    2.2    Propeller Test Case 1: SR-2 Propeller in Low Speed Condition .....</b>	23
<b>    2.3    Propeller Test Case 2: SR-2 Propeller in Cruise Condition .....</b>	25
<b>    2.4    Using Wind Tunnel Data to Validate Propeller Aeroacoustic Simulations ..</b>	27
<b>Chapter 3: Numerical Methods .....</b>	31
<b>    3.1    The STAR CCM+ Code .....</b>	32
3.1.1    Numerical Modeling of Aerodynamics in STAR CCM+.....	32
3.1.1.1    Governing Equations of Motion .....	32
3.1.1.2    Turbulence Modeling.....	34
3.1.1.2.1    Reynolds Averaged Navier-Stokes Equations .....	35
3.1.1.2.2    Detached Eddy Simulation.....	36
3.1.2    Discretization and Solver Properties .....	37
3.1.3    Solver Stability Characteristics .....	40
3.1.4    Numerical Modeling of Aeroacoustics in STAR CCM+ .....	42
3.1.4.1    Direct Methods .....	42
3.1.4.2    Indirect Methods.....	42
3.1.5    Grid Generation in STAR CCM+.....	47
3.1.5.1    Trimmed Mesh.....	47

3.1.5.2	Polyhedral Mesher .....	48
3.1.5.3	Prism Layer Mesher.....	49
3.1.5.4	Grid Extruder .....	50
3.1.6	Sliding Mesh Method .....	51
<b>3.2</b>	<b>Overview of SmartRotor Code .....</b>	<b>51</b>
3.2.1	Code Background .....	52
3.2.2	Numerical Modeling of Aerodynamics in SmartRotor .....	53
3.2.2.1	Brief Overview of Panel Method.....	54
3.2.2.2	Overview of the Free Vortex Method.....	58
3.2.3	Numerical Modeling of Aeroacoustics in SmartRotor .....	60
3.2.4	Limitations of SmartRotor Code .....	60
<b>3.3</b>	<b>Impact of Simulation Properties on Aeroacoustic Prediction .....</b>	<b>61</b>
<b>3.4</b>	<b>Computational Facilities Utilized .....</b>	<b>62</b>
<b>Chapter 4: Tandem Cylinder Test Case .....</b>	<b>64</b>	
<b>4.1</b>	<b>Simulation Setup .....</b>	<b>64</b>
4.1.1	Boundary Conditions and Grid Generation .....	64
4.1.2	Solver Selection and Simulation Properties .....	67
<b>4.2</b>	<b>Convergence Criteria.....</b>	<b>68</b>
<b>4.3</b>	<b>Verification .....</b>	<b>68</b>
<b>4.4</b>	<b>Validation.....</b>	<b>71</b>
4.4.1	Average Pressure Coefficient Results .....	71
4.4.2	Noise Emission Results .....	74
<b>4.5</b>	<b>Chapter Summary .....</b>	<b>77</b>
<b>Chapter 5: Aeroacoustic Validation of SR-2 Propeller in Low Speed Condition....</b>	<b>78</b>	
<b>5.1</b>	<b>STAR CCM+ Simulation Setup.....</b>	<b>78</b>
5.1.1	Boundary Conditions and Grid Design .....	78
5.1.2	Solver Selection and Simulation Properties .....	82
5.1.3	Convergence Criteria.....	83
5.1.4	Verification.....	83
<b>5.2</b>	<b>SmartRotor Simulation Setup .....</b>	<b>85</b>
5.2.1	Convergence Criteria.....	86
5.2.2	Verification.....	87
<b>5.3</b>	<b>Results Validation .....</b>	<b>87</b>
5.3.1	Aerodynamic Results.....	87
5.3.2	Aeroacoustic Results .....	88
<b>5.4</b>	<b>Chapter Summary .....</b>	<b>95</b>
<b>Chapter 6: Aerodynamic and Aeroacoustic Validation of SR-2 Propeller in Cruise Conditions.....</b>	<b>96</b>	
<b>6.1</b>	<b>STAR CCM+ Simulation Setup.....</b>	<b>96</b>
6.1.1	Boundary Conditions and Grid Generation .....	96
6.1.2	Selection of Blade Pitch Angles .....	99
6.1.3	Solver Selection and Simulation Properties .....	99

6.1.4	Convergence Criteria.....	100
6.1.5	Verification.....	101
<b>6.2</b>	<b>SmartRotor Simulation Setup .....</b>	<b>102</b>
6.2.1	Convergence Criteria.....	103
6.2.2	Verification.....	103
<b>6.3</b>	<b>Validation of CFD Results .....</b>	<b>104</b>
6.3.1	Aerodynamic Results.....	104
6.3.2	Aeroacoustic Results .....	104
<b>6.4</b>	<b>Chapter Summary .....</b>	<b>112</b>
<b>Chapter 7: Parametric Study on the Impact of Blade Count on Propeller Noise...</b>		<b>113</b>
<b>7.1</b>	<b>Background .....</b>	<b>113</b>
<b>7.2</b>	<b>Parametric Study Setup .....</b>	<b>115</b>
<b>7.3</b>	<b>Selection of Blade Pitch Angles.....</b>	<b>117</b>
<b>7.4</b>	<b>STAR CCM+ Simulation Setup.....</b>	<b>117</b>
7.4.1	Boundary Conditions and Grid Design .....	117
7.4.2	STAR CCM+ Solver Selection and Simulation Properties .....	119
<b>7.5</b>	<b>SmartRotor Simulation Setup .....</b>	<b>120</b>
<b>7.6</b>	<b>Results of Parametric Study .....</b>	<b>121</b>
<b>Chapter 8: Conclusions and Recommendations for Future Work .....</b>		<b>128</b>
<b>8.1</b>	<b>STAR CCM+ Code Validation .....</b>	<b>128</b>
<b>8.2</b>	<b>SmartRotor Code Validation .....</b>	<b>129</b>
<b>8.3</b>	<b>Parametric Study Results.....</b>	<b>131</b>
<b>8.4</b>	<b>Feasibility of Using the Codes for Propeller of Propeller Noise .....</b>	<b>131</b>
<b>8.5</b>	<b>Recommendations for Future Work .....</b>	<b>132</b>
<b>References .....</b>		<b>134</b>
<b>Appendix A: Geometry Definition Used for SR-2 Propeller in SmartRotor Code.</b>		<b>141</b>
<b>Appendix B: SR-2 Validation Data for SR-2 Test Case 2 .....</b>		<b>142</b>

## List of Tables

Table 1.1: Published Experiments on Propeller Aeroacoustics .....	14
Table 1.2: Propeller Information for Available Experiments on Propeller Aeroacoustics	15
Table 1.3: Aerodynamic and Aeroacoustic Simulations of Propeller Noise Validated by Experiment.....	16
Table 2.1: List of Potential Experiments for Validation Cases .....	20
Table 2.2: Experiment Conditions for SR-2 Test Case 1.....	23
Table 2.3: Experiment Conditions for SR-2 Test Case 2.....	26
Table 2.4: Unique Acoustic Adjustments Performed by De Gennaro et al. [52] .....	28
Table 3.1: Computational Platforms Utilized for Simulations .....	63
Table 4.1: Boundary Conditions of Tandem Cylinder Test Case .....	65
Table 4.2: Grid Properties for Tandem Cylinder Test Case .....	66
Table 4.3: Refinement Regions of Overset Grid .....	66
Table 4.4: Solver Properties for Tandem Cylinder Test Case .....	67
Table 4.5: Simulation Properties for Tandem Cylinder Test Case .....	67
Table 4.6: Verification Studies for Tandem Cylinder Test Case .....	69
Table 4.7: Peak frequencies and magnitudes for tandem cylinder test case .....	77
Table 5.1: Boundary Conditions for SR-2 Test Case 1 .....	80
Table 5.2: General Grid Properties for SR-2 Test Case 1.....	81
Table 5.3: Refinement Regions of Grid for SR-2 Test Case 1 .....	81
Table 5.4: Grid Extrusion Parameters for SR-2 Test Case 1 .....	81
Table 5.5: Solver Properties for SR-2 Test Case 1 .....	82
Table 5.6: Simulation Properties for SR-2 Test Case 1 .....	82
Table 5.7: Verification of Boundary Layer Thickness and Refinement .....	84
Table 5.8: SmartRotor Simulation Properties for SR-2 Test Case 1 .....	86
Table 5.9: SmartRotor Verification Results for SR-2 Test Case 1 .....	87
Table 5.10: Aerodynamic Results for SR-2 Test Case 1 .....	87
Table 5.11: Blade Passage Frequency Noise Predictions for SR-2 Test Case 1 .....	89
Table 6.1: Boundary Conditions for SR-2 Test Case 2 .....	98
Table 6.2: General Grid Properties for SR-2 Test Case 2.....	98
Table 6.3: Refinement Regions of Grid for SR-2 Test Case 2 .....	98
Table 6.4: Grid Extrusion Parameters for SR-2 Test Case 2 .....	99
Table 6.5: Comparison of Predicted Thrust and Torque for Periodic and Full Size Simulations .....	99
Table 6.6: Solver Properties for SR-2 Test Case 2 .....	100
Table 6.7: Simulation Properties for SR-2 Test Case 2 .....	100
Table 6.8: Verification of Boundary Layer Thickness and Refinement .....	102
Table 6.9: SmartRotor Simulation Properties for SR-2 Test Case 2 .....	103
Table 6.10: SmartRotor Verification Results for SR-2 Test Case 1 .....	103
Table 6.11: Aerodynamic Results for SR-2 Test Case 2 .....	104
Table 6.12: Blade Passage Frequency Noise Predictions for SR-2 Test Case 2.....	106
Table 7.1: Simulation Conditions for Propeller Blade Count Study .....	116
Table 7.2: Pitch angles used for blade count study.....	117
Table 7.3: Grid Sizes for Blade Count Parametric Study .....	118
Table 7.4: Simulation Properties for Blade Count Parametric Study .....	120
Table 7.5: SmartRotor Simulation Properties for Blade Count Parametric Study .....	120

Table 7.6: Aerodynamic Results for Blade Count Parametric Studies .....	121
Table 7.7: Total Noise in dB at BPFs for 7-, 8-, and 10- Bladed Propellers .....	123
Table A.1: Geometrical Inputs of SR-2 Propeller Into SmartRotor .....	141

# List of Figures

Fig. 1.1: ICAO measurement points for certification of aircraft [3]. The measurement locations are indicated by letters A-C.....	2
Fig. 1.2: Noise level requirements for commercial aircraft from ICAO Annex 16 [3]....	3
Fig. 1.3: Example plot from literature showing propeller noise data captured at a pressure transducer for two different free stream speeds [12].....	6
Fig. 1.4: A visualization of blade thickness, with a relatively thin (left) and thick propeller (right).....	8
Fig. 1.5: An unswept (left) and swept (right) propeller.....	9
Fig. 1.6: Noise reduction due to sweep for an 8 bladed propfan at a cruise speed of 0.8 Mach [1].....	10
Fig. 1.7: A standard propeller (left) compared to a propeller with offset (right).....	11
Fig. 1.8: A propeller without twist (left) compared to a propeller with twist (right).....	12
Fig. 1.9: A propeller without taper (left) compared to a propeller with taper (right).....	12
Fig. 2.1: Instantaneous spanwise vorticity of tandem cylinder experiment [60].....	21
Fig. 2.2: Experiment setup of tandem cylinder test case [73].....	22
Fig. 2.3: Experimental apparatus at BART (left) [61] and QFF (right) [63] .....	22
Fig. 2.4: SR-2 Propeller Geometry, describing (a) spanwise distribution of chord (b), twist ( $\beta_0$ ), thickness (t), diameter (d), and design lift coefficient ( $C_l$ ) [12].....	24
Fig. 2.5: Planform view of 622 mm diameter SR-2 Propeller Blade [57], with dimensions in mm.....	24
Fig. 2.6: Transducer locations relative to the propeller hub, with a description of the plan view (left) and the plane containing the propeller looking downstream (right) [12].....	25
Fig. 2.7: Experimental apparatus and transducer locations for SR-2 Test Case 2 [15] ...	26
Fig. 3.1: An illustration of a V-cycle of a Multigrid Solver with 4 Grid Levels [103]. ...	39
Fig. 3.2: The effect of the quadrupole noise term at transonic speeds [96].....	45
Fig. 3.3: An example of a trimmed grid with different regions of refinement.....	48
Fig. 3.4: An example of a polyhedral grid around the blade of a propeller.....	49
Fig. 3.5: A prism grid alongside a boundary showing the development of a velocity boundary layer.....	50
Fig. 3.6: An example of grid extrusion.....	51
Fig. 3.7: Panels Generated on an SR-2 Propeller [57].....	57
Fig. 4.1: Computational domain and boundary conditions of tandem cylinder case.....	65
Fig. 4.2: A planar cut of the entire grid showing refinement regions A and B.....	66
Fig. 4.3: Grid refinement around cylinders showing refinement regions B, C, D, and E. ....	67
Fig. 4.4: Average $C_p$ values of upstream cylinder for verification simulations.....	69
Fig. 4.5: Average $C_p$ values of downstream cylinder for verification simulations.....	70
Fig. 4.6: Power spectral density values for pressure probe at $\theta = 135^\circ$ on upstream cylinder for verification simulations.....	70
Fig. 4.7: Power spectral density values for pressure probe at $\theta = 45^\circ$ on downstream cylinder for verification simulations.....	71
Fig. 4.8: Instantaneous density contours of tandem cylinder test case.....	72
Fig. 4.9: Average pressure coefficient values of upstream cylinder.....	73
Fig. 4.10: Average pressure coefficient values of downstream cylinder.....	73
Fig. 4.11: Location of pressure probes where pressure spectra were calculated.....	74

Fig. 4.12: Gauge pressure-time history for the upstream cylinder.....	74
Fig. 4.13: Gauge pressure-time history for the downstream cylinder.....	75
Fig. 4.14: Power spectral density values for pressure probe at $\theta = 135^\circ$ on upstream cylinder .....	76
Fig. 4.15: Power spectral density values for pressure probe at $\theta = 45^\circ$ on downstream cylinder .....	76
Fig. 5.1: Regions in computational domain for SR-2 Test Case 1.....	79
Fig. 5.2: Front view of the domain boundaries for SR-2 Test Case 1.....	79
Fig. 5.3: Side view of grid for SR-2 Test Case 1.....	79
Fig. 5.4: Grid around SR-2 propeller for Test Case 1.....	80
Fig. 5.5: Convergence of thrust and torque values with grid size for steady state simulations.....	84
Fig. 5.6: Thrust and torque convergence plotted against iteration in SmartRotor.....	86
Fig. 5.7: Wind tunnel data measured at transducer 7 (from [12]).....	88
Fig. 5.8: Gauge pressure time history at transducer 12 predicted by an impermeable FW-H surface in STAR CCM+. Time period of revolution: 0.073 s. ....	91
Fig. 5.9: Gauge pressure time history at transducer 12 predicted by a permeable FW-H surface in STAR CCM+. Time period of revolution: 0.073 s. ....	91
Fig. 5.10: Gauge pressure time history at transducer 12 predicted by SmartRotor. Time period of revolution: 0.073 s. ....	91
Fig. 5.11: Noise at transducer 7 predicted in STAR CCM+ from an impermeable FW-H surface.....	92
Fig. 5.12: Noise at transducer 7 predicted in STAR CCM+ from a permeable FW-H surface.....	92
Fig. 5.13: Noise at transducer 7 predicted in SmartRotor.....	93
Fig. 5.14: Noise at transducer 12 predicted in STAR CCM+ from an impermeable FW-H surface.....	93
Fig. 5.15: Noise at transducer 12 predicted in STAR CCM+ from a permeable FW-H surface.....	94
Fig. 5.16: Noise at transducer 12 predicted in SmartRotor.....	94
Fig. 6.1: Grid around SR-2 Propeller for Test Case 2. ....	97
Fig. 6.2: Convergence of thrust and torque values with grid size for steady state simulations.....	101
Fig. 6.3: Noise at transducer 2 predicted in STAR CCM+ from an impermeable FW-H surface.....	107
Fig. 6.4: Noise at transducer 2 predicted in STAR CCM+ from a permeable FW-H surface.....	107
Fig. 6.5: Noise at transducer 2 predicted in SmartRotor.....	108
Fig. 6.6: Noise at transducer 6 predicted in STAR CCM+ from an impermeable FW-H surface.....	108
Fig. 6.7: Noise at transducer 6 predicted in STAR CCM+ from a permeable FW-H surface.....	109
Fig. 6.8: Noise at transducer 6 predicted in SmartRotor.....	109
Fig. 6.9: Noise at transducer 12 predicted in STAR CCM+ from an impermeable FW-H surface.....	110

Fig. 6.10: Noise at transducer 12 predicted in STAR CCM+ from a permeable FW-H surface .....	110
Fig. 6.11: Noise at transducer 12 predicted in SmartRotor.....	111
Fig. 6.12: A polar plot of the first harmonic at the microphone locations around the propeller, located at the origin .....	111
Fig. 7.1: Propeller sound pressure levels with varying number of blades (B) and rotational mach tip number ( $M_T$ ) for an 8 foot diameter propeller [13].....	113
Fig. 7.2: Equal level loudness contours showing the sensitivity of the human ear [127]. .....	114
Fig. 7.3: Propellers studied in blade number study.....	116
Fig. 7.4: Transducer locations for parametric study, all located $16D$ from the propeller. .....	116
Fig. 7.5: Grid generated for 7-bladed (left) and 10-bladed (right) Propeller .....	118
Figure 7.6: Grid refinement study for 8-bladed propeller used in parametric study. ....	119
Fig. 7.7: Noise predicted at transducer 13 in STAR CCM+ (left) and SmartRotor (right) for 7-Bladed Propeller.....	124
Fig. 7.8: Noise predicted at transducer 15 in STAR CCM+ (left) and SmartRotor (right) for 7-Bladed Propeller.....	124
Fig. 7.9: Noise predicted at transducer 17 in STAR CCM+ (left) and SmartRotor (right) for 7-Bladed Propeller.....	124
Fig. 7.10: Noise predicted at transducer 13 in STAR CCM+ (left) and SmartRotor (right) for 8-Bladed Propeller.....	125
Fig. 7.11: Noise predicted at transducer 15 in STAR CCM+ (left) and SmartRotor (right) for 8-Bladed Propeller.....	125
Fig. 7.12: Noise predicted at transducer 17 in STAR CCM+ (left) and SmartRotor (right) for 8-Bladed Propeller.....	125
Fig. 7.13: Noise predicted at transducer 13 in STAR CCM+ (left) and SmartRotor (right) for 10-Bladed Propeller.....	126
Fig. 7.14: Noise predicted at transducer 15 in STAR CCM+ (left) and SmartRotor (right) for 10-Bladed Propeller.....	126
Fig. 7.15: Noise predicted at transducer 17 in STAR CCM+ (left) and SmartRotor (right) for 10-Bladed Propeller.....	126
Fig. 7.16: Predicted directivity of first harmonic of 7-Bladed Propeller.....	127
Fig. 7.17: Predicted directivity of first harmonic of 8-Bladed Propeller.....	127
Fig. 7.18: Predicted directivity of first harmonic of 10-Bladed Propeller.....	127
Fig. B.1: Noise at transducer 3 predicted in STAR CCM+ from an impermeable FW-H surface .....	142
Fig. B.2: Noise at transducer 3 predicted in STAR CCM+ from a permeable FW-H surface.....	142
Fig. B.3: Noise at transducer 3 predicted in SmartRotor.....	143
Fig. B.4: Noise at transducer 4 predicted in STAR CCM+ from an impermeable FW-H surface .....	143
Fig. B.5: Noise at transducer 4 predicted in STAR CCM+ from a permeable FW-H surface.....	144
Fig. B.6: Noise at transducer 4 predicted in SmartRotor.....	144

Fig. B.7: Noise at transducer 5 predicted in STAR CCM+ from an impermeable FW-H surface .....	145
Fig. B.8: Noise at transducer 5 predicted in STAR CCM+ from a permeable FW-H surface .....	145
Fig. B.9: Noise at transducer 5 predicted in SmartRotor .....	146
Fig. B.10: Noise at transducer 7 predicted in STAR CCM+ from an impermeable FW-H surface .....	146
Fig. B.11: Noise at transducer 7 predicted in STAR CCM+ from a permeable FW-H surface .....	147
Fig. B.12: Noise at transducer 7 predicted in SmartRotor .....	147
Fig. B.13: Noise at transducer 8 predicted in STAR CCM+ from an impermeable FW-H surface .....	148
Fig. B.14: Noise at transducer 8 predicted in STAR CCM+ from a permeable FW-H surface .....	148
Fig. B.15: Noise at transducer 8 predicted in SmartRotor .....	149
Fig. B.16: Noise at transducer 9 predicted in STAR CCM+ from an impermeable FW-H surface .....	149
Fig. B.17: Noise at transducer 9 predicted in STAR CCM+ from a permeable FW-H surface .....	150
Fig. B.18: Noise at transducer 9 predicted in SmartRotor .....	150
Fig. B.19: Noise at transducer 10 predicted in STAR CCM+ from an impermeable FW-H surface .....	151
Fig. B.20: Noise at transducer 10 predicted in STAR CCM+ from a permeable FW-H surface .....	151
Fig. B.21: Noise at transducer 10 predicted in SmartRotor .....	152
Fig. B.22: Noise at transducer 11 predicted in STAR CCM+ from an impermeable FW-H surface .....	152
Fig. B.23: Noise at transducer 11 predicted in STAR CCM+ from a permeable FW-H surface .....	153
Fig. B.24: Noise at transducer 11 predicted in SmartRotor .....	153
Fig. C.1: Lift (Top Left), Drag (Top Right), and Moment (Bottom) Coefficient Curves for the NACA 65-(-2.2) 20 Airfoil .....	154
Fig. C.2: Lift (Top Left), Drag (Top Right), and Moment (Bottom) Coefficient Curves for the NACA 65-(-2) 15 Airfoil .....	155
Fig. C.3: Lift (Top Left), Drag (Top Right), and Moment (Bottom) Coefficient Curves for the NACA 65-010 Airfoil .....	156
Fig. C.4: Lift (Top Left), Drag (Top Right), and Moment (Bottom) Coefficient Curves for the NACA 65-107 Airfoil .....	157
Fig. C.5: Lift (Top Left), Drag (Top Right), and Moment (Bottom) Coefficient Curves for the NACA 16-105 Airfoil .....	158
Fig. C.6: Lift (Top Left), Drag (Top Right), and Moment (Bottom) Coefficient Curves for the NACA 16-203 Airfoil .....	159
Fig. C.7: Lift (Top Left), Drag (Top Right), and Moment (Bottom) Coefficient Curves for the NACA 16-102 Airfoil .....	160
Fig. C.8: Lift (Top Left), Drag (Top Right), and Moment (Bottom) Coefficient Curves for the NACA 16-002 Airfoil .....	161

## **List of Appendices**

Appendix A: Geometry Definition Used for SR-2 Propeller in SmartRotor Code.....	141
Appendix B: SR-2 Validation Data for Test Case 2.....	142
Appendix C: Airfoil Data Used for Aerodynamic Input in SmartRotor.....	154

## List of Symbols

Bold typeface indicates a vector or matrix quantity.

$c_0$	Speed of sound
$C_p$	Pressure Coefficient
$[C_{ij}^{lifting}]$	Influence coefficient matrix for lifting body elements
$[C_{ik}^{near wake}]$	Influence coefficient matrix for lifting body elements
$[C_{il}^{non-lifting}]$	Influence coefficient matrix for lifting body elements
$D$	Diameter
$\overleftrightarrow{D}$	Deformation Tensor
$D_\omega$	Domain of far wake calculations
dB	Decibel
$d\tilde{\alpha}$	Differential surface area
$f$	Function describing a Ffowcs Williams-Hawkins surface
$f_r$	Force due to rotation
$f_g$	Gravitational force
$f_p$	Porous media force
$f_u$	User defined body force
$f_\omega$	Vorticity confinement specific force
$f_L$	Lorentz or Laplace force
$E$	Total energy per unit mass
H	Total enthalpy
$H_b$	Vector of body forces
$H(f)$	Heaviside Function
$I$	Identity Matrix
$k$	Turbulent Kinetic Energy
$l$	Local force on the fluid per unit area
$M$	Mach number
$N$	Number of panels on a specified surface
$n$	Surface Normal Vector
$p$	Pressure
$p_0$	Far field pressure
$p'(\bar{x}, t)$	Total far-field pressure in Ffowcs Williams-Hawkins Equation
$p'_T(\bar{x}, t)$	Thickness pressure term
$p'_L(\bar{x}, t)$	Loading pressure term
$p'_Q(\bar{x}, t)$	Quadrupole pressure term
$p'$	Fluctuating pressure
$P$	Point in velocity field
$\dot{q}''$	Heat flux vector
$\tilde{r}$	Distance from a given element to the evaluation point
$S$	Mean stress rate tensor
$S_u$	Mass or energy source term

$t$	Time
$T$	Temperature
$\mathbf{T}_v$	Viscous stress tensor
$\mathbf{T}_t$	Reynolds stress tensor
$\mathbf{T}_L$	Lighthill stress tensor
$\mathbf{u}$	Velocity of the fluid
$\mathbf{u}_{ref}$	Free stream velocity
$\mathbf{u}_g$	The grid velocity vector
$\mathbf{u}''$	Fluctuating component of velocity
$\tilde{\mathbf{u}}$	Mean velocity in RANS Equations
$\mathbf{u}_{ext}$	External velocity field in Helmholtz decomposition
$\mathbf{u}_{far-wake}$	Far wake velocity field in Helmholtz decomposition
$\mathbf{u}_{near-wake}$	Near wake velocity field in Helmholtz decomposition
$\mathbf{u}_{solid}$	Velocity field created by the interference of bodies on an external flow
$U$	Velocity magnitude of a fluid particle
$\mathbf{v}$	Surface velocity in in the $x_i$ direction
$\tilde{V}$	Control volume
$\mathbf{x}$	Cartesian spatial coordianate
$\mathbf{z}_j$	Position of a given vortex particle j
$\delta$	Dirac delta function
$\varepsilon$	Cut-off length of vortex particles
$\theta$	Angular position around cylinder
$\Delta t$	Time step
$\Delta x_i$	Spatial distance across a cell in a given dimension $i$
$\mu$	Dipole Intensity
$\rho$	Density
$\rho_0$	Far field density
$\mu_t$	Eddy Viscosity
$\sigma$	Source Intensity
$\tau$	Stress tensor
$\phi$	Velocity Potential
$\Psi$	Vector streamfunction
$\omega$	Vorticity
$\Omega_j$	Vorticity of a given vortex particle j

## List of Abbreviations

AMG	Algebraic Multi Grid
CAA	Computational Aeroacoustics
CFD	Computational Fluid Dynamics
CFL	Courant-Friedrich-Lowy
DES	Direct Eddy Simulation
EPNdB	Effective Perceived Noise [dB]
FW-H	Ffowcs Williams and Hawking
HPCVL	High Performance Computing Virtual Laboratory
ICAO	International Civil Aviation Organization
LES	Large Eddy Simulation
OASPL	Overall Sound Pressure Level
RANS	Reynolds Averaged Navier Stokes Equations
Re	Reynolds Number
SPL	Sound Pressure Level
SST	Shear Stress Transport

# **Chapter 1: Introduction**

A driving factor in the design of modern aircraft is the acoustic signature of the aircraft, driven both by international standards as well as noise considerations for both passengers and city residents. This is especially true for propeller aircraft, for which the propeller is known to be a major source of noise. A combination of computing advances and numerical techniques has recently allowed advanced Computational Aeroacoustics (CAA) models to be a useful design tool to predict propeller noise at the design stage. The research presented in this thesis aimed to examine the feasibility of Computational Fluid Dynamics (CFD) for predicting the aeroacoustic signature of a propeller in two different flight regimes. Two methods, the grid-based STAR CCM+ as well as the grid-free SmartRotor code were utilized to predict the aerodynamic and aeroacoustic performance of a scaled SR-2 propeller, for which experimental data were available from the literature. The confidence built in the codes allowed them to be utilized for performing a parametric study on the influence of blade count on propeller noise.

## **1.1 Motivation**

Propellers are a set of rotating blades which convert rotational motion to a propulsive thrust force. They do so by inducing a pressure difference between the two sides of the propeller disc, resulting in thrust. As they induce a relatively small amount of velocity to a large volume of air, propellers operate at high efficiency until flight speeds of about 0.65 Mach [1], with advanced propeller design enabling efficient operation up to cruise speeds of 0.8 Mach [2]. At these speeds the efficiency of propellers can be significantly higher than that of turbofans or turbojets and consequently their utilization is of

continued interest for subsonic aircraft in a competitive industry with increasing fuel costs.

Aircraft equipped with propulsion units consisting of a propeller driven by a gas turbine engine are termed as turboprop aircraft. Although they are popular for short-haul flights, an impediment to the use of turboprop engines is the noise generated by the propeller. Quiet operation is desired in order to ensure passenger comfort in the cabin as well as to conform to increasingly strict international noise standards. The International Civil Aviation Organization (ICAO) sets international standard noise level requirements for aircraft manufacturers, with noise measurement points set at the approach before landing, on the runway (sideline), and the takeoff point. These measurement points are illustrated in Fig. 1.1 below.

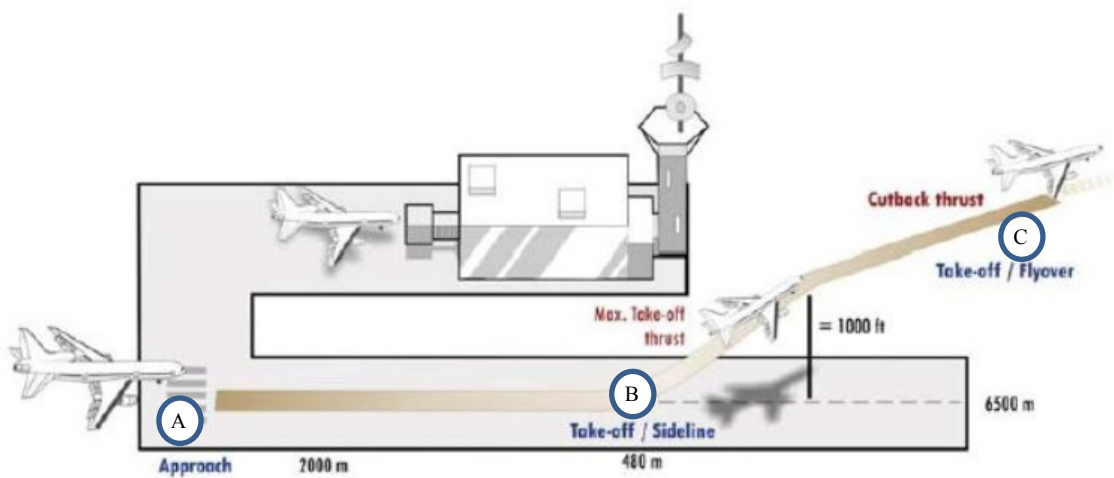


**Fig. 1.1: ICAO measurement points for certification of aircraft [3]. The measurement locations are indicated by letters A-C.**

The ICAO standards have continuously reduced acceptable levels of noise generated by aircraft, with ICAO Annex 16 establishing Chapter 14 to come into effect in 2017. As can be seen from Fig. 1.2, Chapter 14 requires a significant decrease in effective perceived noise (EPNdB) from Chapter 4, which is currently in effect. As a result, noise reduction for aircraft is particularly important and understanding the prediction tools and utilizing them to predict noise in new designs is essential.

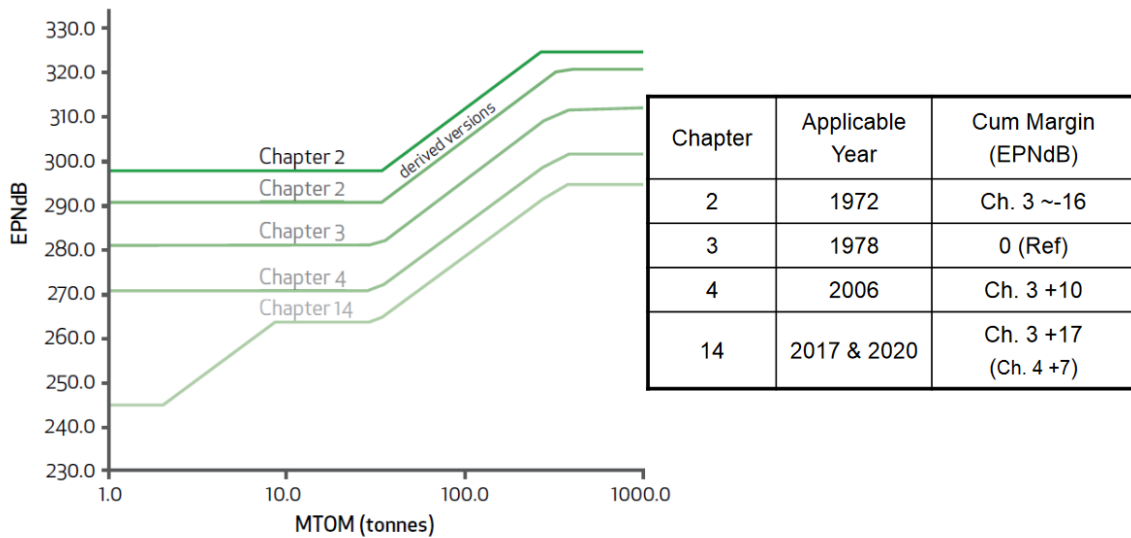


**Fig. 1.2: Noise level requirements for commercial aircraft from ICAO Annex 16 [3].**

## 1.2 Literature Review

### 1.2.1 Historical Evolution of Propeller Research

Propellers have been used as a primary method for aerospace propulsion since they were first employed by the Wright brothers in 1903. By the 1920s, the aerodynamics of propeller design was well developed, as seen in publications on propeller efficiency such as early as Technical Report 481 published in 1928 by the National Advisory Committee for Aeronautics (NACA) [4]. Between 1927 to the mid-1950s, NACA was at the head of

extensive propeller research, alongside industry and military efforts, resulting in the advent of many efficient turboprop engines [2]. Propeller research slowed between the 1950s and 1970s as turbojet and turbofan engines became the focus of research because of their efficient flight at higher speeds and high altitude operation. However, as fuel costs rose in the 1970s, a demand for more efficient operation resulted in the study of advanced high-speed propellers, leading to designs such as counter-rotating propfans [2].

Significant experimental testing was performed by NASA as part of their Advanced Turboprop Program, established in 1975, to develop efficient, reliable, and acceptable operation of advanced turboprop or prop-fan powered aircraft at cruise speeds up to Mach 0.8 while maintaining noise and vibration levels comparable to typical turbofan aircraft at the time [5]. This set of experiments has provided much of the openly available aerodynamic and aeroacoustic data on turboprop propellers.

### **1.2.2 Development of Computational Noise Models for Propellers**

Propeller noise models have been developed as early as 1919, though, at the time, they were quite limited due to a lack of computational power and experimental equipment [6], [7]. In 1936, Gutin [8] was the first to develop a noise prediction theory, which correctly described the noise generation process in propellers. Significant progress was then made between the 1950s and the 1970s as a result of the advent of computers and the acoustic analogy first proposed by Lighthill [9]. This work lead to the derivation of the Ffowcs Williams and Hawkings (FW-H) Equations in 1969 [10], upon which most of the propeller noise models are currently based [7]. All these models share the concept that blade loads and fluid displacement around the propeller are predicted via some sort of

aerodynamic method in the rotating frame and then converted to an acoustic signal in the non-rotating frame. The blade loads are either represented as a spanwise distribution along the quarter-chord line (Gutin) or surface pressure distribution (FW-H).

### 1.2.3 Propeller Noise Sources

Propeller noise consists of steady noise sources, unsteady noise sources, and random sources [1]. Steady noise sources are divided into three elements: a) thickness noise, which is dependent upon the geometry of the propeller, b) loading noise, which is dependent upon the aerodynamic loading on the propeller, and c) quadrupole noise, which is dependent upon noise sources distributed around the volume of the blades. Thickness noise, as the name implies, is caused by the transverse displacement of air due to the actual shape of the propeller and is proportional to the volume of a propeller. Loading noise is caused by forces exerted upon the air by a propeller blade, such as thrust and torque. For moderate blade speeds, the thickness and loading noise sources dominate, with the quadrupole sources only becoming significant for transonic speeds [1]. Unsteady sources can come from inflow distortion or effects such as the tilt of the propeller shaft during climb, causing a cyclic change in angle of attack. Random sources of noise result in broadband noise, caused by turbulence ingested from the inflow or that generated in the turbulent boundary layer, leading edge, and tip vortex of a propeller [1]. For full scale propellers operating in flight, broadband noise sources are relatively insignificant [11]. Noise data for propellers is typically represented graphically in the frequency domain for a given microphone or pressure transducer, as shown in Fig. 1.3 below.

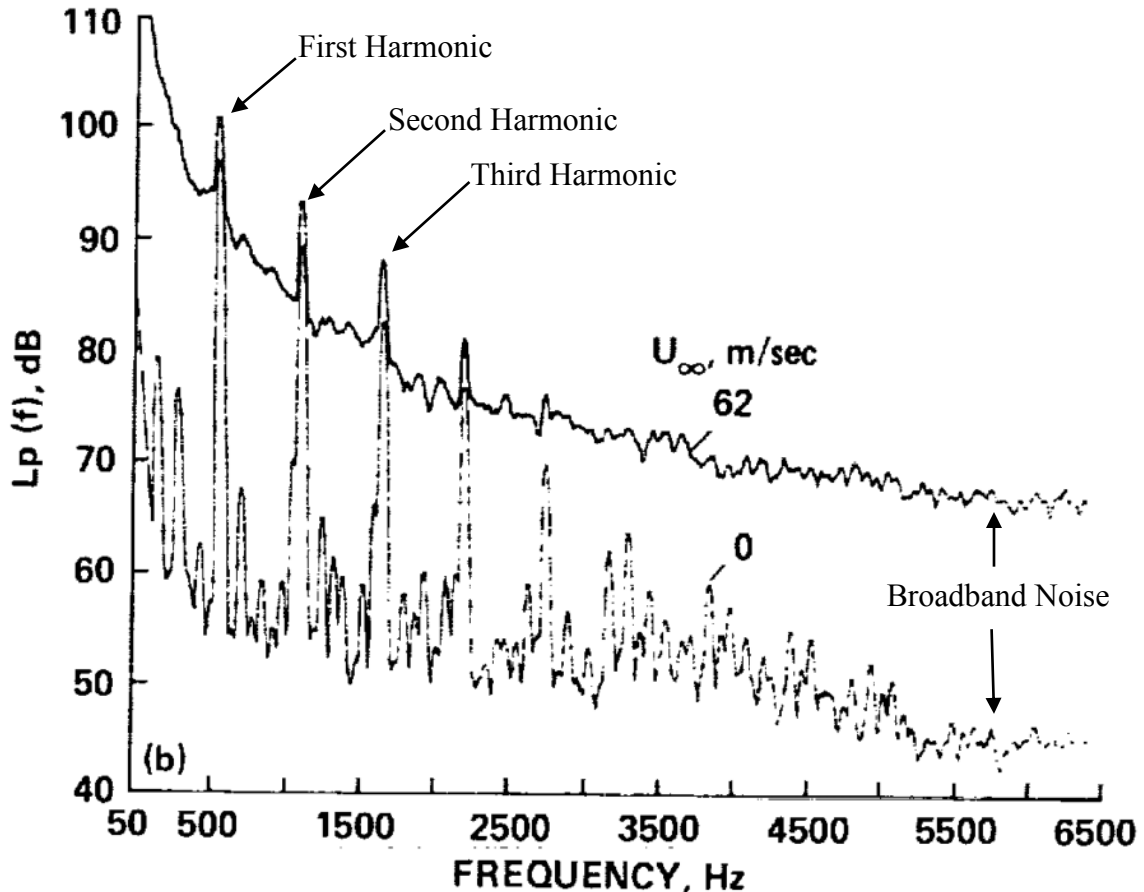


**Fig. 1.3: Example plot from literature showing propeller noise data captured at a pressure transducer for two different free stream speeds [12].**

As can be seen in the above plot, the peak noise is emitted at frequencies which are integer multiples of the blade passage frequency (BPF), referred to as harmonics. Because these harmonics are the loudest element of propeller noise, propeller noise is often described by tabulating the magnitude of these peaks rather than providing plots.

#### 1.2.4 Impact of Design Parameters on Propeller Noise

The influence of design parameters on propeller noise has been studied since the earliest numerical methods for predicting propeller noise emerged, as evidenced by Hubbard's extensive propeller noise charts in 1953 [13]. Since then, many parametric studies have

been performed with the continued evolution and improvement of numerical models, as summarized in this section.

a. RPM and Tip Speed

Because all sources of noise radiation are dependent upon relative velocity, if the RPM, and consequently tip speed, can be decreased, all sources of noise are generally reduced [1]. It has been shown that for conventional propellers operating at low to moderate flight speeds, the overall noise in decibels varies as approximately 40 times the tip Mach number [14].

b. Propeller Diameter

An increase in propeller diameter results in a decrease in blade loading, consequently reducing loading noise for a given thrust. Because loading noise dominates at takeoff, increasing a propeller diameter is most significant during this phase of flight [1]. However, increasing diameter can also increase blade volume or tip speed which can increase noise.

c. Blade Count

For a given thrust, increasing blade count will decrease loading and quadrupole noise, creating significant reductions during flight regimes where loading noise dominates such as during takeoff. This reduction is particularly evident at higher harmonics. However, increasing the blade count increases the frequency of the propeller harmonics which can bring more noise into the range of frequencies which are more sensitive to the human ear, resulting in a higher perceived noise. If blades are simply added to a propeller, overall blade volume increases and thickness noise will increase. Thus, it is best if blades can be added while also reducing the volume by reducing blade thickness or chord [1].

#### d. Blade Thickness

Propeller blade thickness is the width of a blade section perpendicular to its chord, the line connecting the leading and trailing edge. A visualization of blade thickness is shown in Fig. 1.4. Thickness noise can be quite significant at cruise speeds and a simple method to reduce thickness noise is to reduce the blade thickness and chord, with the goal to reduce the overall volume of the blade. This has been shown to provide reduction at each harmonic, while also reducing quadrupole noise [1]. Consequently, propellers are often designed with small thickness to chord ratios, such as the high speed SR-2 and SR-7 propellers which have thickness to chord ratios of 24% and 16% at the root and 1% and 5% near the tip, respectively [5], [15].

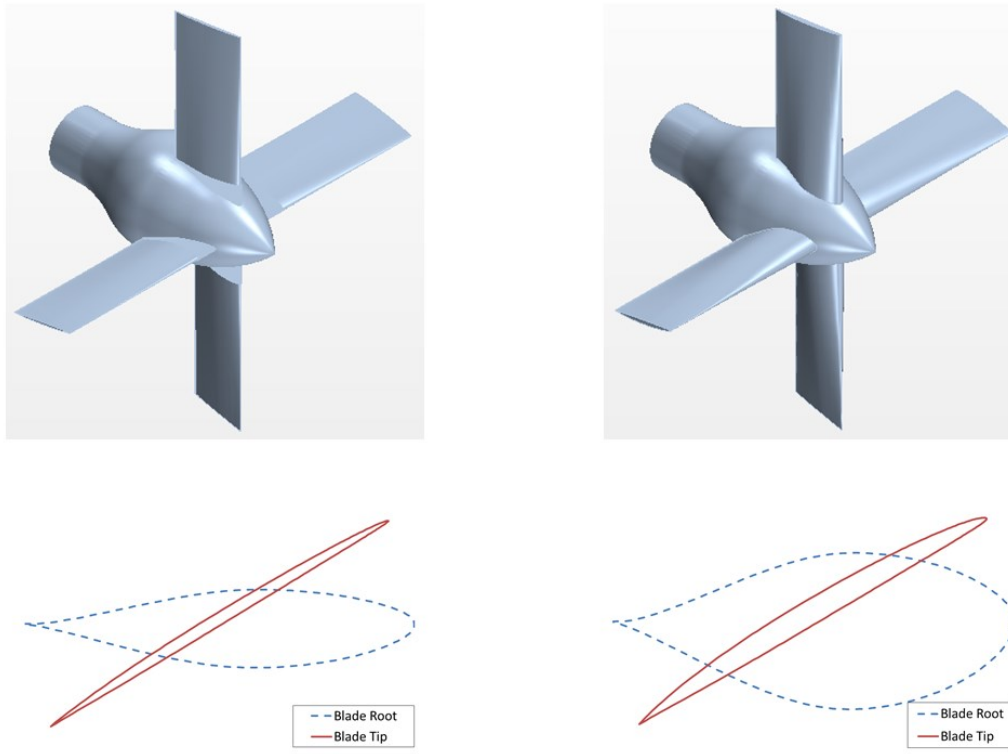


**Fig. 1.4: A visualization of blade thickness, with a relatively thin (left) and thick propeller (right).**

### e. Blade Sweep

Blade sweep is a bending of a propeller blade in a direction parallel to the chord, as portrayed in Fig. 1.5.

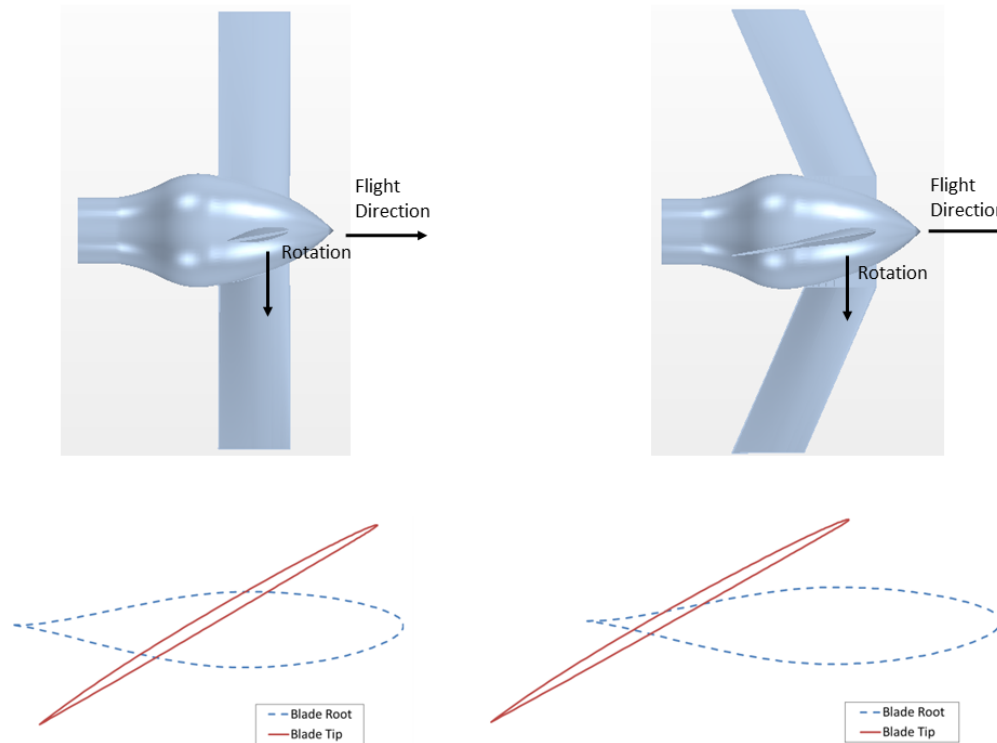


**Fig. 1.5: An unswept (left) and swept (right) propeller.**

During high speed cruise, blade sweep has been shown to be very beneficial for noise reduction. At takeoff, as well as at low speeds, noise reduction due to sweep is less significant [1]. The effect of sweep becomes increasingly more beneficial as the angle of sweep is increased, as shown in Fig. 1.6.

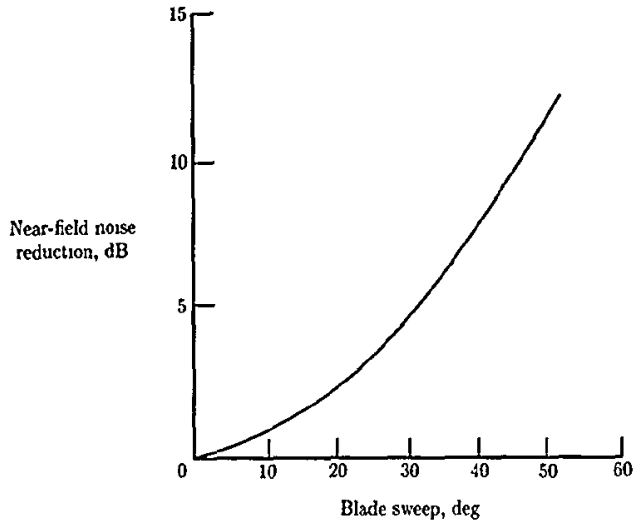


**Fig. 1.6: Noise reduction due to sweep for an 8 bladed propfan at a cruise speed of 0.8 Mach [1].**

This reduction in noise occurs because of two main effects. First, sweep mitigates the effects of transonic compressibility, as with a swept wing design, in turn reducing quadrupole sources. Second, noise is reduced because of phase interference caused by the physical displacement of the noise sources on the blade [16]. In other words, the sweep causes the noise sources along the blade to lag in phase with one another, ultimately causing signal interference and reducing the overall noise signal.

#### f. Offset

Offset, also known as face alignment, is the bending of a blade in a direction perpendicular to the chord as shown in Fig. 1.7. Though offset has the potential for phase cancellation resulting in noise reduction, in practice, only small amounts of offset are feasible [16].

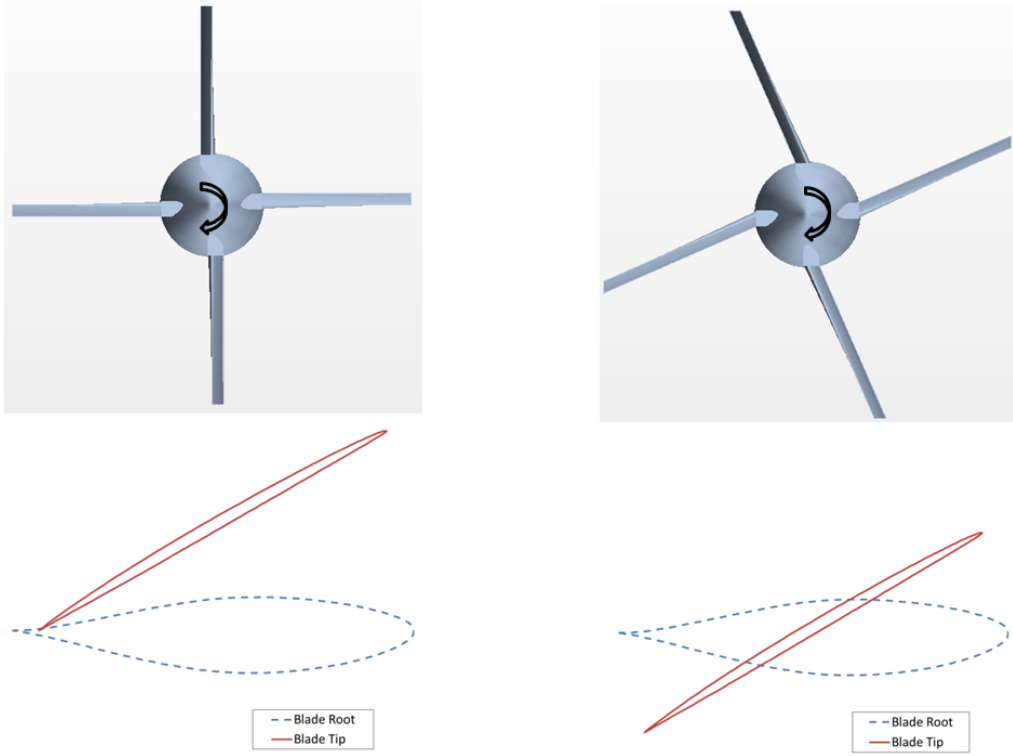


**Fig. 1.7: A standard propeller (left) compared to a propeller with offset (right).**

#### g. Twist and Taper

Twist, an essential aerodynamic characteristic of propellers in order to achieve reasonable relative angle of attack, is the relative rotation of a blade section along the span, as shown in Fig. 1.8. Taper is the relative reduction in chord length from root to tip, as shown in Fig. 1.9. Both twist and taper enable the designer to optimize the loading along a propeller blade. Overall, the noise reduction due to blade twist and taper has a stronger effect on aerodynamic performance than noise, only offering minimal opportunity for noise reduction [1]. Twist can change the spanwise distribution of blade loading, thus enabling the loading to be moved closer to the hub where it radiates less effectively. However, this often results in a high aerodynamic performance penalty [16].

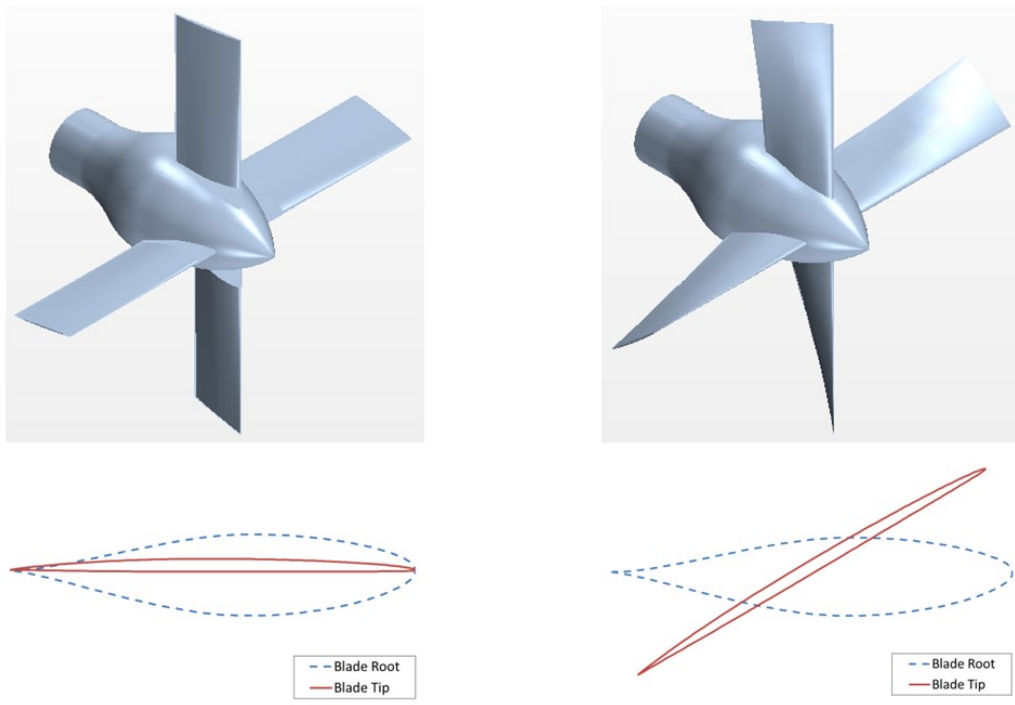


**Fig. 1.8:** A propeller without twist (left) compared to a propeller with twist (right).

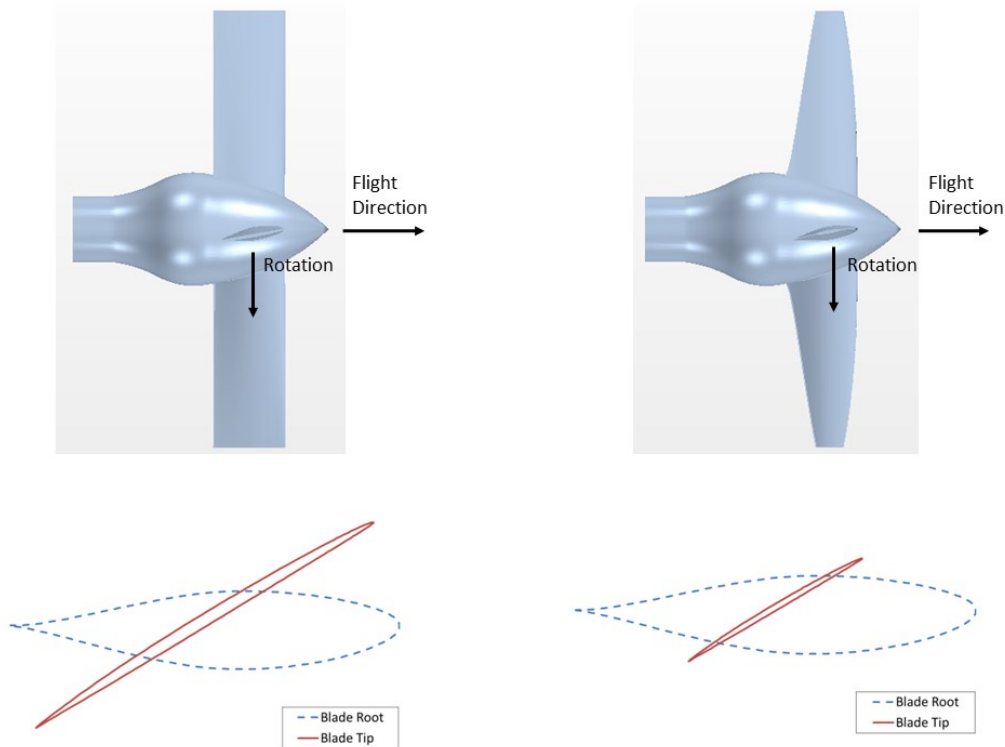


**Fig. 1.9:** A propeller without taper (left) compared to a propeller with taper (right).

#### h. Airfoil Shape

Some airfoil sections have been shown to be more effective for noise reduction, however, this only has only been shown to have a small effect on the lower harmonics emitted from high speed propfans [1].

### **1.3 Experimental and CFD Studies on Propeller Aeroacoustics**

For model validation and propeller design, a number of experiments have been performed and published as presented in Table 1.1 and Table 1.2. This list is not comprehensive, but represents many of the experiments available in the open literature. Most of the experiments were developed either in the process of designing quiet, high speed propellers or to generate data for propeller noise verification. Many computational studies have been performed top validate different noise models on the experiments in Table 1.1 and Table 1.2. However, relatively few couple an aerodynamic and an aeroacoustic prediction. Studies that do so are listed in Table 1.3.

**Table 1.1: Published Experiments on Propeller Aeroacoustics**

Author	Year	RPM	Free Stream Mach Number	Test Type
Paris [17]	1932	800	0.0	Free Field*
Kemp [18]	1933	800	0.0	Free Field*
Hicks and Hubbard [19]	1947	1100-4800	0.0	Free Field*
Hubbard [20]	1950	2300-3800	0.0	Free Field*
Hubbard [21]	1952	3900-6900	0.0	Free Field*
Karbjun [22]	1955	1675	0.0	Free Field*
Karbjun [23]	1957	3500	0.0	Free Field*
Brown and Ollerhead [24]	1973	1000-3150	0-0.13	Wind Tunnel, Free Field*
Dittmar et al. [25]	1978	8500	0.8	Wind Tunnel
Dittmar et al. [26]	1980	4600-9000	0.7-0.85	Wind Tunnel
Dittmar and Jeracki [27]	1981	5400-8900	0.6-0.85	Wind Tunnel
Dittmar and Jeracki [28]	1981	5600-9100	0.6-0.85	Wind Tunnel
Dittmar and Lasagna [29]	1981	5700-7500	0.6-0.8	Flight
Dittmar et al. [30]	1982	4600-7900	0.5-0.85	Wind Tunnel
Succi et al. [31]	1982	7000-10000	0.08	Wind Tunnel
Sulc et al. [32]	1982	1900	0.2-0.3	Flight
Dittmar et al. [33]	1983	5600-7500	0.6-0.8	Wind Tunnel
Dittmar and Lasagna [34]	1983	5000-7100	0.6-0.8	Flight
Treble et al. [35]	1983	1000-1700	0.03-0.15	Wind Tunnel
Block and Gentry [36]	1986	7200-11400	0.1	Wind Tunnel
Dobrzynski et al. [11]	1986	1069-2800	0.1-0.2	Wind Tunnel
Woodward et al. [37]	1987	5600-8800	0.2	Wind Tunnel
Dittmar and Stang [38]	1988	5600-10100	0.6-0.85	Wind Tunnel
Schulten [39]	1988	N/A	N/A	Wind Tunnel
Dittmar [15]	1989	5100-9500	0.6-0.8	Wind Tunnel
Dittmar and Hall [40]	1990	4900-8100	0.6-0.8	Wind Tunnel
Soderman and Horne [12]	1990	6000-8200	0-0.18	Wind Tunnel
Zandbergen et al. [41]	1990	0-7500	0.1-0.2	Wind Tunnel
Dittmar et al. [42]	1991	6000-9300	0.6-0.86	Wind Tunnel
Schulten [43]	1997	5700-8200	0.2-0.78	Wind Tunnel
Sinibaldi and Marino [44]	2013	N/A	N/A	Wind Tunnel

\*Free field signifies an outdoor test in an open area.

**Table 1.2: Propeller Information for Available Experiments on Propeller Aeroacoustics**

Author	Year	Propeller	Blade Number	Diameter [m]
Paris [17]	1932	N/A	2	4.5
Kemp [18]	1933	N/A	2	4.5
Hicks and Hubbard [19]	1947	Sensenich No. 70145	2	1.77
		NACA 4-(3)(06.3)-06	4	1.22
		NACA 4-(3)(08)-03	7	1.22
Hubbard [20]	1950	Clark Y	2,5	1.25
Hubbard [21]	1952	NACA (5)(08)-03	2	1.22
Karbjun [22]		N/A	4	3.0
Karbjun [23]	1957	N/A	3	2.2
Brown and Ollerhead [24]	1973	NACA 0012	2	1.25
		Sensenich W 60LK 18	2,3,4,6	1.25
Dittmar et al. [25]	1978	SR-2, SR-1M*, SR-3*	8	0.622
Dittmar et al. [26]	1980	SR-2, SR-1M*, SR-3*	8	0.622
Dittmar and Jeracki [27]	1981	SR-3*	8	0.622
Dittmar and Jeracki [28]	1981	SR-3*	8	0.622
Dittmar and Lasagna [29]	1981	SR-3*	8	0.622
Dittmar et al. [30]	1982	SR-6*	10	0.696
Succi et al. [31]	1982	1C160	2	0.473
Sulc et al. [32]	1982	NACA 0016	3	2.5
Dittmar et al. [33]	1983	SR-6*	10	0.696
Dittmar and Lasagna [34]	1983	SR-6*	10	0.696
Treble et al. [35]	1983	R292	4	2.82, 0.705
Block and Gentry [36]	1986	SR-2	4 8	0.409
Dobrzynski et al. [11]	1986	F 8475 D-4 F 9684 – 14	2 2	2.03
Woodward et al. [37]	1987	SR-7A*	8	0.622
Dittmar and Stang [38]	1988	SR-7A*	8	0.622
Schulten [39]	1988	N/A	6	0.732
Dittmar [15]	1989	SR-2	8	0.622
Dittmar and Hall [40]	1990	SR-7A*	8	0.622
Soderman and Horne [12]	1990	SR-2	4	0.591
Zandbergen et al. [41]	1990	Fokker 50 (ARA-D)	6	0.732
Dittmar et al. [42]	1991	SR-7A*	8	0.622
Schulten [43]	1997	LSP, HSP*	6	0.9
Sinibaldi and Marino [44]	2013	Clark Y	2	0.6
		NACA 16		

\*These are swept propellers.

**Table 1.3: Aerodynamic and Aeroacoustic Simulations of Propeller Noise Validated by Experiment**

Author	Year	Aerodynamic Calculation	Acoustic Calculation	Validation Case
Gutin [8]	1936	Blade Element Theory	Gutin	Paris [17] and Kemp [18]
Succi et al. [31]	1982	Lifting Line	FW-H	Succi et al. [31]
Schulten [39]	1988	Blade Element Theory	Kirchoff-Helmholtz	Schulten [39]
Nallasamy et al. [45]	1989	Euler Equation	FW-H	Woodward [46]
Whitefield et al. [47]	1989	Euler Equation	FW-H	[21], [23], [26], [27], [32], [33], [48]–[50]
Schulten [51]	1996	Lifting Line	Kirchoff-Helmholtz	Schulten [51]
Schulten [52]	1997	Lifting Line	Kirchoff-Helmholtz	Zandbergen et al. [41]
De Gennaro et al. [53]	2010	RANS	FW-H	Dittmar [15]
Pagano [54]	2010	Potential Flow	FW-H	Schulten [52]
Boots and Feszty [55]	2016	Discrete Vortex	FW-H	Soderman and Horne [12]

It is noted that a number of university theses at the Masters and Doctoral level also perform computational validation studies on propeller aerodynamic and aeroacoustic data [56]–[60]. In addition a number of models are validated to other numerical data, but, because of a lack of comparison to experimental data, are omitted from Table 1.3.

## 1.4 Research Objectives

It can be seen in Table 1.3 that there is only one published CAA study using a Reynolds Averaged Navier-Stokes (RANS) simulation (defined in Section 3.1.1.2.1) which can enable much more accurate and robust calculation of aerodynamic forces and the flow field than the other methods listed at higher computational cost. The study utilizing RANS [53] is fairly narrow in scope as it is based on the steady state simulation of a slice of the domain with periodic boundary conditions. Though the comparison to

experiment is good, six separate acoustic adjustments are added to the CAA noise predictions before comparison with experiment. A number of those adjustments are based on loose justification from literature and are not found in other studies of the same validation case. Consequently:

- There is a need to assess how accurately and feasibly RANS methods coupled with an acoustic solver can calculate of propeller noise.
- There is a need to establish a methodology to set up propeller aeroacoustic simulations due to the limited availability of reference studies.
- There is a need to evaluate whether a higher fidelity method like RANS is more advantageous than a simpler and less expensive method for the simulation of propeller noise.

Based on the above needs, this thesis has the following goals and approach:

1. To investigate the effectiveness and feasibility of a RANS solver for the prediction of flow as part of a CAA method to predict propeller noise.
2. To compare the effectiveness of a RANS method to a simpler CFD method as part of a propeller noise calculation.
3. To establish methodology for the prediction of propeller noise using both CFD methods for a propeller comparable to one used in a turboprop application.
4. To utilize the established methodology for both CFD methods to perform a parametric study varying one of the design parameters described in Section 1.2.4.

## 1.5 Approach

In order to accomplish the research goals, two codes were selected for use: a) STAR CCM+, a well-established industrial code capable of a broad variety of CFD simulations and b) SmartRotor, an in-house discrete vortex method with an aeroacoustic solver. The following approach was employed:

1. A simple and well-documented computational aeroacoustic case was studied in order to validate the STAR CCM+ simulation software. This was done through simulating the interference between two cylinders, one of the most studied problems in Computational Aeroacoustics. The results were then compared to the experimental results of pressure and noise in literature [61]–[65]. The experiment and results are described in detail in Chapter 4.
2. Two separate aeroacoustic validation simulations were performed to establish a strong methodology and compare the capabilities of STAR CCM+ utilizing a RANS aerodynamic solver and SmartRotor utilizing a discrete vortex aerodynamic solver. The background to these experiments is provided in Chapter 2, while the validation results are described in detail in Chapter 5 and Chapter 6.
3. A parametric study on the impact of blade count on propeller noise was performed using propellers having 7, 8, and 10 blades. The results of this study are detailed in Chapter 7.

## **Chapter 2: Test Cases Selected for Validation**

In order to develop confidence in the numerical prediction of aeroacoustics of a propeller, a building-block approach was applied. First, a relatively simple, but experimentally well documented test case was considered: the noise generated by the unsteady force on a tandem cylinder configuration with vortex shedding. This test case served to build confidence in capturing the relevant surface pressure loads as well as in converting them to noise data at specific locations. Following this, two test cases involving a scaled experimental propeller, tested in a wind tunnel, were considered in increasing level of complexity. Detailed descriptions of these test cases are provided in this chapter.

In selecting propeller validation cases, the focus was on the prediction of noise for propellers representative of those currently in production for turboprop aircraft, namely, straight-bladed propellers with subsonic tip speeds. The selection of a straight blade, i.e., one without sweep, also enables the validation cases to serve as a good base case for future parametric studies. In selecting only straight-bladed experiments with subsonic tip speeds and available geometrical data from Table 1.1 and Table 1.2, the following list of potential test cases result.

**Table 2.1: List of Potential Experiments for Validation Cases**

<b>Author</b>	<b>Year</b>	<b>Propeller</b>	<b>Blade Number</b>	<b>Free Stream Mach Number</b>
Hicks et al. [19]	1947	Sensenich No. 70145	2	0.0
		NACA 4-(3)(06.3)-06	4	
		NACA 4-(3)(08)-03	7	
Hubbard [20]	1950	Clark Y	2,5	0.0
Brown et al. [24]	1973	NACA 0012 Sensenich W 60LK 18	2 2,3,4,6	0-0.1
Block et al. [36]	1986	SR-2	4 8	0.1
Dobrzynski et al. [11]	1986	F 8475 D-4 F 9684 – 14	2 2	0.1-0.2
Dittmar [15]	1989	SR-2	8	0.6-0.8
Soderman et al. [12]	1990	SR-2	4	0-0.2

From the above test cases, the 1990 test from Soderman and Horne [12] and the 1989 test from Dittmar [15] were selected. The combination of the two test cases enables the aeroacoustic validation of a 4-bladed and 8-bladed SR-2 propeller at a flight speed of both 0.2 and 0.6 Mach, respectively. Moreover, the SR-2 propeller has been designed for high speed turboprop flight [26], the flight regime of interest. The 1989 case from Dittmar [15] also enables comparison to the validation case from De Gennaro [53] which is the only published propeller aeroacoustic validation study that uses RANS for aerodynamic prediction as discussed in Section 1.3.

## 2.1 Tandem Cylinder Test Case

One of the most studied benchmark cases for CAA is the tandem cylinder benchmark case, where an upstream cylinder sheds vortices upon a downstream cylinder, as can be seen in Fig. 2.1. This case was studied first to investigate the capability of a STAR CCM+ to simulate noise. Efforts were made to keep the computational costs low.

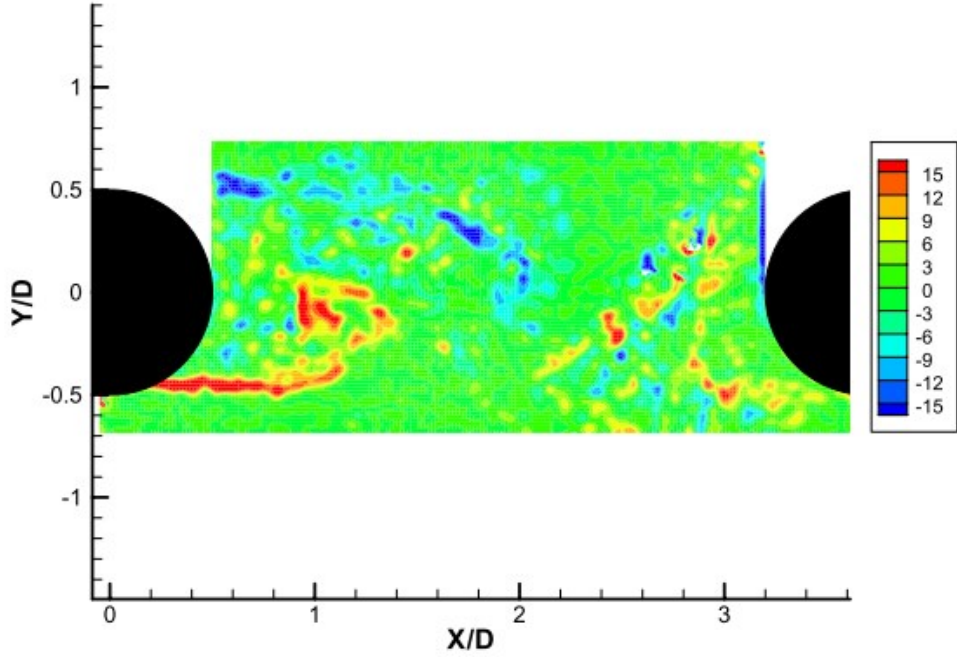


**Fig. 2.1: Instantaneous spanwise vorticity of tandem cylinder experiment [61],  $Re = 166,000$ .**

This test case was initially set up by NASA to provide extensive aerodynamic and aeroacoustic data to study the unsteady flow across two cylinders arranged in tandem at a critical Mach number, resulting in the upstream cylinder shedding vortices upon the downstream cylinder. The study was initially performed in 2005 at the Basic Aerodynamic Research Tunnel (BART) at the NASA Langley Research Center to investigate the noise produced by components of landing gear [62], and repeated in 2006 [61] and 2009 [63] to augment the dataset of aerodynamic and aeroacoustic measurements for the purpose of developing and validating computational techniques for predicting such unsteady flow. Additionally, similar measurements were made in NASA's Quiet Flow Facility (QFF) in 2006 [64] and 2014 [65] to further expand this dataset, resulting in one of the most comprehensive aerodynamic and aeroacoustic datasets for computational aeroacoustics. Due to the detail of the unsteady pressure data, numerous numerical studies have been published comparing simulated results to that of

the experiment [57], [66]–[93], including summary papers describing various solutions [94], [95].

In the experiments performed at the NASA BART [61]–[63] and QFF [64], [65] facilities, numerous measurements were taken of the unsteady and mean flow field along with noise measurements at a number of flow conditions and configurations. This study focuses on the case when the cylinders are spaced 3.7 diameters ( $D$ ) apart with a freestream velocity of 44 m/s resulting in a Reynolds number of  $1.66 \times 10^5$ . The span of the cylinders was  $12.4D$  in the BART experiment and  $16D$  in the QFF experiment. The experimental setup analyzed in this chapter can be seen in Fig. 2.2 with  $L = 3.7D$  and  $D = 0.05715$  m, and the experimental apparatus is shown in Fig. 2.3.

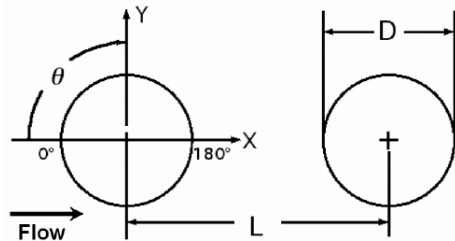


**Fig. 2.2: Experiment setup of tandem cylinder test case [74]**

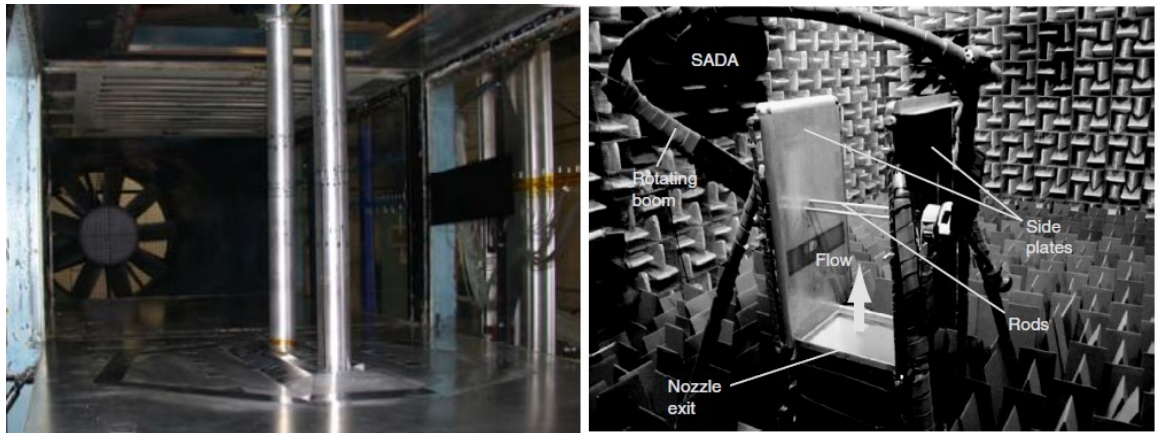


**Fig. 2.3: Experimental apparatus at BART (left) [62] and QFF (right) [64]**

## 2.2 Propeller Test Case 1: SR-2 Propeller in Low Speed Condition

This experiment was performed by Paul Soderman and W. Clifton Horne in the NASA Ames Research Center 7-by-10 foot wind tunnel in 1990, in a study of aerodynamic and aeroacoustic results of a pusher propeller [12]. The purpose of the experiment was to measure detailed wake and noise properties from a 591 mm SR-2 propeller, particularly when the pusher propeller is operating in the wake of an I-tail, Y-tail, and V-tail empennage. This provides an excellent validation case as acoustic measurements were performed with the propeller operating alone in the wind tunnel, as well as empty wind tunnel noise measurements at the operating conditions. The experimental conditions selected for validation in this thesis are summarized in Table 2.2:

**Table 2.2: Experiment Conditions for SR-2 Test Case 1**

Property	Value
<b>Propeller</b>	SR-2
<b>Propeller diameter</b>	0.591 m
<b>Number of Blades</b>	4
<b>Blade Pitch Angle</b>	21
<b>Mach Number</b>	0.18
<b>RPM</b>	8200

The propeller utilized, the NASA SR-2 scaled propeller, is an unswept propeller consisting of NACA 65 series airfoils from the propeller root through to 37% percent of the blade radius, followed by a transition region to NACA 16 series airfoils, which define the propeller section from 44% of the radius to the propeller tip. This geometry is described in Fig. 2.4. Acoustic measurements were made via 13 transducers, Fig. 2.6.

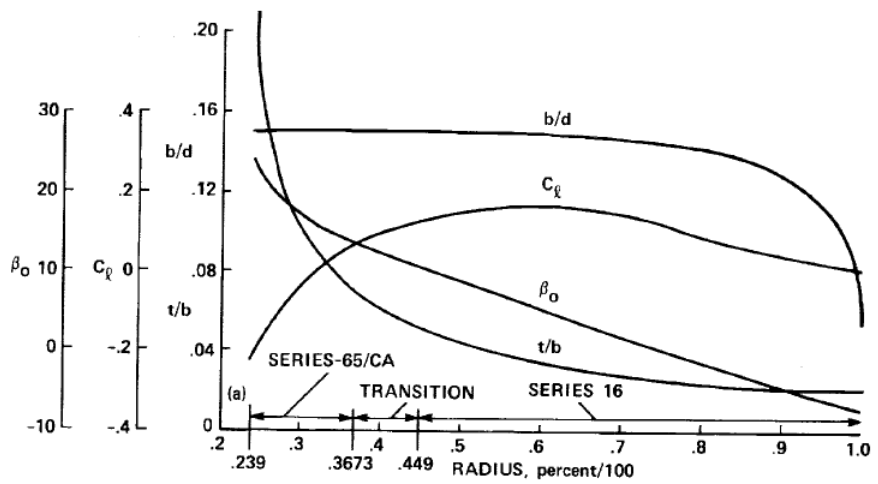


Fig. 2.4: SR-2 Propeller Geometry, describing (a) spanwise distribution of chord ( $b$ ), twist ( $\beta_0$ ), thickness ( $t$ ), diameter ( $d$ ), and design lift coefficient ( $C_L$ ) [12].

#### Planform View

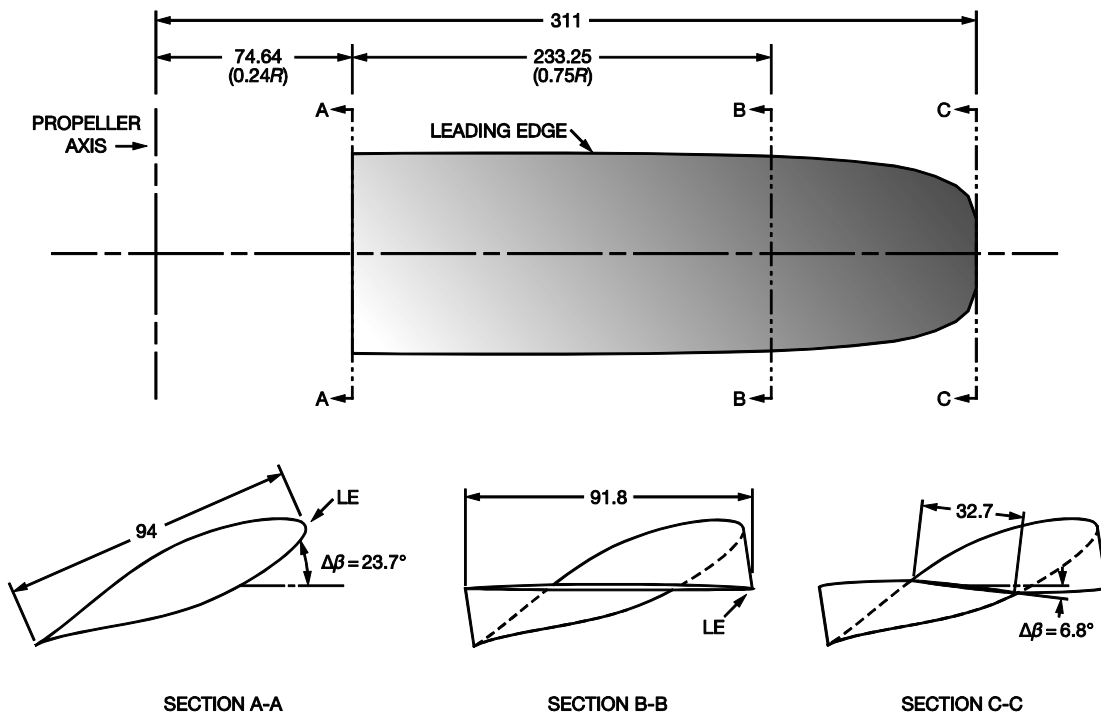
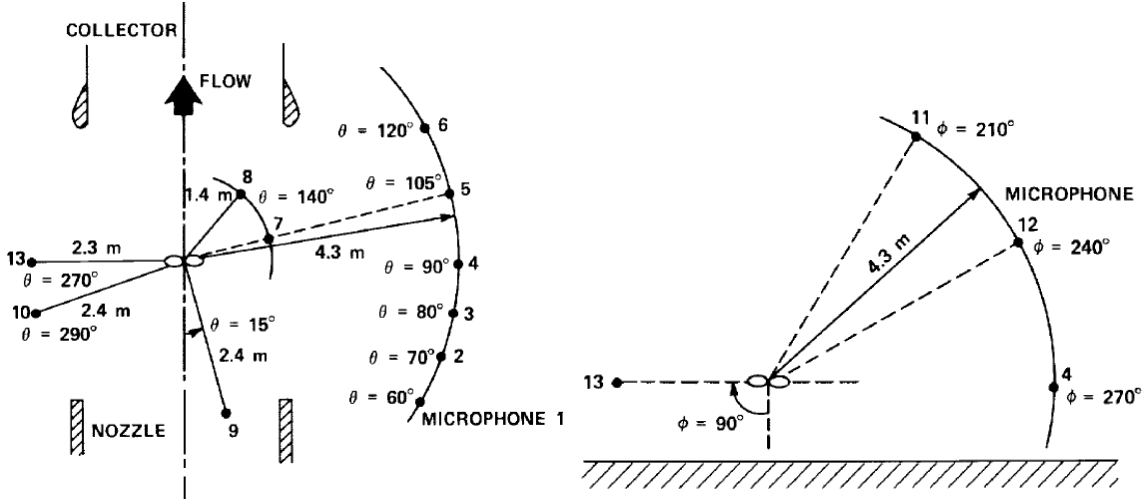


Fig. 2.5: Planform view of 622 mm diameter SR-2 Propeller Blade [58], with dimensions in mm.



**Fig. 2.6: Transducer locations relative to the propeller hub, with a description of the plan view (left) and the plane containing the propeller looking downstream (right) [12].**

Boots performed the only available validation case of this experiment using the SmartRotor discrete vortex method coupled with a Ffowcs Williams-Hawking acoustic solver [55]. Nonetheless, a similar validation using SmartRotor is performed in this work to obtain data at an additional microphone for additional comparison to the STAR CCM+ predictions.

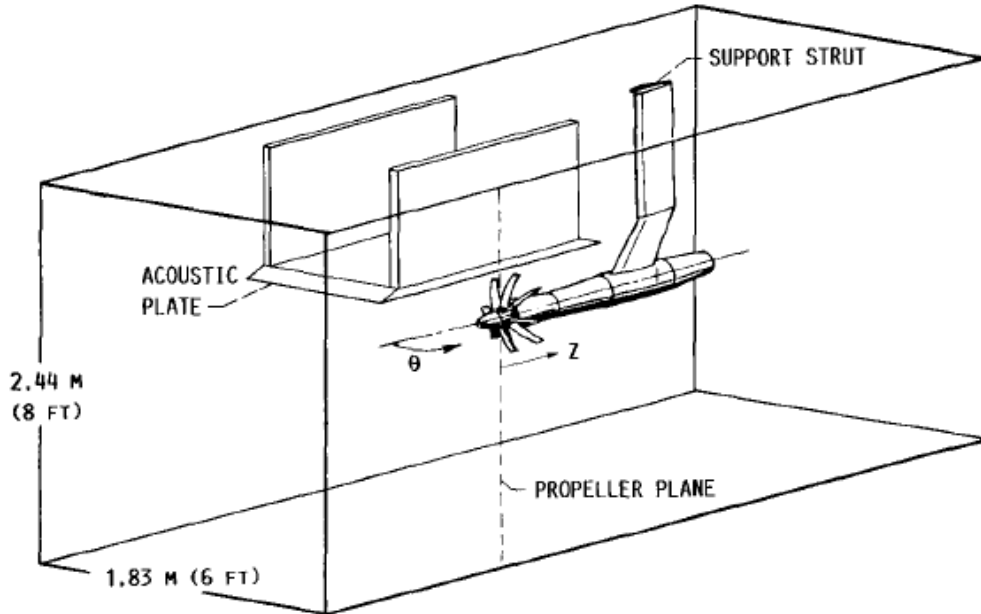
### 2.3 Propeller Test Case 2: SR-2 Propeller in Cruise Condition

This experiment was performed by James Dittmar in the NASA Lewis Research Center 8-by-6 foot wind tunnel in 1989, in a study of aerodynamic and aeroacoustic results of an SR-2 propeller [15]. The experimental conditions which were simulated are summarized in Table 2.3. The propeller geometry for each blade is depicted in Fig. 2.4, differing from the propeller tested by Soderman and Horne only in diameter and blade count.

Table 2.3: Experiment Conditions for SR-2 Test Case 2

Property	Value
<b>Propeller</b>	SR-2
<b>Propeller diameter</b>	0.622 m
<b>Number of Blades</b>	8
<b>Blade Pitch Angle</b>	59
<b>Mach Number</b>	0.6
<b>RPM</b>	6487

Acoustic measurements were made at 12 transducers, shown, along with the experiment apparatus in Fig. 2.7.



TRANSDUCER (PLATE 0.3 DIAMETER FROM TIP)											
1	2	3	4	5	6	7	8	9	10	11	12
TRANSDUCER DISTANCE FROM PROPELLER PLANE, Z, CM (IN.)											
-46.7 (-18.4)	-41.7 (-16.4)	-30.5 (-12.0)	-16.0 (-6.3)	-8.9 (-3.5)	0.8 (0.3)	8.9 (3.5)	12.4 (4.9)	18.0 (7.1)	25.0 (9.9)	28.7 (11.3)	42.4 (16.7)
ANGLE FROM UPSTREAM, θ, DEG											
46.8	50.0	58.5	72.2	80	90.9	100	104	110	116.8	120	130.4

Fig. 2.7: Experimental apparatus and transducer locations for SR-2 Test Case 2 [15].

De Gennaro et al. [53] performed the only available numerical study on this test case in 2010, using ANSYS FLUENT to utilize a RANS coupled solver using a  $k-\omega$  SST turbulence model on a periodic sliced domain of 10.5 million cells containing only 1 blade. Acoustic performance was simulated through a Ffowcs Williams-Hawkins Solver. Two simulations were performed: one at 0.6 Mach and one at 0.8 Mach, both corresponding to experimental measurements performed by Dittmar [15]. In order to match the experimental power coefficient, De Gennaro et al. increased the blade pitch angle was increased to 60 degrees (compared to the experimental value of 59 degrees). This lead to a power coefficient of 1.32 compared to the experimental value of 1.34. For both simulated cases, the SPL of the first harmonic was calculated to be within 2 dB of the experimental values after corrections of 40.5 dB and 38.5 dB were added to the computational results of the 0.6 Mach and 0.8 Mach simulations, respectively. Details about each type of correction added are discussed in Section 2.4.

## 2.4 Using Wind Tunnel Data to Validate Propeller Aeroacoustic Simulations

The conditions of a wind tunnel experiment, governed by an interior flow, are different than typical simulations of a propeller in free space or in flight. Consequently, adjustments can be made to wind tunnel data to better represent acoustic conditions of flight or a numerical simulation. Dittmar and Lasagna compared flight tests to wind tunnel tests in [29] using an 8-bladed, 0.622 m diameter SR-3 propeller across flight speeds of 0.6 to 0.8 Mach. Excellent comparison of results was found after adjustments made for differences in atmospheric conditions such as pressure and for differences in the distance of noise measurement locations in the same direction. These two adjustments are

also seen in the numerical simulations of Whitefield [47] alongside other studies [57], [60] which make similar adjustments.

De Gennaro et al. [53] uses additional adjustments to the numerical predictions according to the adjustments as listed in Table 2.4.

**Table 2.4: Unique Acoustic Adjustments Performed by De Gennaro et al. [53]**

Adjustment	M = 0.6 Adjustment Value	M = 0.8 Adjustment Value
1. Acoustic Plate Interference	8 dB	8 dB
2. Pseudo-Noise	1 dB	1 dB
3. Wind Tunnel Effects	5.5 dB	2.5 dB
4. Non-linear Effects	1 dB	3 dB

These adjustments are not seen in other numerical simulations of propeller aeroacoustics and are justified as follows by De Gennaro et al. [53]:

1. The acoustic plate interference adjustment value of 8 dB is based on the original experiment report by Dittmar [15]. Though the plate will have interference effects and boundary layer refraction of noise [96], an adjustment value of 8dB is not justified by De Genarro et al. or described as an adjustment in the original report from Dittmar [15] as implied.
2. The pseudo-noise adjustment value is used to incorporate the effect of near field noise on far field noise based on a near field model described in Sulc et al. [32]. Though this is a valid source of error to compare the experient to a numerical simulation, the value of 1 dB is based on an estimate which is not applied directly to the experimental case.
3. The adjustments for wind tunnel effects is based on Dittmar and Lasagna [29], but it is unclear what specifically is being referred to as “wind tunnel effect” and the

adjustment value is not directly present in Dittmar and Lasagna [29] or justified in De Gennaro et al. [53]. The wind tunnel does indeed contribute noise, which will be discussed at the end of this section.

4. The adjustment for non-linear effects is based on a calculation of non-linear effects in [1], originally based on the method and results of Hanson [97] who calculated non-linear effects for a propeller similar to the simulated SR-2 propeller.

Though the above adjustments are sources of error, the first three adjustments will not be included because of poor justification of the quantity of adjustment. The fourth adjustment will not be included as the effect is relatively small for the magnitude of frequencies which are being predicted, which have a peak range of 100-140 dB [12], [15]. Moreover, this adjustment is neglected for the sake of clarity as it is based on the calculation of quadrupole noise (described in Section 3.1.4.2) which, throughout the discussion of methodology and results, is described as neglected.

As the microphones will not be displaced from their experimental locations, there is no need to consider adjustments because of differences in distance. However, adjustments will be considered for the pressure difference in the simulations and in the wind tunnel according to the following formula as described in [47]:

$$SPL = SPL_{raw} - 20 \log_{10}(P_{simulation}/P_{wind\ tunnel}) \quad (2.1)$$

where SPL represents the adjusted sound pressure level,  $SPL_{raw}$  represents the SPL value outputted by the simulation before adjustment for pressure difference. No adjustments

will be added to the propeller validation cases presented in Chapters 5 and 6, but the impact of adding the adjustment in Equation 2.1 will be discussed in Chapter 8.

The other effect which can be accounted for is the actual noise from the wind tunnel, which impacts the measured propeller noise (though mainly on a broadband level). Wind tunnel data is often not supplied, however, for the case of Soderman and Horne, it was for microphone 7 as seen in Fig. 5.7. If one were to add this data to the peak harmonic, the addition of the wind tunnel pressure to the pressure produced by the propeller, an increase of 0-5 dB could be added to the first three harmonics. Again, this will be discussed in Chapter 8. As Dittmar [15] does not provide wind tunnel data, such an adjustment cannot be made for the wind tunnel he used.

## Chapter 3: Numerical Methods

This chapter provides a brief description of the two numerical methods employed, the grid-based STAR CCM+ code as well as the grid-free, in-house SmartRotor code. The choice of these two codes was driven by the desire to identify a numerical method which has the potential to be used in industrial applications. This means that alongside evaluating the accuracy of a method, its computational costs also had to be considered.

STAR CCM+ is a “classical” grid based CFD method widely utilized in the industry. It is viewed as one of the most advanced codes for predicting aeroacoustics, as seen in validation papers such as [67]. The question to be answered via this research was whether it is suitable for simulating propeller aeroacoustics in an efficient manner.

SmartRotor is an in-house code developed specifically for rotary wing applications. It has been extensively validated for the fully aeroelastic-aeroacoustic simulation of rotorcraft flow. It employs a panel method to assess the surface loads and a grid-free discrete vortex method to represent the wake. In contrast to a grid-based solver, it is much more accurate and cost effective in capturing the helical tip vortices in the wake, including the vortex aging. Experience shows that it runs at least an order of magnitude faster than a classical grid-based method. However, the code uses an inherently incompressible Discrete Vortex Method alongside an inviscid panel method. In contrast, STAR CCM+ is viscous and fully compressible everywhere in the computational domain. However, it is expected to dissipate the helical tip vortices in the wake faster than in real life.

In summary, two different codes were chosen to be evaluated in this thesis. Their descriptions are provided in the sections below.

### 3.1 The STAR CCM+ Code

STAR CCM+ is a commercially available CFD software from the CD-adapco company. It consists of numerous modules, enabling the user to conduct fully aerodynamic and aeroacoustic simulations among many others. For this reason, STAR CCM+ has become a popular choice for several key players in the aerospace or automotive sector. In the following sections, an overview of the aerodynamic and acoustic modules will be overviewed since these were utilized for the simulations in this thesis. The code is very extensive, and only the utilized features of the code are described here. In the following chapters, which describe the simulation results, details of the specific choices made for each simulation will be provided.

#### 3.1.1 Numerical Modeling of Aerodynamics in STAR CCM+

##### 3.1.1.1 Governing Equations of Motion

Fluid flow is governed by the Navier-Stokes Equations, a coupled set of partial differential equations based on the conservation of mass, momentum, and energy. The Navier-Stokes equations in Cartesian integral form for a finite control volume  $\tilde{V}$  with differential surface area  $d\tilde{\alpha}$  may be written in vector form:

$$\frac{\partial}{\partial t} \int_{\tilde{V}} \mathbf{W} d\tilde{V} + \oint [\mathbf{F} - \mathbf{G}] \cdot d\tilde{\mathbf{a}} = \int_{\tilde{V}} \mathbf{H}_b d\tilde{V} \quad (3.1)$$

where:

$$\begin{aligned} \mathbf{W} &= \begin{bmatrix} \rho \\ \rho \mathbf{u} \\ \rho E \end{bmatrix}, \quad \mathbf{F} = \begin{bmatrix} \rho(\mathbf{u} - \mathbf{u}_g) \\ \rho(\mathbf{u} - \mathbf{u}_g) \otimes \mathbf{u} + p \mathbf{I} \\ \rho(\mathbf{u} - \mathbf{u}_g) H + p \mathbf{u}_g \end{bmatrix}, \quad \mathbf{G} = \begin{bmatrix} 0 \\ \mathbf{T}_v \\ \mathbf{T}_v \cdot \mathbf{u} + \dot{q}'' \end{bmatrix}, \\ \mathbf{H}_b &= \begin{bmatrix} S_u \\ \mathbf{f}_r + \mathbf{f}_g + \mathbf{f}_p + \mathbf{f}_u + \mathbf{f}_\omega + \mathbf{f}_L \\ S_u \end{bmatrix} \end{aligned}$$

and

- $\rho$  is the density of the fluid
- $\mathbf{u}$  is the velocity vector of the fluid
- $\mathbf{u}_g$  is the grid velocity vector
- $E$  is the total energy per unit mass
- $p$  is pressure
- $\mathbf{I}$  is the identity matrix
- $H$  is the total enthalpy
- $\mathbf{T}_v$  is the viscous stress tensor
- $\dot{q}''$  is the heat flux vector
- $\mathbf{H}_b$  is the vector of body forces, with  $S_u$  representing a source term, and  $\mathbf{f}_r + \mathbf{f}_g + \mathbf{f}_p + \mathbf{f}_u + \mathbf{f}_\omega + \mathbf{f}_L$  representing the sum of the forces due to rotation, gravity, a porous media body force, a user defined body force, a vorticity confinement specific force, and a Lorentz or Laplace force, respectively

When expanding the vector form to a system of equations, the first row of Eq. 3.1 corresponds to the continuity equation, the second corresponds to the momentum equation, and the third corresponds to the energy equation. The momentum equation can be further decomposed to x, y, and z components by considering the components of the velocity vector  $\mathbf{u}$  and  $\mathbf{u}_g$ . These equations are solved in two different ways in this thesis, through coupled or segregated flow models. It should be noted that some terms in the

above equation are set to zero for the flow models in this thesis, including all of the terms in the body force vector,  $\mathbf{H}_b$ , except  $\mathbf{f}_r$ .

Coupled flow models solve the Navier-Stokes equations simultaneously, while segregated flow models solve the momentum equations independently and a predictor-corrector approach is used to link the solution variables together to satisfy the governing equations. Segregated flow is much faster and requires less memory than coupled flow but is less robust and does not resolve compressible, rotating, or convective flows effectively. In addition, the number of iterations to solve a given flow is dependent upon grid size for the segregated model, where it is not for a coupled flow solver. The algorithm used to control the segregated flow in this thesis is the SIMPLE algorithm pioneered by Patankar and Spalding [98].

The flow can be modeled in two ways: steady flow and unsteady flow. In steady flow modeling, time derivatives are made equal to zero, which simplifies the solution of the set of equations. Unsteady flows advance in time according to a defined time step. For unsteady methods in this thesis, solutions utilize an implicit dual time-stepping method first introduced by Jameson [99]. In this method, a number of iterations between advancements in time, called inner iterations, are used to ensure sufficient convergence within each time step.

### 3.1.1.2 Turbulence Modeling

When a flow is turbulent, more variables arise in the description of the flow than can be solved simply through the Eq. 3.1, requiring additional equations to solve the flow.

Though a number of turbulence models are available in STAR CCM+, in this thesis the Shear Stress Transport (SST) model was selected for the simulations and is thus described below. This model was selected because it works well both around and far away from solid surfaces. This is important for propellers, where turbulence in the wake might be important to capture. The overview below is quite brief; a more extensive description can be found in [100].

### 3.1.1.2.1 Reynolds Averaged Navier-Stokes Equations

Due to the fact that turbulence has defined mean properties, one of the simplest ways to define the fluctuating velocities caused by turbulence is through the Reynolds Averaged Navier-Stokes Equations (RANS), which utilize mean properties of turbulence to define the flow. Essentially, velocity is defined as having a mean ( $\tilde{\mathbf{u}}$ ) and a fluctuating component ( $\mathbf{u}''$ ), as shown in Eq. 3.2.

$$\mathbf{u} = \tilde{\mathbf{u}} + \mathbf{u}'' \quad (3.2)$$

Thus, through appropriately describing mean and fluctuating velocity components, turbulence is statistically described. Upon substituting Eq. 3.2 into Eq. 3.1 with appropriate averaging processes, the RANS equations are obtained. These are similar to the original equations except for additional terms that emerge in the momentum and energy equations, as a product of the steady and unsteady terms, including the Reynolds stress tensor,  $T_t$ , which represents the stress impressed upon the mean flow component by the fluctuating flow component:

$$T_{tij} = -\overline{\rho u''_j u''_i} \quad (3.3)$$

where  $i = 1,2,3$  and  $j = 1,2,3$  correspond to the three spatial dimensions. This Reynolds stress is not straightforward to define, and Boussinesq [101] postulated that it could be described in terms of eddy viscosity ( $\mu_t$ ) and turbulent kinetic energy ( $k$ ) as follows:

$$\mathbf{T}_{tij} = 2\mu_t \mathbf{S}_{ij} - \frac{2}{3}\rho k \delta_{ij} \quad (3.4)$$

where  $\mathbf{S}_{ij}$  is the mean strain rate tensor. Despite its simplicity, this approximation was found to work reasonably well for flows where the velocity gradients and turbulence develop slowly. Popular turbulence methods for RANS, namely the  $k-\varepsilon$  and  $k-\omega$  models, have developed two extra transport equations to define the eddy viscosity and turbulent kinetic energy in the Reynolds stresses. Menter [102] developed a modification to this theory, known as the Shear Stress Transport (SST)  $k-\omega$  model, which uses a  $k-\omega$  turbulence formulation in the inner parts of the boundary layer and a  $k-\varepsilon$  formulation in the free stream, improving the effectiveness of the  $k-\omega$  method over a larger variety of flows. Note that in turbulence modeling, the unsteady fluctuations can be resolved only statistically, i.e., one can capture the effect of turbulence, an unsteady phenomenon, by modeling its time-averaged, mean effect on the flow.

### 3.1.1.2.2 Detached Eddy Simulation

Detached Eddy Simulation (DES) is a hybrid modeling approach, which combines features of both unsteady RANS and Large Eddy Simulation (LES) turbulence modeling, which is an inherently unsteady method which explicitly simulates the time-variation of the large eddies in a turbulent flow while the smaller eddies, with smaller length scales than the grid, are modeled via a turbulent model. DES utilizes RANS in the boundary layer and irrotational regions of the flow, while LES is used in unsteady separated

regions. The method has shown great utilization because of the potential for improved turbulent modeling for massively separated flows compared to RANS. DES is more computationally expensive than RANS because it requires a fine grid to resolve the turbulent eddies. Though RANS is used for all the propeller test cases, DES is used in for the tandem cylinder test case because of its capability to accurately capture the separated flow and vortices in the experiment.

### 3.1.2 Discretization and Solver Properties

STAR CCM+ converts the governing equations of motion into a coupled algebraic system of equations using a finite volume discretization. Both structured and unstructured grids can be solved using a number of different cell types. A number of features utilized in this thesis are outlined in this section.

#### Discretization Scheme

For simulations utilizing RANS, a second-order upwind discretization scheme was used and the inviscid fluxes are described using Liou's AUSM+ flux vector splitting scheme for coupled flows, as described in [103]. These equations can then be solved explicitly or implicitly in the software. For the DES simulations, a hybrid second-order upwind/bounded central differencing discretization is used for the convective terms.

#### Gradient Computation

The gradients in STAR CCM+ are computed by copying the (unlimited) reconstruction gradients followed by a method of limiting the gradients. The (unlimited) reconstruction gradients are computed using a Hybrid Gauss-Least Squares Method. The Venkatakrishnan limiter was used for gradient limiting

### Iterative Method

An implicit Gauss-Siedel relaxation scheme was utilized, with coupled flow and segregated pressure utilizing a Bi-Conjugate Gradient Stabilizing method.

### Algebraic Multigrid Solver

An algebraic multigrid solver (AMG) is used, which is a method which solves the discrete linear system of the governing equations iteratively, being efficient for sparse systems such as those presented in CFD. It solves the system of equations in the following manner:

1. It agglomerates cells to form coarse grid levels. It does this without reference to the underlying grid geometry or discrete equations, with coarse grid equations being derived from arithmetic combinations of the fine-grid coefficients.
2. It transfers the residual, which is the difference between the solutions of successive iterations, from a fine level to a coarser level (restriction).
3. It transfers the correction from a coarse level back to a finer level (prolongation).

It performs those steps in order to damp out large frequency components of the error in a solution, which are responsible for poor convergence. The two schemes for using a multigrid solver used in this thesis are a V-Cycle and a flex cycle.

- A fixed V-cycle performs a number of relaxation sweeps on the finest level and transfers them to a coarser level successively until the coarsest level has been reached. Then, the operation is repeated until the finest level is reached.

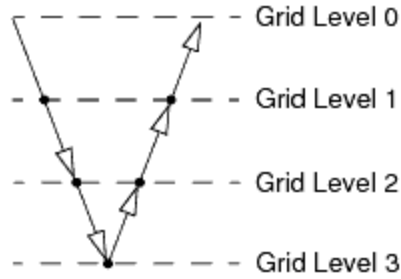


**Fig. 3.1: An illustration of a V-cycle of a Multigrid Solver with 4 Grid Levels [104].**

- A flexible (flex) cycle monitors residuals after every sweep on a given grid level, and if the ratio of the residuals exceeds a given threshold, the solution continues to a coarser level. Once a residual on a given level is reduced more than a specified tolerance, the solution moves to a finer level. Thus, it is more economical than other cycles.

A fixed V-cycle was used for coupled flow, segregated pressure, and segregated energy. A flex cycle was used for turbulence and segregated velocity. The AMG solver runs until it either performs a maximum number of cycles or until it reaches a convergence tolerance, the ratio by which the residuals of a linear system need to change before the multigrid solver stops. For all simulations, a convergence tolerance of 0.1 and 30 maximum cycles was used.

### Wall Function

A hybrid wall function was used for all simulations, incorporating a wall function into the prism layer mesh describing the mesh only if the  $y^+$  values are too big to resolve the boundary layer well without one.

## Convergence Criteria

Convergence criteria for simulations are discussed will be discussed in the following chapters which describe simulation results.

### **3.1.3 Solver Stability Characteristics**

Solver stability is an important issue as solutions that diverge cannot accurately describe flow. Though nearly every choice in CFD affects solution stability, a few important factors in solution stability are described.

#### Under-relaxation factors

Under-relaxation factors define how much a solution can change between iterations. These can be defined for various variables which are solved for in the system, including velocity, pressure, and turbulent terms. A higher under-relaxation factor results in a solution which converges more quickly as the flow is able to change more quickly between iterations. However, the trade-off is stability as solver and grid conditions can only support so much change between iterations.

#### CFL number

The Courant-Friedrich-Lowy (CFL), or Courant number, is a non-dimensionalized time step, whose value can be set to control stability criteria directly. It controls the size of the local time steps that are used to advance a solution in time. It plays the same role as under-relaxation factors. It is defined according to Eq. 3.5:

$$CFL = \sum_{i=1}^3 \frac{\Delta t u_i}{\Delta x_i} \quad (3.5)$$

Where  $\Delta t$  is the time step,  $u_i$  is the velocity, and  $\Delta x$  is the cell length in the dimension  $i$ . From the equation, it can be understood mathematically as the ratio of the flow velocity,

$u_i$  to the speed that the grid can resolve,  $\Delta x_i / \Delta t$ . In STAR CCM+, it is available for coupled flows. Lower CFL numbers are more stable, while higher CFL number can enable faster convergence. Generally, there is an optimal CFL number for a given simulation which balances the number of iterations required to resolve the flow while maintaining numerical stability of the solver. The CFL number is bounded by stability for implicit and explicit methods, with explicit methods having an upper bound of 1 at maximum except in the case where steady flows are applied with residual smoothing iterations in which case a value of 2 can be used.

### Grid Sequencing Method

Good initialization of the flow is extremely important in CFD. The closer an initial solution is to a final solution, the less it has to change between the initial and final solution. In many cases, solvers cannot resolve a flow with a poor initial condition. Additionally, a flow can resolve differently depending on how a solution is initialized due to a different development of flow conditions. A grid sequencing method is one method of initialization which successively solves the flow over a series of grids, ranging from a very coarse grid to the final grid utilized for the simulation. The flow is solved up to a certain condition, such as a particular number of iterations, for each grid in the process and then the solution is interpolated onto a finer grid which is subsequently solved. This enables the initial solution to populate the grid with a good base prediction of the flow in an efficient manner.

### Expert Driver

Many tools are used within CFD software to improve stability and convergence. STAR CCM+ offers an expert driver, which is an automated convergence control tool for

coupled implicit flows. It improves the robustness of the coupled solver by automatically modifying the CFL number and computing optimal under-relaxation factors for fast convergence during the course of the simulation.

### **3.1.4 Numerical Modeling of Aeroacoustics in STAR CCM+**

Aeroacoustics in CFD can be computed via direct methods, where the pressure is taken directly from the pressure fluctuations in the CFD domain, or via indirect or hybrid methods, where the acoustic field is solved separately from the aerodynamic field.

#### **3.1.4.1 Direct Methods**

Noise is generated through very small pressure fluctuations which are transmitted through a medium. Thus, if CFD is able to predict the pressure fluctuations caused by the noise sources in the domain, noise data can be simply garnered from the unsteady pressure data calculated. This is what is termed as direct methods for the numerical prediction of acoustics. This, however, is computationally expensive as the spatial and temporal resolution of the simulation needs to be extremely fine in order to accurately describe the rapid pressure fluctuations of high frequencies. This method is used for the tandem cylinder test case.

#### **3.1.4.2 Indirect Methods**

Lighthill introduced the acoustic analogy in two papers in 1952 and 1954 [9], [105] to understand and predict the noise generated by a jet. The acoustic analogy replaces regions of unsteady flow with an equivalent distribution of sources to derive linear perturbations from the base flow [9]. Essentially, the approach describes a case of small regions of noise-producing flow embedded within a homogenous fluid with constant density and

sound speed ( $c_0$ ). In this case, pressure fluctuations ( $p'$ ) at distances far from the noise source should behave like acoustic waves which satisfy the homogenous wave equation:

$$\frac{1}{c_0^2} \frac{\partial^2 p'}{\partial t^2} - \frac{\partial^2 p'}{\partial \mathbf{x}_i^2} = 0 \quad (3.6)$$

Lighthill manipulated the continuity and momentum equations in such a way that they reduce to the following form outside the region of the flow, as shown below:

$$\frac{1}{c_0^2} \frac{\partial^2 p'}{\partial t^2} - \frac{\partial^2 p'}{\partial \mathbf{x}_i^2} = \frac{\partial^2 \mathbf{T}_{Lij}}{\partial \mathbf{x}_i \partial \mathbf{x}_j} \quad (3.7)$$

where  $\mathbf{T}_{Lij} = \rho u_i u_j - \tau_{ij} + (p' - c^2 \rho') \delta_{ij}$  is known as the Lighthill Stress Tensor with  $p'$  representing fluctuating pressure. In order for this equation to satisfy the homogenous wave equation, this stress tensor must equal zero in the far field.

The Ffowcs Williams-Hawkins equation, one of the most popular far field noise prediction models, is based upon Lighthill's Acoustic Analogy. A complete derivation can be found in [106]. It treats body surfaces as having a mathematical discontinuity, created by mass and momentum sources which, also, act as noise generators. Outside of this surface, the flow is treated as having the same characteristics as the flow exterior to the surface. Mathematically, this is done by combining the continuity and momentum equations, along with the surface discontinuity, into a wave equation. If  $f(\mathbf{x}_1, \mathbf{x}_2, \mathbf{x}_3, t)$  is a function which describes the body, such that any value of  $f$  which is greater than 0 is outside the body, this equation can be written as:

$$\frac{1}{c_0^2} \frac{\partial^2 p'}{\partial t^2} - \frac{\partial^2 p'}{\partial \mathbf{x}_i^2} = \frac{\partial}{\partial t} [\rho_0 \mathbf{v}_n \delta(f)] - \frac{\partial}{\partial \mathbf{x}_i} [\mathbf{l}_i \delta(f)] + \frac{\partial^2}{\partial \mathbf{x}_i \partial \mathbf{x}_j} [\mathbf{T}_{Lij} H(f)] \quad (3.8)$$

where,  $\mathbf{v}_n$  is the local velocity normal to the surface,  $\mathbf{l}_i$  is the local force on the fluid per unit area, and  $H(f)$  is the heavyside function. The three terms on the right hand side of the equation describe thickness, loading, and quadrupole noise sources, respectively. Thus, the equation is often described in the form:

$$p'(\mathbf{x}, t) = p'_T(\mathbf{x}, t) + p'_L(\mathbf{x}, t) + p'_Q(\mathbf{x}, t) \quad (3.9)$$

where  $p'_T(\mathbf{x}, t)$  represents thickness noise,  $p'_L(\mathbf{x}, t)$  represents loading noise, and  $p'_Q(\mathbf{x}, t)$  represents quadrupole noise. Different solutions to this equation exist. The Farassat 1A formulation, having been applied and validated broadly, is a popular solution of the Ffowcs Williams-Hawkings equation for far field noise prediction of subsonic surfaces. It is used for both the STAR CCM+ simulations and SmartRotor simulations in this thesis. The derivation of the formulation is shown in [107].

Quadrupole noise can be computationally expensive to compute because of the volume integral required to calculate this noise source around the propeller blades. It is not computed in this thesis because it has a relatively small impact for test cases utilized in this thesis. Hanson [97] showed that quadrupole noise has a negligible effect outside of the transonic blade section speeds for thin propellers such as the SR-2 propeller simulated in this thesis. Based on a computation of quadrupole noise for a propeller of the same geometry as the propellers simulated in this work, Hanson calculated the contribution of quadrupole noise as shown in Fig. 3.2.

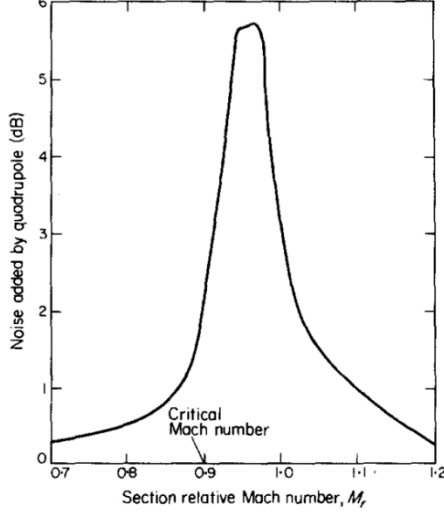


**Fig. 3.2: The effect of the quadrupole noise term at transonic speeds [97].**

For the two validation cases analyzed in this work, the tip speeds have helical tip Mach numbers 0.76 and 0.86 [12], [15]. Thus, the contribution of quadrupole noise is expected to be less than 1 dB and hence is neglected in the following simulations. The Farassat 1A formulation is shown below for thickness and loading noise only:

$$\begin{aligned}
& p'_T(x, t) = \\
& \frac{1}{4\pi} \left( \int_{(f=0)} \left[ \frac{\rho_0(\dot{\mathbf{U}}_n + \mathbf{U}_n)}{\mathbf{r}(1 - \mathbf{M}_r)^2} \right]_{ret} d\tilde{\mathbf{a}} \right. \\
& \quad \left. + \int_{(f=0)} \left[ \frac{\rho_0 \mathbf{U}_n [\mathbf{r} \dot{\mathbf{M}}_r + c_0 (\mathbf{M}_r - \mathbf{M}^2)]}{r^2(1 - \mathbf{M}_r)^3} \right]_{ret} d\tilde{\mathbf{a}} \right) \quad (3.10) \\
& p'_L(x, t) = \\
& \frac{1}{4\pi} \left( \frac{1}{c_0} \int_{(f=0)} \left[ \frac{\overline{\mathbf{L}_r}}{\mathbf{r}(1 - \mathbf{M}_r)^2} \right]_{ret} d\tilde{\mathbf{a}} + \int_{(f=0)} \left[ \frac{\mathbf{L}_r - \mathbf{L}_M}{\mathbf{r}^2(1 - \mathbf{M}_r)^3} \right]_{ret} d\tilde{\mathbf{a}} + \right. \\
& \quad \left. \frac{1}{c_0} \int_{(f=0)} \left[ \frac{\mathbf{L}_r [\mathbf{r} \overline{\mathbf{M}_r} + a_0 (\mathbf{M}_r - \mathbf{M}^2)]}{\mathbf{r}^2(1 - \mathbf{M}_r)^3} \right]_{ret} d\tilde{\mathbf{a}} \right)
\end{aligned}$$

where:

- $\mathbf{U}_i = \left(1 - \frac{\rho}{\rho_0}\right) \mathbf{v}_i + \frac{\rho \mathbf{u}_i}{\rho_0}$
- $\mathbf{M}_i = \frac{\mathbf{u}_i}{c_0}$
- $\mathbf{L}_i = \mathbf{P}_{ij} \mathbf{n}_i + \rho \mathbf{u}_i (\mathbf{u}_n - \mathbf{v}_n)$
- $\mathbf{P}_{ij} = (p - p_0) \delta_{ij} - \mathbf{T}_{v_{ij}}$  is the compressive stress tensor
- $\mathbf{u}_i$  represents fluid velocity in the  $x_i$  direction
- $\mathbf{u}_n$  is the fluid velocity component normal to the surface
- $\mathbf{n}_i$  is the surface normal vector
- $\mathbf{v}_i$  represents surface velocity in the  $x_i$  direction
- $\mathbf{v}_n$  is the surface velocity component normal to the surface
- $\rho_0$  and  $p_0$  are the far field density and pressure, respectively
- $\mathbf{r} = \mathbf{x}_{observer} - \mathbf{y}_{face}$
- $ret$  stands for retarded time
- A dot above a variable denotes the time derivative with respect to the source time of that variable.

The Ffowcs Williams-Hawkins surfaces ( $f$ ) can be defined in two different ways: using impermeable surfaces, which are defined by the boundaries of a solid object within the flow, and permeable surfaces, which are regions which include volumes of air outside of the body. Impermeable surfaces cannot compute quadrupole noise as they avoid the volume integral required to evaluate the third term in the Ffowcs Williams-Hawkins equation. Permeable surfaces are defined as regions where flow can enter and exit, enabling this computation as volumes in the flow are also defined as part of the region. Care must be taken when defining the boundaries of permeable surfaces as unsteady pressure fluctuations passing through this surface, such as those found in a separated wake or vortices, can be interpreted directly as noise. Thus, it is typical for permeable surfaces to encapsulate the entire wake of the flow.

### **3.1.5 Grid Generation in STAR CCM+**

In CFD, modeling broadly consists of three steps. First, a computational domain is generated which defines the simulated space. Second, appropriate boundary conditions are defined for the simulation. Third, the grid, or mesh, is generated to divide the computational domain into cells which are subsequently solved. Since the choice of the computational domain, boundary conditions, and grid represents unique challenges for propellers, we will overview briefly the relevant capabilities of STAR CCM+ in these areas.

The importance of a good grid in CFD is paramount, as resolution is required to describe the flow sufficiently and effectively given the equations being used to describe the flow. With a larger grid, computational time significantly increases. Thus, the best grids have high resolution in areas where the flow variables exhibit strong gradients to capture these in sufficient detail. In STAR CCM+, both structured and unstructured meshing is available. The fastest way to generate a grid for, or mesh, a volume is through unstructured meshing using tetrahedral cells. However, hexahedral and polyhedral cells generally provide more accurate and stable solutions compared to tetrahedral counterparts for lower cell counts. Therefore, these were utilized in this thesis. Structured meshes were used in all simulations near the wall, in a prism layer mesh, to capture the boundary layer.

#### **3.1.5.1 Trimmed Mesher**

The trimmed mesher in STAR CCM+ primarily utilizes hexahedral cells, bounded by 6 quadrilateral faces, to define the regions in space. This enables the creation of Cartesian, rectilinear, or curvilinear grids. To create the grid, a template grid is defined according to

the grid settings and the CAD surfaces are cut or “trimmed” out of the grid. It is advantageous for the following reasons:

- The hexahedral cells are aligned with a specified coordinate system and provide minimal cell skewness, leading to effective grids.
- Hexahedral cells provide straightforward refinement and growth rates in different regions of the grid.
- The grid works well with surfaces that are not well defined in the CAD model used to generate the surface.
- Large grids are easy to construct with parallel processes.

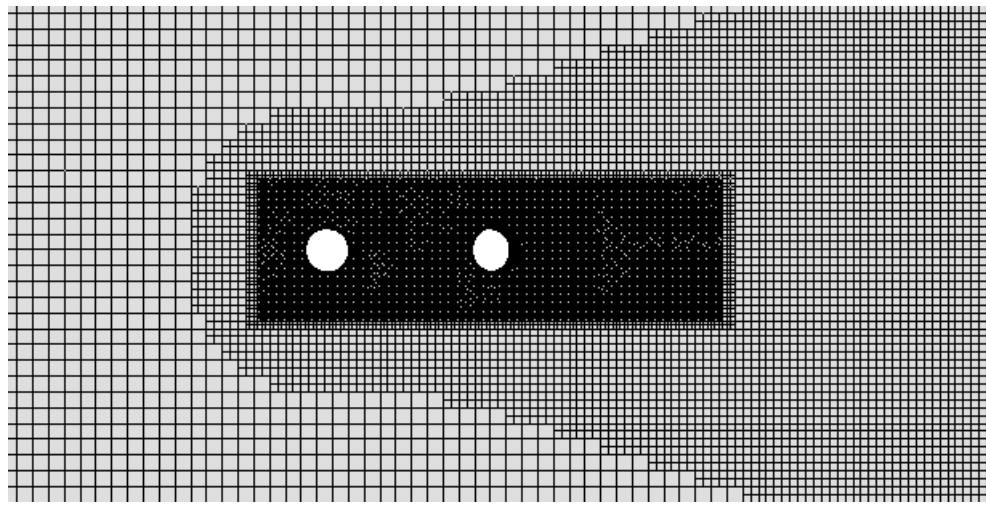


**Fig. 3.3: An example of a trimmed grid with different regions of refinement.**

### 3.1.5.2 Polyhedral Mesher

Polyhedral grids are efficient and easy to build, requiring about five times fewer cells than a tetrahedral grid to define a surface. An arbitrary polyhedral cell shape is used to build the core grid, typically having an average of 14 cell faces. The grid quality is dependent upon the quality of the CAD, unlike hexahedral cells. They can be more efficient than tetrahedral or hexahedral cells due of the following advantages:

- Because of the many cell faces (and, hence, neighboring cells), polyhedral cells allow gradients to be computed effectively.
- Because polyhedral cells contain a greater number of faces than hexahedral or tetrahedral cells, they have a greater number of optimal flow directions that can be computed with a single cell. For instance, a polyhedral cell with 12 faces has six optimal flow directions, while a hexahedral cell only has three (normal to each of the three parallel set of faces). This is particularly beneficial in complex flows such as recirculation.

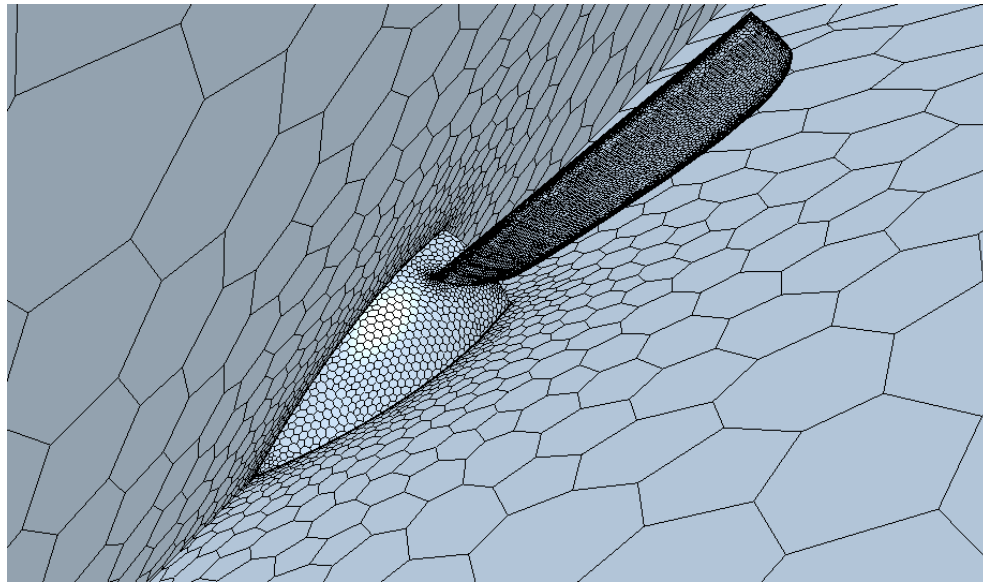


**Fig. 3.4: An example of a polyhedral grid around the blade of a propeller.**

### 3.1.5.3 Prism Layer Mesher

A prism or inflation layer grid is used alongside another meshing model to generate orthogonal prismatic cells next to wall surfaces or boundaries. It allows for a layering of cells with a defined thickness and growth distribution from layer to layer. A good near-wall prism layer is essential to capture boundary and near-wall flows effectively, which require accurate prediction of high temperature or velocity gradients. In order to resolve a

shear layer effectively, at least 10-20 cells are required in the cross-stream direction with greater numbers required for resolving the viscous sublayer. If only the gross flow features are required, grids with only a few prism layers can provide accurate results. As very small cells should be generated with prism meshers, suitable refinement for the application is required.

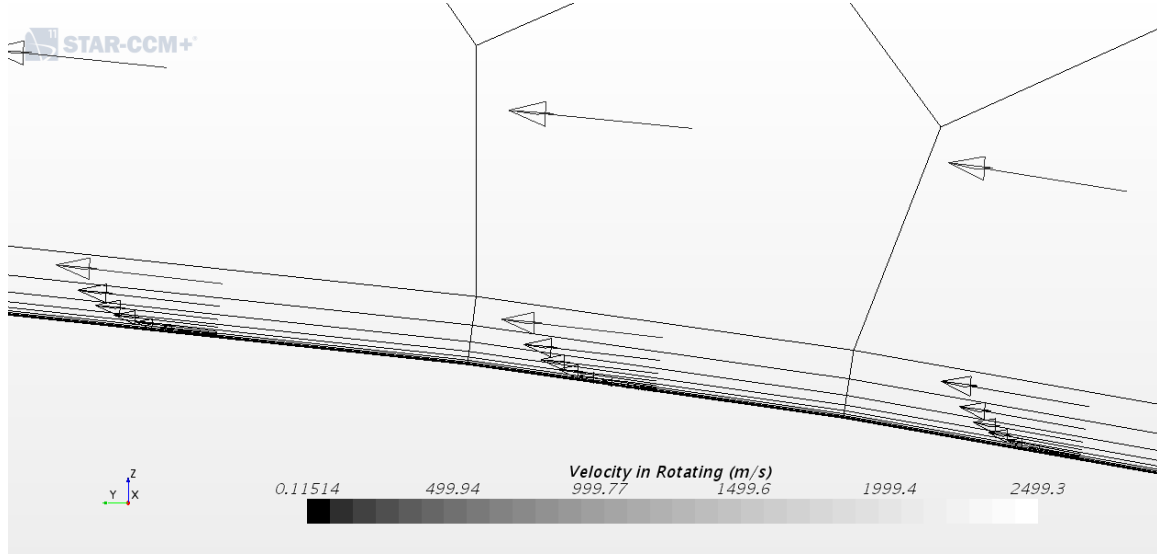


**Fig. 3.5:** A prism grid alongside a boundary showing the development of a velocity boundary layer.

### 3.1.5.4 Grid Extruder

A grid extruder simply copies an element of a grid and repeats it according to some spatial distribution function as can be seen in Fig. 3.6. This allows for the efficient generation of grids in the outer domains where refinement can be more simply defined.

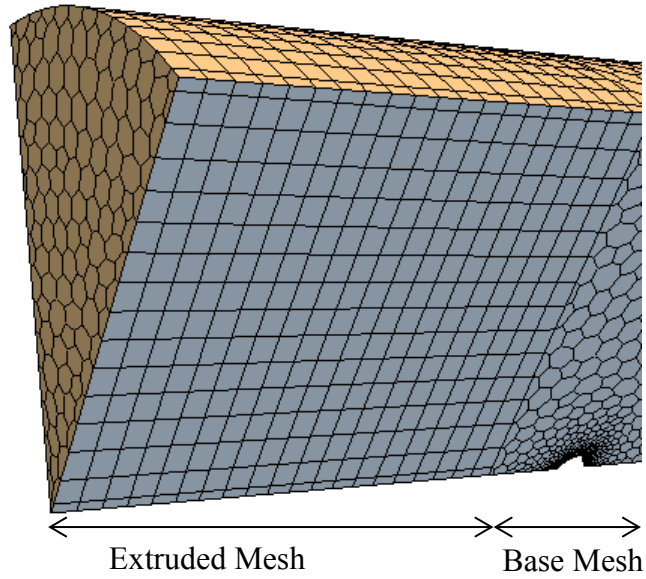


**Fig. 3.6: An example of grid extrusion.**

### 3.1.6 Sliding Mesh Method

In unsteady simulations, a sliding mesh method can also be utilized where part of the grid moves or rotates relative to another part of the grid. Thus, when the solution advances in time, the cell alignment changes within the domain and a different configuration is solved. This sliding mesh method is used for the unsteady propeller simulations in this thesis.

## 3.2 Overview of SmartRotor Code

This chapter provides an overview of the SmartRotor CFD code. The fundamental operating philosophy of SmartRotor is very different from STAR CCM+. While the latter one solves the governing equations using a grid of defined points in space, SmartRotor utilizes a panel method for solid surfaces, coupled with a Discrete Vortex Method for solving the wake [108], [109]. This can provide an accurate prediction of aerodynamic loading on the rotor blades at a computational cost which is orders of magnitude lower

than that of STAR CCM+ [110]. The big advantage of a Discrete Vortex Method is its ability to capture vortex aging more accurately than grid-based methods. On the other hand, this is an inherently incompressible method, introducing possible errors for cases where compressibility might be important.

### 3.2.1 Code Background

SmartRotor is a fully aeroelastic-aeroacoustic code consisting of three modules: aerodynamic, aeroacoustic, and a structural module. The aerodynamic component of the code is based on the GENeral Unsteady Vortex Particle (GENUVP) code developed at the National Technical University of Athens by Voutsinas et al. [111], [112]. GENUVP was initially developed for the modeling of wind turbines, but was extended to simulate rotorcraft [113], [114], wind turbines [115], and propellers. The acoustic component of the code was developed by Opoku at Carleton University [116] using the Ffowcs Williams-Hawkins Equation. SmartRotor also contains an aeroelastic component, jointly developed at M.I.T. by Cheng [117] and at Carleton by Opoku [116]. The aeroelastic component is not utilized in this thesis, i.e., it is assumed that the propeller blades were rigid. The code has also been further enhanced by the addition of a rigid rotor blade articulation model by Michael Martin [118]. At each step of the development of the Smartrotor code, validation studies have been performed according to the list below:

- In 2002, Opoku performed an aerodynamic, aeroacoustic, and aeroelastic validation of SmartRotor compared to the HELINOISE experiment [116].

- In 2008, Sean McTavish performed an aeroelastic and aeroacoustic validation of SmartRotor compared to the results of a National Energy Laboratory wind turbine experiment [115].
- In 2011, Michael Martin performed an aerodynamic validation of the predicted blade flapping for helicopter blades based on the E.D. Harris experiment [118].
- In 2016, David Boots extended the code to parallel processing as well as validated it for certain propeller and wake cases [55], [58].

Additionally, other validation studies have been performed on each module of the code during its development.

### 3.2.2 Numerical Modeling of Aerodynamics in SmartRotor

The details of the formulation of the GENUVP aerodynamic formulation can be found in [111]–[114], [119] but a brief description is given here. The code uses a panel method to compute the blade aerodynamic loads, and a discrete vortex method which estimates the path and rotations of vortex particles which are shed off the rotating blades. It can then predict the interaction with other blades and objects in the flow field. The method is essentially grid-free, enabling easy modeling of multiple rotating bodies within a flow-field.

The code is based on the Helmholtz decomposition, which suggests that the flowfield around a rotor ( $\mathbf{u}(\mathbf{x}, t)$ ) can be decomposed into both an irrotational ( $\vec{u}_{solid}$ ) and rotational component ( $\mathbf{u}_{near-wake}$  and  $\mathbf{u}_{far-wake}$ ):

$$\mathbf{u}(\mathbf{x}, t) = \mathbf{u}_{ext}(\mathbf{x}, t) + \mathbf{u}_{solid}(\mathbf{x}, t) + \mathbf{u}_{near-wake}(\mathbf{x}, t) + \mathbf{u}_{far-wake}(\mathbf{x}, t) \quad (3.11)$$

where  $\mathbf{u}_{ext}$  represents the external velocity field,  $\mathbf{u}_{solid}$  is the velocity field due to the interference of solid bodies such as rotor blades, and  $\mathbf{u}_{near-wake}$  and  $\mathbf{u}_{far-wake}$  represent the velocities influenced by the near and far wake, respectively.  $\mathbf{u}_{ext}$  is specified by the boundary conditions of the system,  $\mathbf{u}_{solid}$  and  $\mathbf{u}_{near-wake}$  are defined by the use of a panel method, and  $\mathbf{u}_{far-wake}$  is evaluated using a free-wake vortex method. This method tracks all of the vortex particles individually in order to describe account for their effect, thus, becoming more computationally expensive with each time step as more vortex particles are tracked. In order to solve for  $\mathbf{u}_{solid}$  and  $\mathbf{u}_{near-wake}$  using a panel method, potential flow equations must be solved by discretizing the surfaces of the bodies and wakes into panel elements. This enables the flow to be solved as a system of linear equations.

The flow field begins as the defined  $\mathbf{u}_{ext}$ , after which point the boundary conditions and bodies within the flow field, described by  $\mathbf{u}_{solid}$ , interact with the flow particles to generate the initial near wake particles using the panel method described. These then become far-wake particles in successive time steps and are solved with a free wake particle method, coupling the two methods together. Once the simulation has converged, all the various components of  $\mathbf{u}$  interact to describe the final flow field.

### 3.2.2.1 Brief Overview of Panel Method

A complete derivation of the panel method utilized by SmartRotor to calculate aerodynamic loads is not provided here because of the broad application and

understanding of such panel methods. The method is based on the work by Hess [120], [121] and assumes incompressible and inviscid potential flow. A concise summary and derivation of its application in SmartRotor can be found in [55], but a condensed version of the derivation follows:

1. The method assumes incompressible and inviscid flow, thus the Navier-Stokes Equations of Eq. 3.1 is reduced to the Laplace equation in Eq. 3.11 for velocity potential,  $\phi$ , which is defined according to  $\mathbf{u} = \nabla \cdot \phi$ . The flow is constrained to be regular and not penetrate solid boundaries.

$$\nabla \cdot \mathbf{u} = \nabla^2 \phi = 0 \quad (3.11)$$

2. General solutions for the flow are constructed with Green's identity, using continuous source distributions for non-lifting bodies, dipole distributions for thin lifting bodies and the wake, and source and dipole distributions for thick airfoils. The velocity potential,  $\phi$ , induced at a given point  $\mathbf{P}$  is found by integrating the source intensity,  $\sigma$ , and dipole intensity,  $\mu$ , over the lifting, non-lifting, and wake surfaces:

$$\begin{aligned} \phi(\mathbf{P}) = -\frac{1}{4\pi} & \left( \int_{lifting} \mu \mathbf{n} \cdot \nabla \left( \frac{1}{\tilde{r}} \right) d\tilde{\mathbf{a}} + \int_{non-lifting} \sigma \left( \frac{1}{\tilde{r}} \right) d\tilde{\mathbf{a}} \right. \\ & \left. + \int_{near-wake} \mu \mathbf{n} \cdot \nabla \left( \frac{1}{\tilde{r}} \right) d\tilde{\mathbf{a}} \right) \end{aligned} \quad (3.12)$$

where  $\tilde{r}$  represents the distance from a given element to the evaluation point and  $d\tilde{\mathbf{a}}$  represents a differential surface area.

3. A boundary condition in such an analysis requires the non-penetration of solid boundaries,  $\nabla\phi = \mathbf{u}_{ext} \cdot \mathbf{n} - \mathbf{F}$  where  $\mathbf{F}$  is the local normal velocity due to the motion of the body and the far-wake induced velocity. This leads to the governing equation of the panel method:

$$-\frac{1}{4\pi} \left( \int_{lifting} \mu \nabla \left( \frac{\partial}{\partial n} \frac{1}{\tilde{r}} \right) d\tilde{\alpha} + \int_{non-lifting} \sigma \nabla \left( \frac{1}{\tilde{r}} \right) d\tilde{\alpha} + \int_{near-wake} \mu \nabla \left( \frac{\partial}{\partial n} \frac{1}{\tilde{r}} \right) d\tilde{\alpha} \right) \cdot \mathbf{n} = \mathbf{u}_{ext} \cdot \mathbf{n} - \mathbf{F} \quad (3.13)$$

4. The surfaces of the bodies and the wake are discretized into panel elements so that Eq. 3.13 can be approximated as a system of linear equations.

$$[\mathbf{C}_{ij}^{lifting}] \{\mathbf{u}_j\} + [\mathbf{C}_{ik}^{near-wake}] \{\mathbf{u}_k\} + [\mathbf{C}_{il}^{non-lifting}] \{\sigma_l\} = \{\mathbf{u}_{ext} \cdot \mathbf{n} - \mathbf{F}_i\} \quad (3.14)$$

where  $\mathbf{C}$  represents constant matrices of influence coefficients, with elements  $i, j, k, l$  ranging from 1 to  $N_{lifting} + N_{non-lifting}, N_{lifting}, N_{near wake}$ , and  $N_{non-lifting}$ , respectively where  $N$  represents the number of panels on the specified,. A visualization of the panels on the SR-2 propeller is shown in Fig. 3.7.

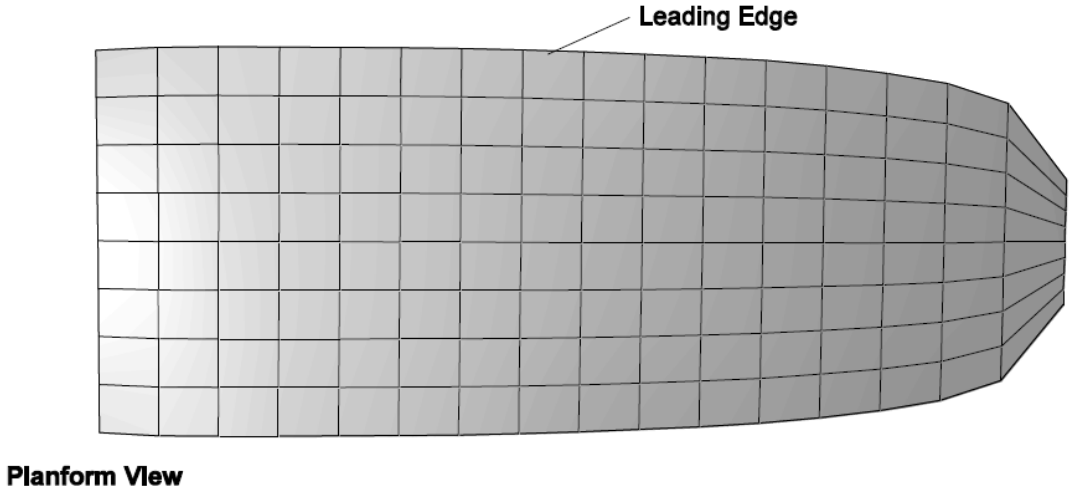


**Fig. 3.7: Panels Generated on an SR-2 Propeller [58].**

5. To enable unique solutions to Eq. 3.14, the dipole intensities of each near-wake element need to be set equal to the value of the adjacent emitting elements on the lifting body along the trailing edge and tip [113]. The geometry of the near wake is then determined from the flow velocity at the edges from which the wake is emitted.
6. Eq. 3.14 is solved for necessary source and dipole distributions. From this, the velocity potential can be calculated from Eq. 3.12. The velocity field can then be calculated using the following equation:

$$\mathbf{u}_{near\ wake} + \mathbf{u}_{solid} = \nabla\phi \quad (3.15)$$

where  $\vec{u}_{solid}$  is the sum of the lifting and non-lifting solid bodies.

The pressure distribution and potential loads can be calculated from the unsteady Bernoulli equation:

$$C_p = 1 - \frac{\mathbf{u}^2}{u_{ref}^2} - \frac{2}{u_{ref}^2} \frac{\partial\phi}{\partial t} \quad (3.16)$$

where  $u_{ref}$  is the freestream velocity. In this work, only thin lifting surfaces are utilized to model the propeller, so the formulation for thick and non-lifting bodies is not applied in this case. On thin lifting bodies, SmartRotor also corrects the load distribution to account for the leading edge suction force.

### 3.2.2.2 Overview of the Free Vortex Method

If incompressible flow is assumed,  $\nabla \cdot \mathbf{u} = 0$  from which the Laplace equation is obtained (3.11). We can satisfy the definition of vorticity,  $\omega = \nabla \times \mathbf{u}$ , and Eq. 3.17 with a vector stream function  $\Psi$  such that  $\mathbf{u} = \nabla \times \Psi$  since the divergence of a curl is always zero:

$$(\nabla \cdot \mathbf{u}) = \nabla \cdot [\nabla \times \Psi] = 0 \quad (3.17)$$

Substituting 3.18 into 3.17 yields a Poisson equation :

$$\omega = \nabla \times \mathbf{u} = \nabla \times [\nabla \times \Psi] = \nabla \cdot [\nabla \times \Psi] - \nabla^2 \Psi = -\nabla^2 \Psi \quad (3.18)$$

This equation has a well-known solution, which can be integrated along a vortex line for the velocity induced by a vortex filament. This solution, the Biot-Savart Law, enables the definition of the velocity field of a vortex:

$$\mathbf{u}_{far-wake}(\mathbf{x}, t) = \int_{D_\omega} \frac{\omega(\mathbf{x}_0, t) \times (\mathbf{x} - \mathbf{x}_0)}{4\pi|\mathbf{x} - \mathbf{x}_0|^3} dD \quad (3.19)$$

where  $\omega$  is vorticity,  $D_\omega$  is the domain of the far-wake calculations,  $\mathbf{x}$  is a position vector, and  $\mathbf{x}_0$  is a position vector of a point of a vortex.

The vortex particle method used by SmartRotor is a free wake vortex particle method, which develops the shape of the wake as the simulation progresses using vorticity

transport equations. The method treats the wake as a cloud of vortex particles, each with vector quantities of position, velocity, and intensity. The Biot Savart Law (Eq. 3.19) is applied to the vortex particles to determine the effect on the surrounding velocity field.

From Eq. 3.19,  $D_\omega$  is decomposed into volume elements with a vortex particle assigned to each one. If  $\Omega_j(t)$  is the vorticity and  $\mathbf{Z}_j(t)$  is the position of a given vortex particle j, vorticity can be defined:

$$\Omega_j(t) = \int_{D_{\omega,j}} \omega(x, t) dD \quad (3.20)$$

Such that,

$$\omega(\mathbf{x}, t) = \sum_j \Omega_j(t) \delta(\mathbf{x} - \mathbf{Z}_j(t)) \quad (3.21)$$

$$\Omega_j(t) \times \mathbf{Z}_j(t) = \int_{D_{\omega,j}} \omega(\mathbf{x}, t) \times \mathbf{x} dD \quad (3.22)$$

The far wake velocity from Eq. 3.19 can then be expressed as Eq. 3.23. However, this equation is highly singular, so a smooth approximation developed by Beale and Majda [122] is used to yield Eq. 3.24

$$\mathbf{u}_{far-wake}(\mathbf{x}, t) = \sum_j \frac{\Omega_j(t) \times (\mathbf{x} - \mathbf{Z}_j(t))}{4\pi |\mathbf{x} - \mathbf{Z}_j(t)|^3} \quad (3.23)$$

$$\begin{aligned} \mathbf{u}_{far-wake}(\mathbf{x}, t) &= \sum_j \frac{\Omega_j(t) \times (\mathbf{x} - \mathbf{R}_j(t))}{4\pi \mathbf{R}_j(t)^3} f_\varepsilon(\mathbf{R}_j(t)) \\ \mathbf{R}_j(t) &= \mathbf{x} - \mathbf{Z}_j(t) \end{aligned} \quad (3.24)$$

$$f_\varepsilon(\mathbf{R}_j(t)) = 1 - e^{-(\mathbf{R}_j/\varepsilon)^3}$$

where  $\varepsilon$  is the cut-off length for the vortex particles. This changes the method from a vortex particle method to a vortex blob method which have proven to be automatically adaptive, stable, convergent, and of arbitrarily high-order accuracy [123]. SmartRotor, for instance, uses a second-order space and time discretization. The vortex blobs are then convected in the Lagrangian sense, according to Eq.s 3.25 and 3.26:

$$\frac{d\mathbf{Z}_j(t)}{dt} = \mathbf{u}(\mathbf{Z}_j, t) \quad (3.25)$$

$$\frac{d\boldsymbol{\Omega}_j(t)}{dt} = (\nabla \boldsymbol{\Omega}_j(t)) \mathbf{u}(\mathbf{Z}_j, t) = \vec{D} \cdot \boldsymbol{\Omega}_j \quad (3.26)$$

Where  $\vec{D}$  is the deformation tensor.

### 3.2.3 Numerical Modeling of Aeroacoustics in SmartRotor

The aeroacoustic prediction in SmartRotor is based upon the Farrasat 1A solution to the Ffowcs Williams-Hawkings equations without quadrupole source terms as described in Section 3.1.4.2. The code treats each panel used for the panel method as an acoustic source, computing the acoustic results from the aerodynamic results at each time step. This produces an acoustic pressure signal for each defined microphone location. Though this part of the code has been validated for propellers in previous work as described in a recent work by Boots [55], additional simulations will be performed for comparison to STAR CCM+ data and to compute additional noise data for the same test case considered by Boots [55].

### 3.2.4 Limitations of SmartRotor Code

The SmartRotor code is an efficient and effective way to predict propeller noise, subject to some limitations:

1. The vortex panel method requires subsonic flow.
2. Both the panel and vortex method use incompressible flow. However, because aerodynamic performance data is based upon airfoil performance lookup tables, the method can predict transonic speeds if the tables include accurate data for those Mach numbers. In a similar way, even though viscosity is not directly modeled via the panel method, it is taken into account on the surface of the blades by the airfoil performance lookup tables.
3. The method only produces surface noise data, and thus quadrupole noise cannot be computed. As discussed in Section 3.1.4.2, this is not a significant source of error in the simulations which are run.
4. The code is limited by the accuracy of the aerodynamic lookup tables used to derive the forces on the blade. Thus, any non-wake effects not taken into account in the lookup tables will not be predicted.

SmartRotor simulations become less efficient with an increasing number of blades and as the solution advances in time, because the number of wake particles increases.

### **3.3 Impact of Simulation Properties on Aeroacoustic Prediction**

The prediction of mean aeroacoustic properties is much more difficult than the prediction of mean aerodynamic properties because they are heavily bounded by time and grid properties. The Nyquist sampling criterion states that, at minimum, a signal needs to be sampled at twice its frequency in order to be able to describe it. Thus, the highest frequency which can be predicted by a given simulation is bounded by double the time

step. Similarly, the lowest frequency which can be predicted by a simulation is determined by half of the simulation duration. For example, a 5 second simulation with a time step of 0.1 seconds can only, at best, resolve frequencies from 0.4 to 5 Hz. In practice, simulation durations and time steps need to be set significantly higher (i.e., by an order of magnitude) from these minimums.

In STAR CCM+, the temporal and spatial discretization schemes are also important. The temporal discretization scheme, which defines the impact of the advancement of a solution in time, can significantly impact the accuracy of an aeroacoustic simulation. For better accuracy, a second-order scheme, rather than a first-order scheme, is recommended as it more accurately describes the change in the flow between each time step. In addition, the maximum frequency which can be predicted in STAR CCM+ is dependent upon the spatial discretization (i.e., the size of the grid) as the sound pressure predicted depends upon the fluctuation rate that can be predicted. The minimum cell count required to represent an acoustic eddy is 2 cells per direction. Thus, a finer grid enables the calculation of smaller frequencies, while a coarser grid can only resolve large frequencies.

### **3.4 Computational Facilities Utilized**

The computational work was performed on three different computing platforms, with characteristics listed in Table 3.1. Thus, simulations were limited to what was feasible with these systems.

**Table 3.1: Computational Platforms Utilized for Simulations**

<b>System</b>	<b>Operating System</b>	<b>Number of Processors</b>	<b>Processor Type</b>	<b>Processor Speed</b>	<b>Physical Memory</b>
Desktop Computer	Windows 8.1 Pro	6	Intel Core i7-5820K x64	3.3GHz	16 GB
Clusterq (Carleton University)	LINUX	30	Intel Xeon X5450 x64	3.0 GHz	128 GB
High Performance Computing Virtual Laboratory (HPCVL)	LINUX	40	Intel Xeon E7-4860 x64	2.27 GHz	256 GB

## Chapter 4: Tandem Cylinder Test Case

As discussed in Chapter 2, a number of test cases were selected for validation using the CFD codes studied in this work. The first is a very well established case experimentally and numerically, and is simulated here to investigate the capability of STAR CCM+ in predicting noise.

This numerical study focuses on matching the average pressure coefficient measured around the cylinders at various locations of theta ( $\theta$ ), as seen in Fig. 2.2, for both the upstream and downstream cylinders. The noise emitted from the surface of the upstream cylinder at  $\theta = 135$  degrees, the location where the vortices are shed from the upstream cylinder onto the downstream cylinder, will also be compared. Also compared will be the noise emitted from the surface of the downstream cylinder at  $\theta = 45$  degrees, the approximate location where the vortices primarily impinge upon the second cylinder.

### 4.1 Simulation Setup

#### 4.1.1 Boundary Conditions and Grid Generation

The domain extended a distance of  $15D$  from the surface of each cylinder, with a thickness of  $3D$  (Fig. 4.1). It should be noted that the spanwise correlation studies have shown that domains with spanwise thicknesses of  $3D$  cannot fully resolve all of the spanwise effects of the unsteady flow on both cylinders [94], however, this thickness was chosen in order to keep computational time low.

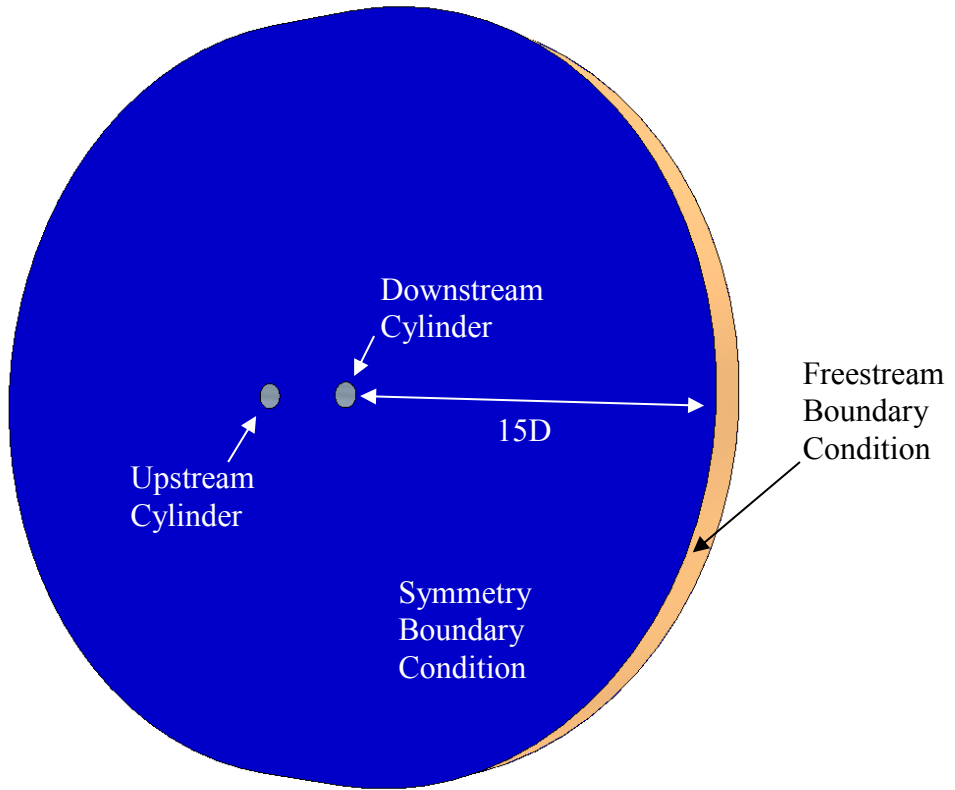


**Fig. 4.1: Computational domain and boundary conditions of tandem cylinder case.**

The boundary conditions are summarized in Table 4.1. An overset Cartesian grid (Fig. 4.2 and Fig. 4.3) was constructed with hexahedral cells with properties outlined in Table 4.2, containing 5 different levels of refinement, as outlined in Table 4.3.

**Table 4.1: Boundary Conditions of Tandem Cylinder Test Case**

Boundary	Type	Values
<b>Radial Boundary</b>	Freestream	$M = 0.128$ $Re = 166,000$
<b>Sides of Domain (Perpendicular to Cylinder Span)</b>	Symmetry Plane	
<b>Cylinder Surfaces</b>	Wall (No-Slip)	Roughness Height = 0.05 mm

**Table 4.2: Grid Properties for Tandem Cylinder Test Case**

Grid Property	Value
<b>Number of Cells</b>	5,200,535
<b>Prism Layers</b>	25
<b>Prism Layer Stretch Factor</b>	1.5
<b>Prism Layer Thickness</b>	$1.786 \times 10^{-3}$ m

**Table 4.3: Refinement Regions of Overset Grid**

Refinement Region as Seen in Fig. 4.2 and Fig. 4.3	Cell Size (m)	Cell Size (Diameters)
<b>A</b>	$2.86 \times 10^{-2}$	50%
<b>B</b>	$1.43 \times 10^{-2}$	25%
<b>C</b>	$3.57 \times 10^{-3}$	12.5%
<b>D</b>	$1.79 \times 10^{-3}$	6.3%
<b>E</b>	$8.93 \times 10^{-4}$	3.1%

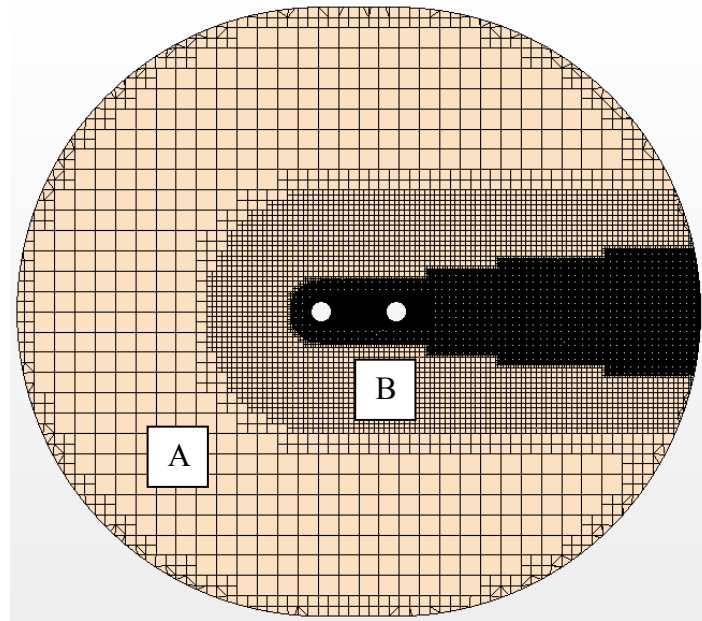


**Fig. 4.2: A planar cut of the entire grid showing refinement regions A and B.**

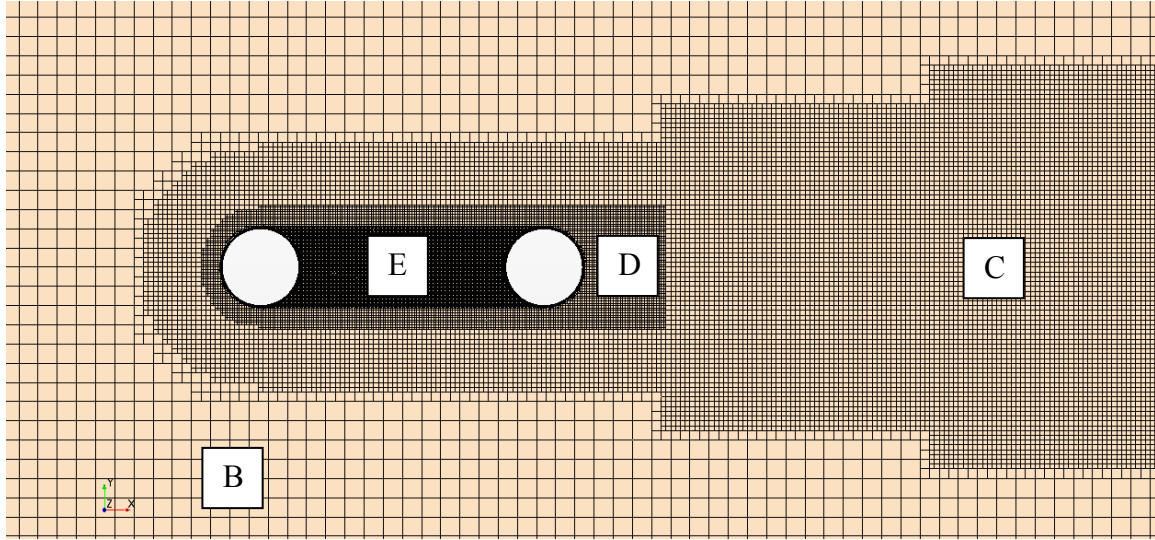


**Fig. 4.3:** Grid refinement around cylinders showing refinement regions B, C, D, and E.

#### 4.1.2 Solver Selection and Simulation Properties

The solution was initialized with a steady state solution from a segregated flow solver.

The properties utilized for the simulation are listed in Table 4.4 and Table 4.5.

**Table 4.4: Solver Properties for Tandem Cylinder Test Case**

Solver Category	Method
<b>Time</b>	Implicit Unsteady
<b>Flow</b>	Segregated Flow
<b>Turbulence Model</b>	Detached Eddy Simulation SST Menter K-Omega
<b>Temporal Discretization</b>	2 <sup>nd</sup> Order
<b>Velocity Under-Relaxation Factor</b>	0.7
<b>Pressure Under-Relaxation Factor</b>	0.5
<b>Turbulence Under-Relaxation Factor</b>	0.8
<b>Acoustic Solver</b>	Direct

**Table 4.5: Simulation Properties for Tandem Cylinder Test Case**

Property	Value
<b>Simulation Length</b>	0.35 s 35000 time steps
<b>Time step</b>	$1 \times 10^{-5}$ s
<b>Inner Iterations per time step</b>	8
<b>CPUs Utilized</b>	30 (Clusterq)
<b>Wall clock time per time step</b>	101 sec
<b>Total wall clock time</b>	982 hours

## **4.2 Convergence Criteria**

For this simulation, two orders of magnitude of reduction in all relative residuals was achieved between each time step except for the continuity residual, which only reduced by a single order of magnitude.

## **4.3 Verification**

A grid refinement study was done utilizing a series of five different grids with increasing refinement, ranging from 1.5 to 5.2 million cells. Three different time steps were tested, ranging from  $2.5 \times 10^{-5}$  to  $5 \times 10^{-6}$  seconds. The focus of the tandem cylinder simulation was to capture the pressure coefficient results and surface noise data reasonably before moving on to more complicated propeller cases. The verification is incomplete because of computational limitations (see Table 4.5 for run times). The unsteady nature of the flow on a 5.6 million cell mesh reached the limits of the available computational facilities and prohibited further refinement of the mesh. However, this study was viewed as a test case for learning about the aeroacoustic capabilities of STAR CCM+ rather than the ultimate goal of the research work which focuses on propellers. Thus, validation was only carried out on the finest mesh on which simulations could be run.

The simulations performed as part of the verification process for the Tandem Cylinder Case are listed in Table 4.6.

Table 4.6: Verification Studies for Tandem Cylinder Test Case

Simulation ID	Grid Size (Million Cells)	Time Step Size (s)	Iterations Per Time Step	Simulation Length After Initial Transient (s)
A	1.5	$2.5 \times 10^{-5}$	5	0.09345
B	1.5	$2.5 \times 10^{-5}$	5	0.25
C	1.7	$1.0 \times 10^{-5}$	5	0.20
D	1.7	$5.0 \times 10^{-6}$	8	0.0512
E	2.2	$2.5 \times 10^{-5}$	6	0.25
F	3.4	$2.5 \times 10^{-5}$	5	0.25
Final	5.2	$1.0 \times 10^{-5}$	8	0.20

Under relaxation factors were set to ensure a residual decline of two orders of magnitude across each time step. The  $C_p$  distributions and noise results of the verification data from simulation E and F are shown in Fig. 4.4-Fig. 4.7. Simulations A-E failed to capture the peak of the on the downstream cylinder, as seen in Fig. 4.7.

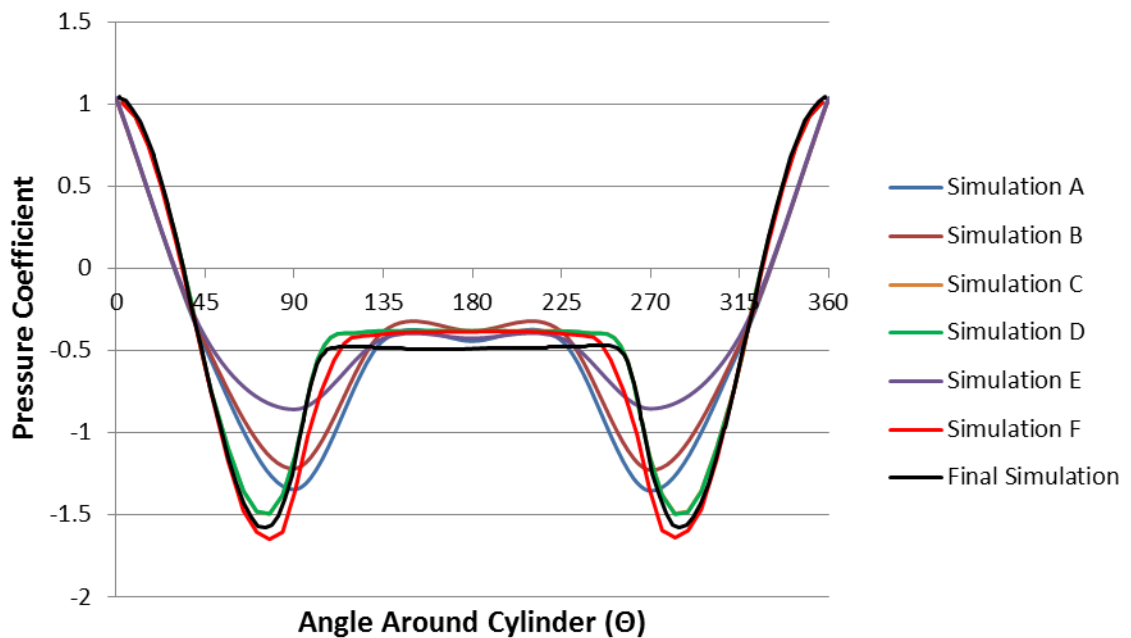
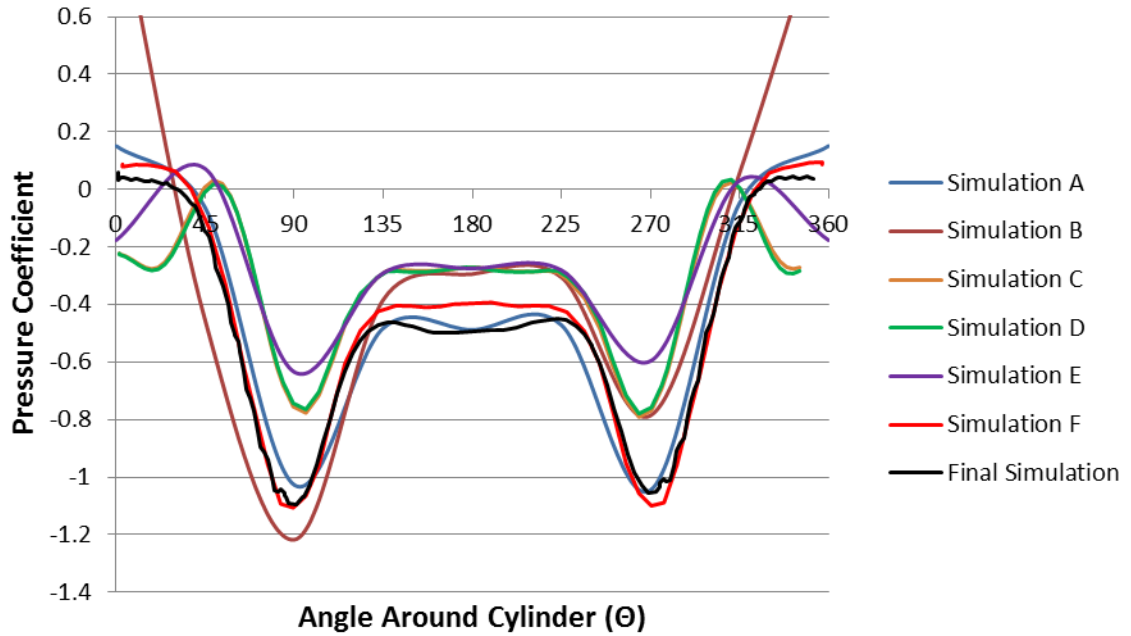
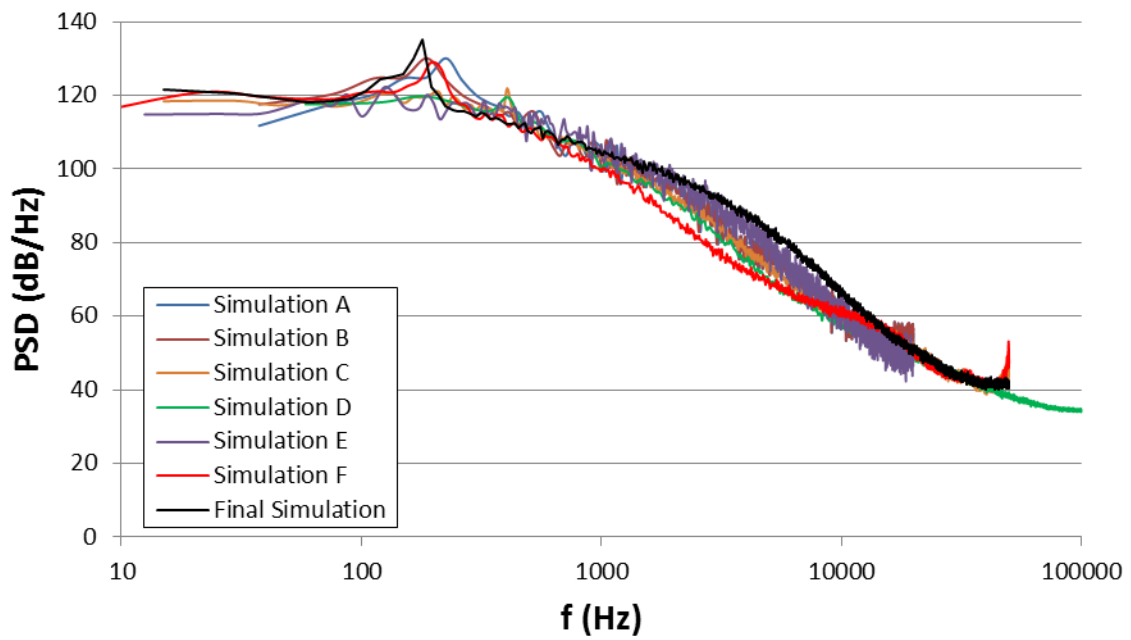


Fig. 4.4: Average  $C_p$  values of upstream cylinder for verification simulations.



**Fig. 4.5:** Average  $C_p$  values of downstream cylinder for verification simulations.



**Fig. 4.6:** Power spectral density values for pressure probe at  $\theta = 135^\circ$  on upstream cylinder for verification simulations.

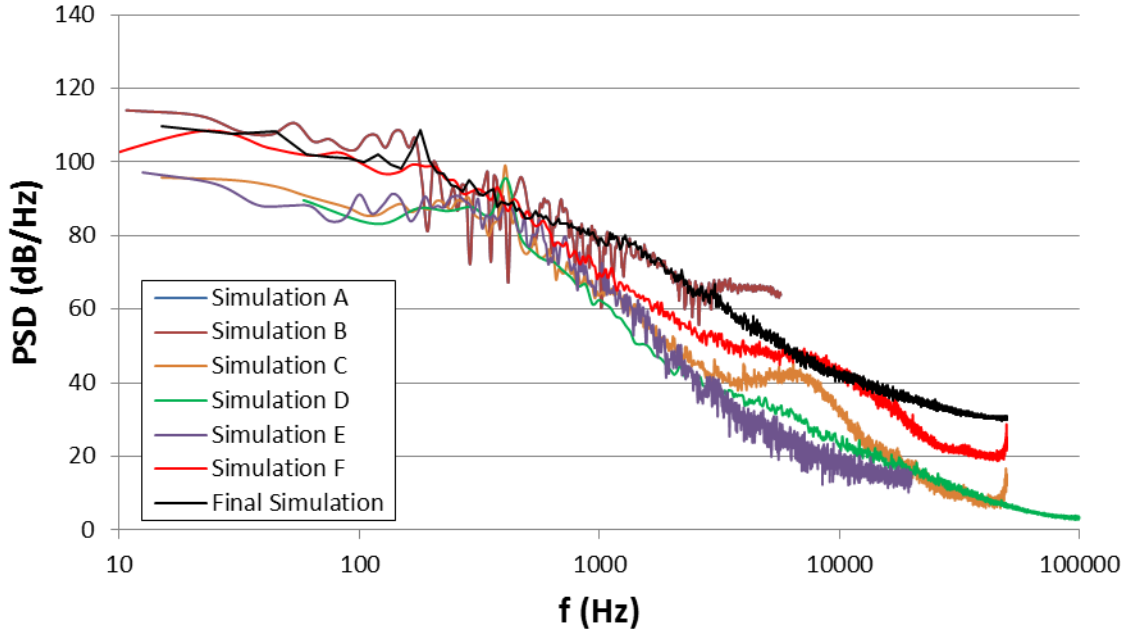


**Fig. 4.7: Power spectral density values for pressure probe at  $\theta = 45^\circ$  on downstream cylinder for verification simulations.**

## 4.4 Validation

### 4.4.1 Average Pressure Coefficient Results

As can be seen in the density contours in Fig. 4.8, the simulation predicts the unsteady shear layer rollup and shedding of vortices from both cylinders, with the vortices of the upstream cylinder impinging upon the downstream cylinder. The average pressure coefficient is plotted around each cylinder, which, particularly, shows the shedding locations from each cylinder and the average pressure in the wake after each cylinder. The average pressure is averaged across the span and compared to the experimental values in Fig. 4.9 (the upstream cylinder) and Fig. 4.10 (the downstream cylinder), in which the angle around the cylinder,  $\theta$ , is defined as in Fig. 2.2.

The upstream cylinder shows excellent comparison to experimental values except for a higher prediction of the pressure coefficient at the vortex shedding points (approximately 90° and 135°). The downstream cylinder also shows a higher prediction of pressure coefficient at the vortex shedding points, with a lower predicted pressure coefficient along the upstream face of the cylinder (0°-30° and 330°-360°). It is expected that better initialization of the turbulent boundary layer on the upstream cylinder and a finer grid between and around the immediate vicinity of the two cylinders can improve these predictions.

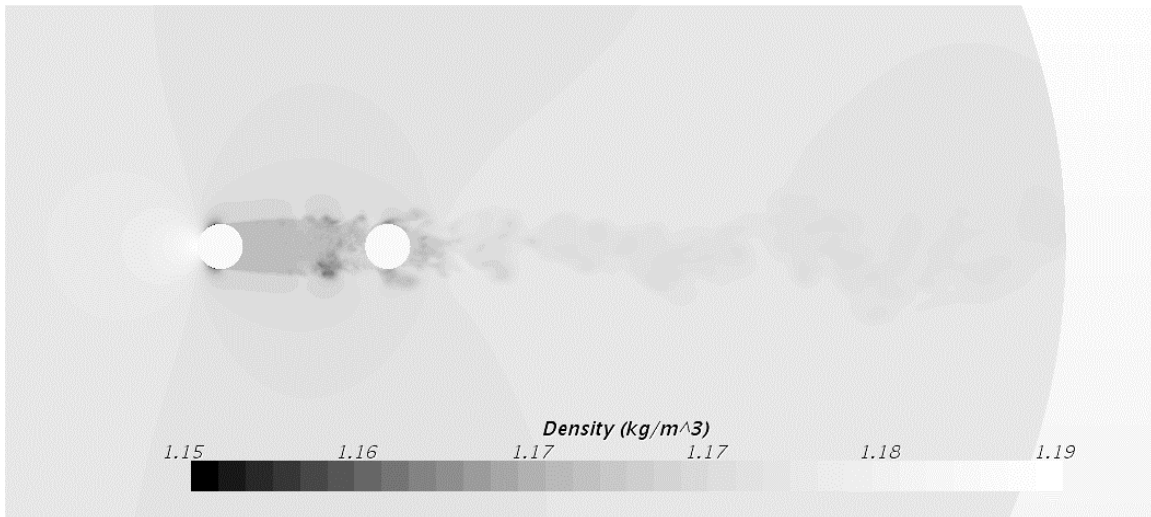


**Fig. 4.8: Instantaneous density contours of tandem cylinder test case.**

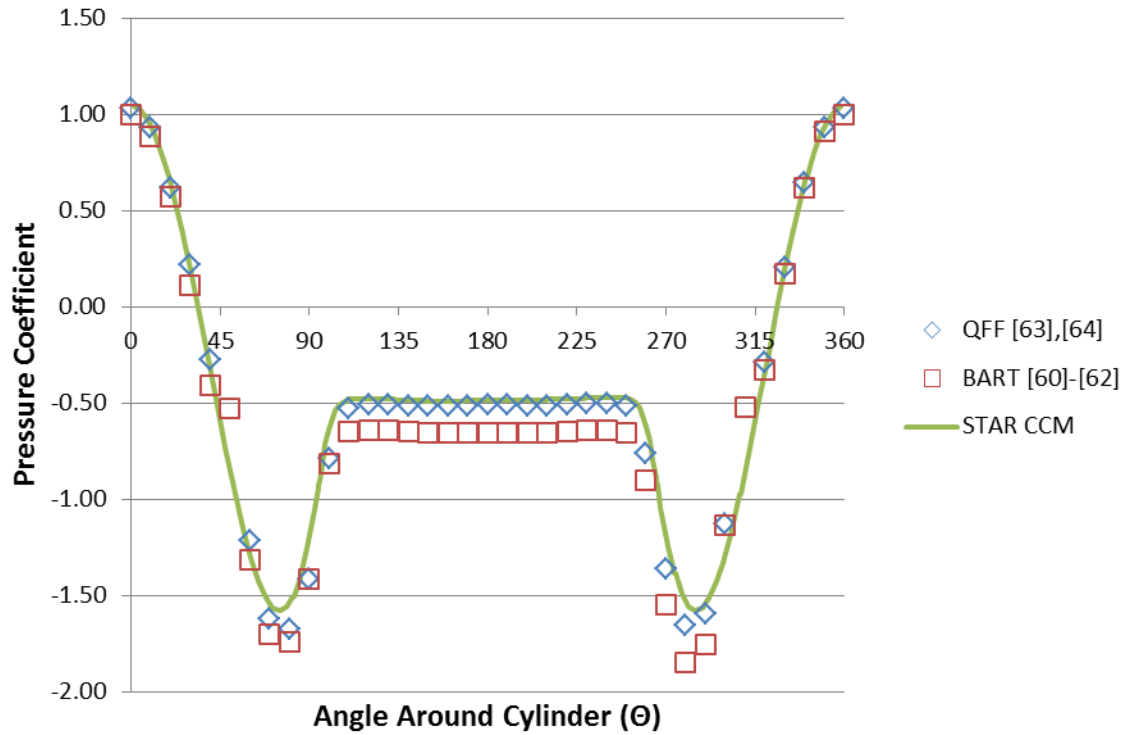


Fig. 4.9: Average pressure coefficient values of upstream cylinder.

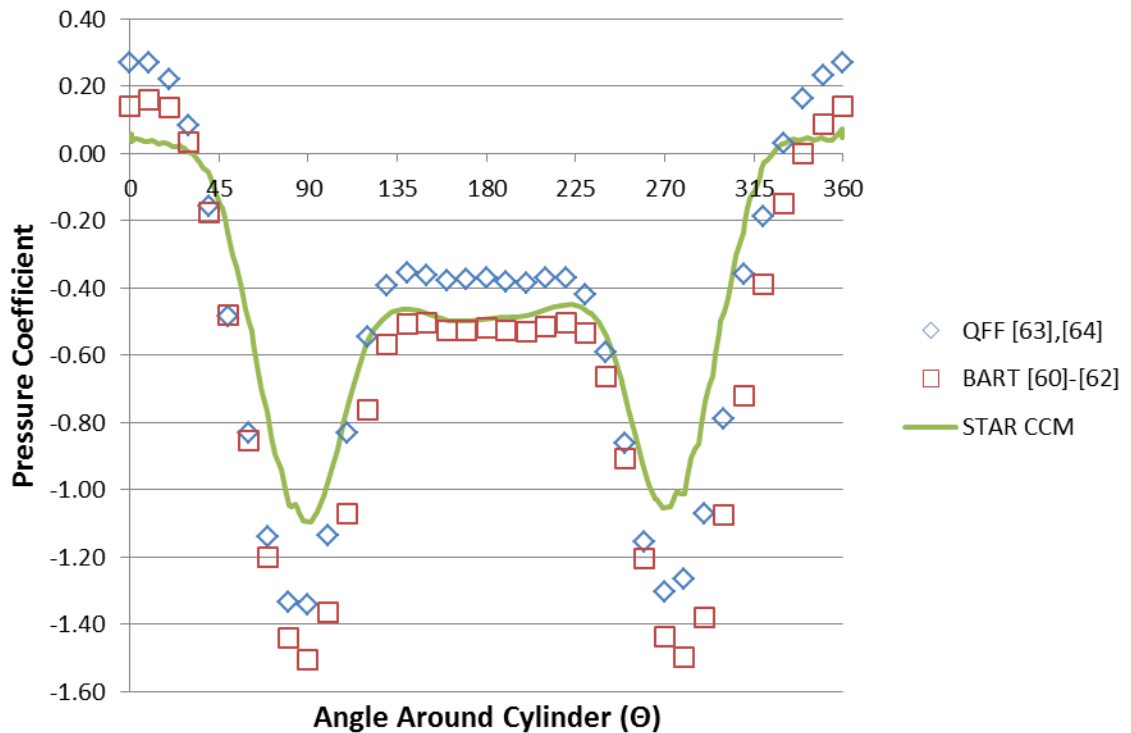
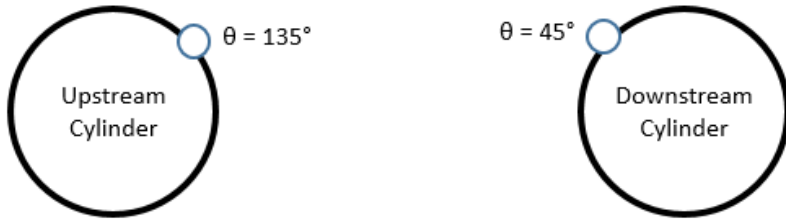


Fig. 4.10: Average pressure coefficient values of downstream cylinder.

#### 4.4.2 Noise Emission Results

The noise emitted from the surface of the cylinders was calculated at two points as shown in Fig. 4.11: at  $\theta = 135$  degrees on the upstream cylinder, and at  $\theta = 45$  degrees on the downstream cylinder. This was done using a series of pressure probes at that location along the span of the cylinders which recorded the unsteady pressure.



**Fig. 4.11: Location of pressure probes where pressure spectra were calculated.**

The power spectral density (PSD) values in Fig. 4.14 and Fig. 4.15 were calculated using 3 analysis blocks and a Hamming window function. It was found that the initial transient of the simulation took 0.15 seconds to wash out, so only data after this initialization were used for the pressure analysis. This can be seen at the beginning of the raw pressure time histories output from STAR CCM+ in Fig. 4.12 and Fig. 4.13.

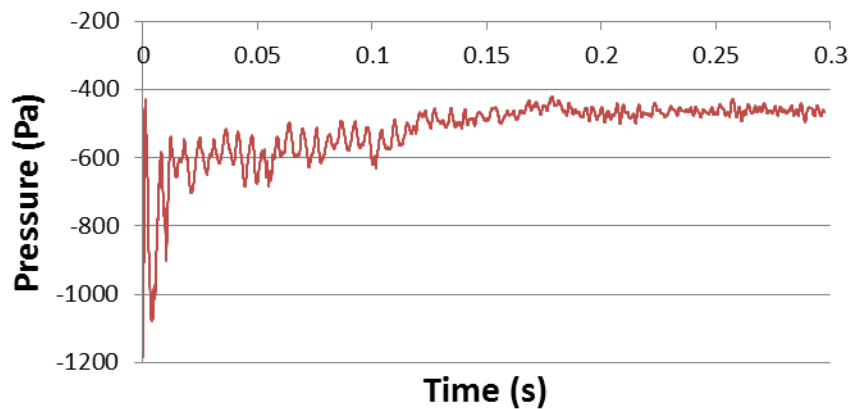


**Fig. 4.12: Gauge pressure-time history for the upstream cylinder.**

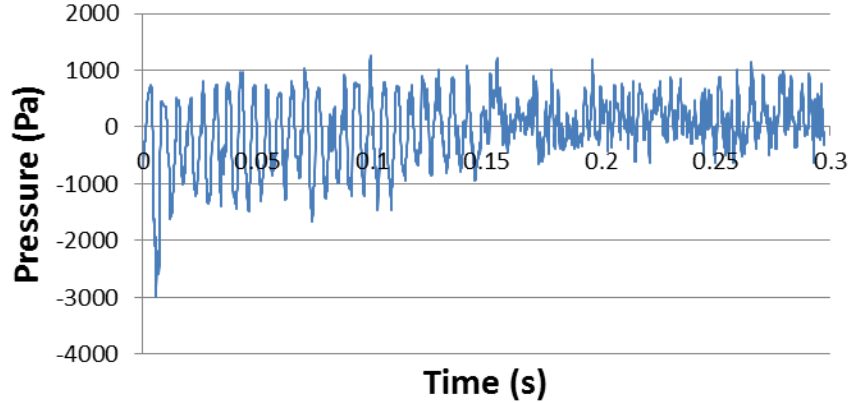


**Fig. 4.13: Gauge pressure-time history for the downstream cylinder.**

The shedding frequencies and magnitudes were well captured in both instances, as well as good simulation of noise levels up to 500 Hz and 1000 Hz for the upstream and downstream cylinders, respectively. The peak values and frequencies are listed in Table 4.7, which are about within 10 and 7 dB of the experiments for the upstream and downstream cylinder, respectively. It is expected that a finer grid in the wake region between the two cylinders, a longer simulation time, and a greater domain size in the span wise direction would improve these results.

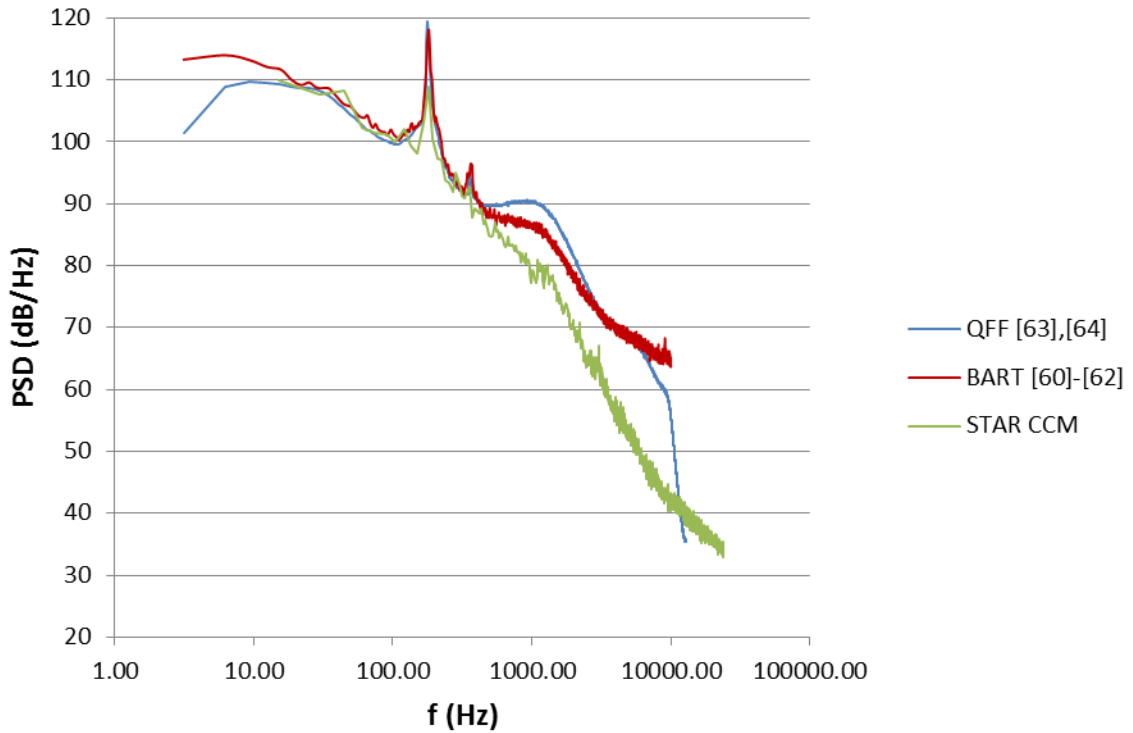


**Fig. 4.14:** Power spectral density values for pressure probe at  $\theta = 135^\circ$  on upstream cylinder.

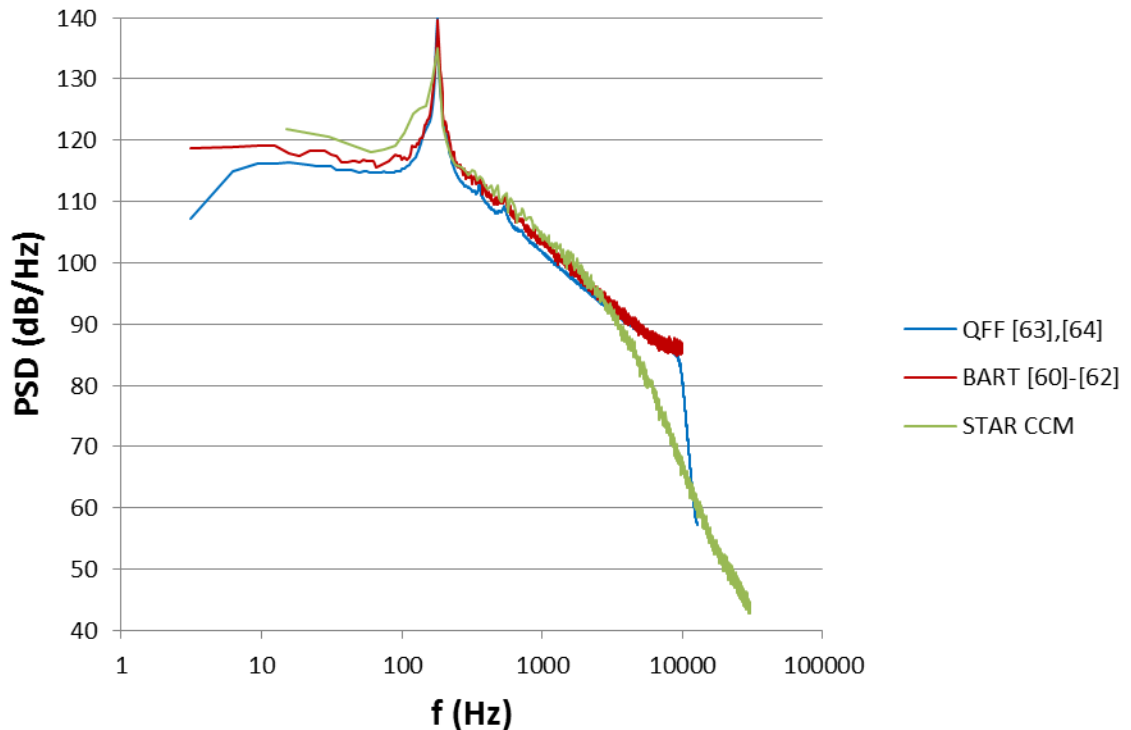


**Fig. 4.15:** Power spectral density values for pressure probe at  $\theta = 45^\circ$  on downstream cylinder.

**Table 4.7: Peak frequencies and magnitudes for tandem cylinder test case**

Transducer Location	Data	Peak Frequency (Hz)	Peak Magnitude (dB)
<b>Upstream Cylinder at <math>\theta = 135^\circ</math></b>	BART Experiment	181	118
	QFF Experiment	178	119
	STAR CCM+ Simulation	180	109
<b>Downstream Cylinder at <math>\theta = 45^\circ</math></b>	BART Experiment	181	140
	QFF Experiment	178	140
	STAR CCM+ Simulation	183	133

## 4.5 Chapter Summary

The presented results, which predict noise levels within 10 dB of the peak at the correct frequency, show quite good comparison between the experiment and CFD, increasing the confidence in the capability of STAR CCM+ to predict noise. Consequently, propeller test cases will now be simulated.

# **Chapter 5: Aeroacoustic Validation of SR-2 Propeller in Low Speed Condition**

This chapter presents a propeller aeroacoustic test case, where experimental data is compared to simulated data from both STAR CCM+ results and SmartRotor results to assess the capabilities of both softwares at predicting propeller noise. The experiment background and conditions is contained in Section 2.2.

## **5.1 STAR CCM+ Simulation Setup**

### **5.1.1 Boundary Conditions and Grid Design**

The computational domain chosen consists of a cylinder extending a distance of 10 diameters in the radial direction, 11 diameters upstream and 21.5 diameters downstream from the propeller (Fig. 5.1 - Fig. 5.3). The propeller geometry was constructed in PTC Creo with 21 blade elements according to the definition of the propeller in Fig. 2.4, with 4 blades, a diameter of 0.591 m, and a root pitch angle of 21 degrees. An area-ruled spinner was constructed according to the geometry of the SR-2 spinner from Steffko and Jeracki [49] with a shaft which extends all the way through the domain. A stationary region enclosed a rotating cylindrical region which encapsulating the propeller, resulting in two regions for this case. The rotating cylinder has a diameter of 0.8 m (135% of the propeller diameter), extending 0.2 m upstream and 0.4 m downstream of the propeller. This region can be seen in Fig. 5.1, with a detailed view shown in Fig. 5.4.

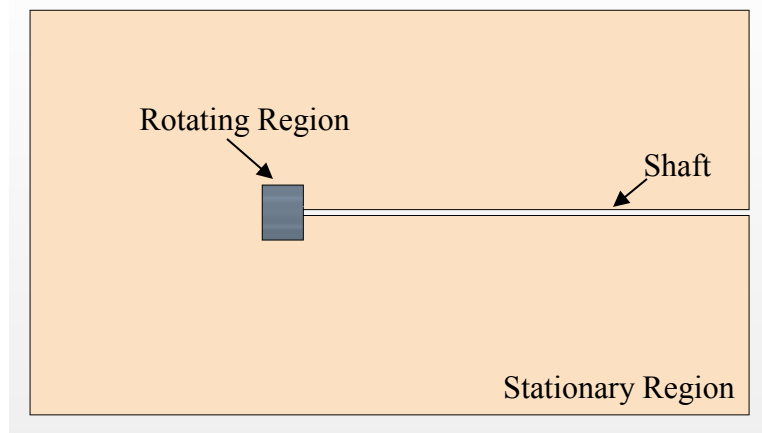


**Fig. 5.1:** Regions in computational domain for SR-2 Test Case 1.

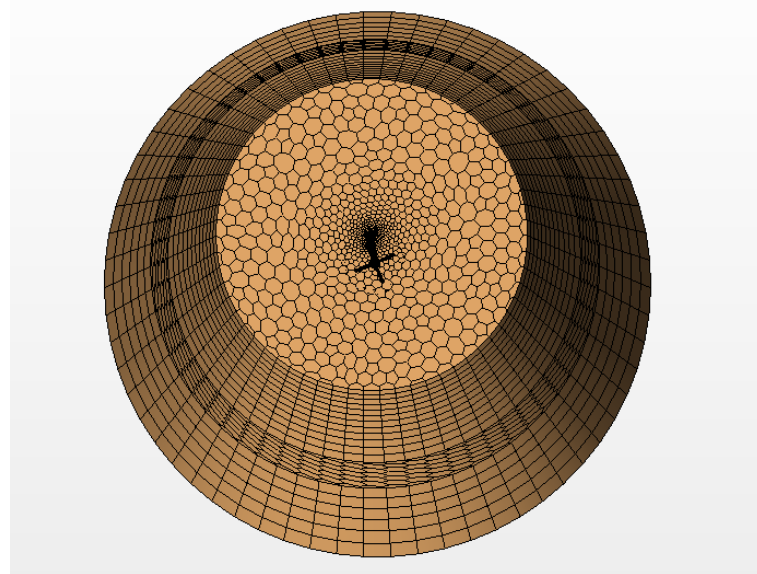


**Fig. 5.2:** Front view of the domain boundaries for SR-2 Test Case 1.

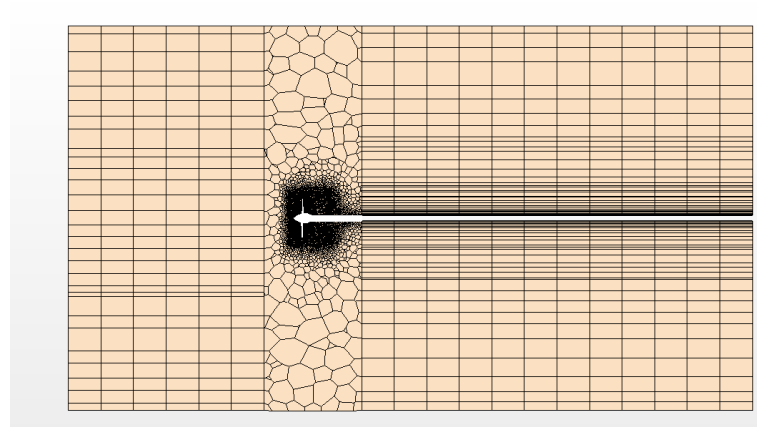


**Fig. 5.3:** Side view of grid for SR-2 Test Case 1.

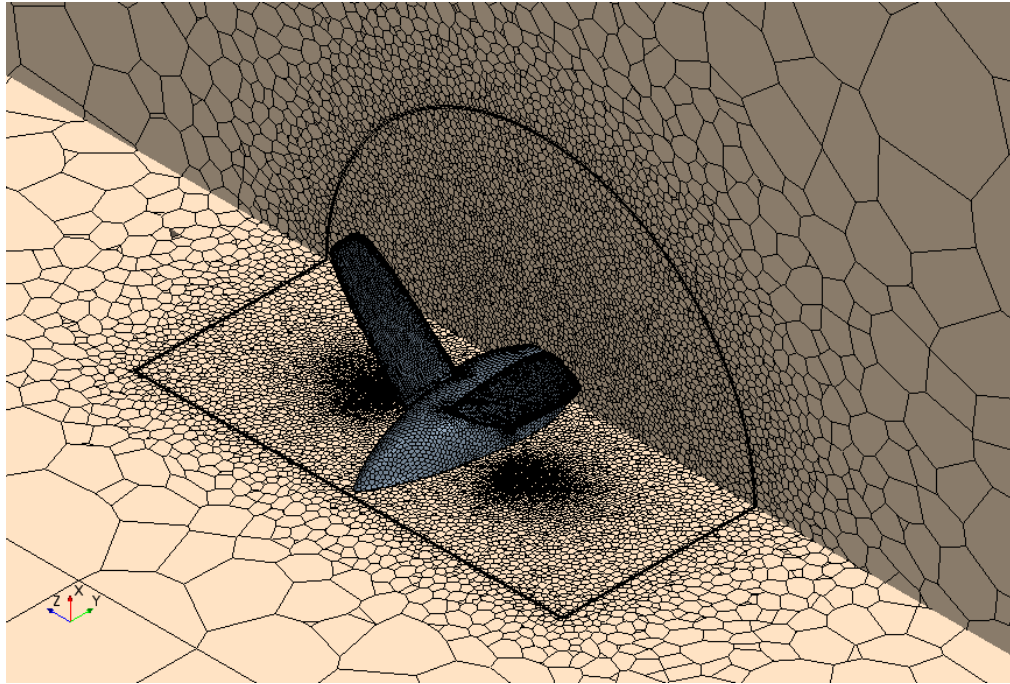


**Fig. 5.4: Grid around SR-2 propeller for Test Case 1.**

The boundary conditions are summarized in Table 5.1. A polyhedral grid (Fig. 5.2-Fig. 5.4) was constructed with general properties outlined in Table 5.2 and refinement properties according to Table 5.3. A grid was created for the domain, extending 1 diameter upstream and 1.5 diameters downstream of the propeller. This grid was then extruded normally upstream and downstream to fill out the entire domain, with properties listed in Table 5.4.

**Table 5.1: Boundary Conditions for SR-2 Test Case 1**

Boundary	Type	Values
<b>Radial Boundary</b>	Freestream	$M = 0.18$
<b>Domain Inlet and Outlet</b>	Freestream	$M = 0.18$
<b>Propeller, Spinner, and Shaft</b>	Wall (No-Slip)	Smooth Wall

**Table 5.2: General Grid Properties for SR-2 Test Case 1**

<b>Grid Property</b>	<b>Value</b>
<b>Number of Cells</b>	3,762,853
<b>Base Size</b>	$3.8 \times 10^{-3}$ m
<b>Prism Layer (Propeller and Spinner)</b>	
<b>Prism Layers</b>	15
<b>Prism Layer Stretch Function</b>	Geometric Progression
<b>Prism Layer Thickness</b>	$5 \times 10^{-4}$ m
<b>Thickness of Near Wall Prism Layer</b>	$1 \times 10^{-7}$ m
<b>Prism Layer (Stationary-Rotational Interface)</b>	
<b>Prism Layers</b>	1 (in both directions)
<b>Prism Layer Thickness</b>	$1.9 \times 10^{-3}$ m
<b>Prism Layer (Shaft)</b>	
<b>Prism Layers</b>	2
<b>Prism Layer Stretch Factor</b>	1.5
<b>Prism Layer Thickness</b>	$5 \times 10^{-4}$ m

**Table 5.3: Refinement Regions of Grid for SR-2 Test Case 1**

<b>Refinement Surface</b>	<b>Cell Size (m)</b>
<b>Outside of Stationary Domain</b>	$3.0 \times 10^{-1}$
<b>Outside of Rotating Domain</b>	$7.6 \times 10^{-3}$
<b>Shaft Surface</b>	$1.14 \times 10^{-2}$
<b>Spinner Surface</b>	$5.70 \times 10^{-3}$
<b>Blade Surface</b>	$2.85 \times 10^{-3}$
<b>Leading Edge</b>	$9.50 \times 10^{-4}$
<b>Trailing Edge</b>	$7.60 \times 10^{-4}$
<b>Tip of Propeller</b>	$9.50 \times 10^{-4}$

**Table 5.4: Grid Extrusion Parameters for SR-2 Test Case 1**

<b>Property</b>	<b>Value</b>
<b>Extrusion Method</b>	Constant Rate Normal
<b>Upstream Extrusion Length</b>	3 m
<b>Upstream Extrusion Layers</b>	6
<b>Downstream Extrusion Length</b>	6 m
<b>Downstream Extrusion Layers</b>	12

### 5.1.2 Solver Selection and Simulation Properties

All flight conditions were set according to the experimental conditions listed in Table 2.2.

To initialize the solution, the following steps were taken:

1. The solution was initialized with a constant velocity of 62 m/s (0.18 Mach). A grid sequencing method utilizing 10 levels and 50 iterations per level was then performed to initialize a steady state solution with a coupled flow solver using a CFL number of 5. This steady state solver was run for 3,000 iterations, at which point the moment and thrust values were converged in steady state. The expert solution driver was used with default properties.
2. The solution was run using a sliding mesh method (as described in Section 3.1.6) using the unsteady parameters listed in Table 5.5 and Table 5.6.

**Table 5.5: Solver Properties for SR-2 Test Case 1**

Solver Category	Method
<b>Time</b>	Implicit Unsteady
<b>Flow</b>	Coupled Flow
<b>Turbulence Model</b>	RANS Simulation SST Menter K-Omega
<b>Temporal Discretization</b>	2 <sup>nd</sup> Order
<b>Turbulence Under-Relaxation Factor</b>	0.5
<b>Acoustic Solver</b>	Ffowcs Williams-Hawkins

**Table 5.6: Simulation Properties for SR-2 Test Case 1**

Property	Value
<b>Simulation Length</b>	0.0375 s 3750 time steps 5.13 revolutions
<b>Time step</b>	$1 \times 10^{-5}$ s
<b>Inner Iterations per time step</b>	10
<b>CPUs Utilized</b>	40 (HPCVL)
<b>Wall clock time per time step</b>	121 s
<b>Total wall clock time</b>	126 hours

### **5.1.3 Convergence Criteria**

Initially, the thrust and torque are converged in steady state. Following this, after the initial transient had washed out, the convergence criteria used for the simulations was based on a single order of magnitude reduction in relative residuals at each time step based on a personal communication from a CD-adapco engineer [124]. The standard turbulence dissipation rate residual was the only value which did not decrease by an order of magnitude across each time step, but it was also found that even a significant variation of simulation parameters did not contribute to a higher reduction in this residual across a time step. A CFL number of 1 was used for the simulation based on recommendations for using the Ffowcs Williams-Hawkins solver from STAR CCM+ [104] and based on a study on the impact of CFL numbers on residual reduction and computational time.

### **5.1.4 Verification**

Three levels of grid density were considered for a grid dependence study. A coarse mesh of 1.7 million cells and a finer mesh of 9.6 million cells were created. Due to the extensive computational power required for the full unsteady simulations, only partial verification was performed for this simulation. This was accomplished by comparing the converged thrust and torque values for those steady state simulations which served as starting solutions for the unsteady simulations. As the unsteady values for thrust and torque compare within a percent of the steady state values, such verification studies in steady state give a good indication of what forces the grid will predict in unsteady simulations. Results of the verification are shown in Fig. 5.5. Additionally, steady simulations with a thicker and more refined boundary layer were performed, with results presented in Table 5.7.

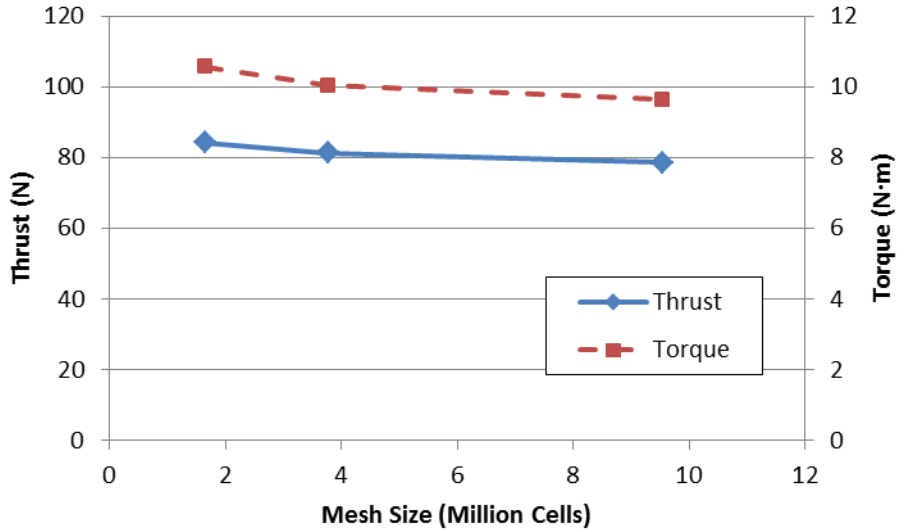


**Fig. 5.5: Convergence of thrust and torque values with grid size for steady state simulations.**

As one can see, there is less than a 5% change in both thrust and torque between the 3.5 and 8.6 million cell grid. Hence, the 3.5 million cell grid was utilized. Additionally, two tests were performed varying the near-wall prism layer mesh characteristics to ensure correct capturing of the propeller and spinner boundary layer, with all other meshing characteristic held the same.

**Table 5.7: Verification of Boundary Layer Thickness and Refinement**

Grid Size (Million Cells)	Boundary Layer Thickness	Number of Prism Layers	Thrust (N)	Torque (Nm)
3.8*	$5 \times 10^{-4}$ m*	15*	81.3*	10.0*
4.5	$5 \times 10^{-4}$ m	30	77.0	10.4
4.3	$1 \times 10^{-3}$ m	30	80.7	10.4

\*simulated parameters

Once again, the values compare to within 5% for both thrust and torque for the base case, which is simulated in this chapter. A proper verification study would perform an additional unsteady simulation to compare the acoustic results of a grid finer than 3.5 million cells, but because of time constraints and good comparison of numerical results to experiment as discussed in Section 5.3, such a simulation was not performed. In the grid

design, it was ensured that the size of the cells was capable of predicting at least 5 harmonics. The time step was chosen based on the desired maximum prediction frequency and the STAR CCM+ recommendation of at least 360 time steps per revolution for a sliding mesh simulation [104]. A value containing at least 720 time steps per revolution was chosen. No additional verification studies of time step were performed.

In the parametric study of blade count in Chapter 7, it was found that an analysis of four revolutions produced harmonic amplitudes within a dB of those produced by a simulation length of eight revolutions for all three cases. Thus, a simulation length of five revolutions was deemed sufficient for simulation, with the data from the first revolution not analyzed due to un converged values as the simulation switched from a steady state initialization to an unsteady simulation.

## 5.2 SmartRotor Simulation Setup

The SmartRotor simulation was set up with the blade defined according to Fig. 2.4, the flow conditions set to the experiment conditions in Table 2.2, and the simulation parameters listed in Table 5.8. As with classical panel methods, there is no need to define a computational domain here. It is only the surface of the object which is discretized into panels. The panels generated with SmartRotor for this propeller can be seen in Fig. 3.7. The specific geometrical input into the SmartRotor code is listed in Appendix A. Boots [55], [58] also performed this validation case in SmartRotor using the same simulation time step and the same number of chordwise and spanwise elements. However, as the geometrical description of the blade is not given, it is possible that there are slight

differences in blade geometries. A simulation was performed of this test case in order to obtain results at Transducer 7, which Boots did not simulate, for further comparison to STAR CCM+ data.

**Table 5.8: SmartRotor Simulation Properties for SR-2 Test Case 1**

Property	Value
<b>Simulation Length</b>	0.066 s 810 time steps 9 revolutions
<b>Time step</b>	$8.1325 \times 10^{-5}$ s
<b>Spanwise Elements</b>	16
<b>Chordwise Elements</b>	8
<b>CPUs Utilized</b>	6 (Desktop)
<b>Wall clock time per time step</b>	96 sec
<b>Total wall clock time</b>	2 hours

### 5.2.1 Convergence Criteria

No specific convergence criteria were used, though the aerodynamic properties in the code do converge quickly, as shown in Fig. 5.6. The analyzed data only contained values with converged aerodynamic data, which also corresponded to uniform acoustic pressure data.

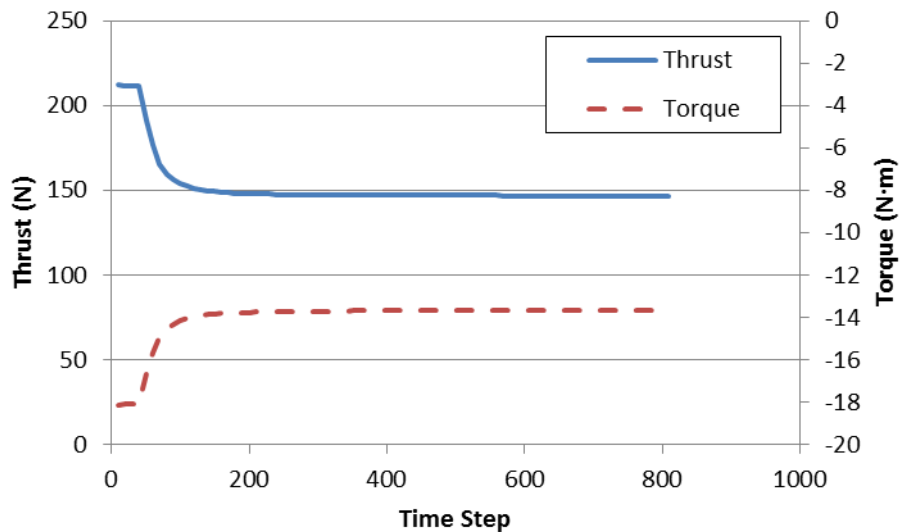


**Fig. 5.6: Thrust and torque convergence plotted against iteration in SmartRotor.**

### 5.2.2 Verification

Boots performed a verification of this validation study in [58] for spanwise elements, chordwise elements, timestep, and simulation length and their impact on OASPL, thrust, torque, and first harmonic. The final parameters chosen by Boots match the ones chosen in this chapter. To provide additional verification data, in this work three additional studies were performed with the SmartRotor code for the same simulation duration, utilizing more spanwise elements, chordwise elements, and a smaller time step. The key results are presented in Table 5.9, showing that the utilized time step and number of chordwise and spanwise are sufficient for the simulation.

**Table 5.9: SmartRotor Verification Results for SR-2 Test Case 1**

Time Step ( $10^{-5}$ s)	Spanwise Elements	Chordwise Elements	Thrust (N)	Torque (N·m)	Harmonic Amplitudes [dB] at Transducer 12		
					First	Third	Fifth
8.1325*	16*	8*	146.8*	13.7*	94.6*	80.8*	70.1*
8.1325	24	8	145.0	13.6	94.5	80.5	69.8
4.06625	16	8	148.6	13.8	94.8	81.0	70.4
8.1325	16	16	151.8	14.1	95.1	80.8	69.9

\*simulated parameters

## 5.3 Results Validation

In this section, aerodynamic and aeroacoustic results from both STAR CCM+ and SmartRotor will be compared to experimental data.

### 5.3.1 Aerodynamic Results

The following values were computed for the thrust, torque,  $C_T$ , and  $C_P$ :

**Table 5.10: Aerodynamic Results for SR-2 Test Case 1**

Data	Thrust (N)	Torque (N·m)	$C_T$	$C_P$
Experimental Data (Estimated) [12]	N/A	N/A	0.08	0.09
STAR CCM+	81.3	10.04	0.03	0.04
SmartRotor	146.8	13.67	0.05	0.05

The variation is quite significant, in part because of the difficulty of predicting a high RPM, low thrust case where the propeller blades are nearly in a windmill state where they are not generating very much thrust. However, because the thrust and power coefficients are relatively small, the thrust and torque variations do not translate into large discrepancy in acoustic predictions. A simple blade element theory calculation, based on the QOPTR code from Jonathan Wiebe [125] yielded thrust results of 61.4 N, more in line with the STAR CCM+ results than any others. This discrepancy will be discussed further in Chapter 8 in the context of the other results.

### 5.3.2 Aeroacoustic Results

Soderman and Horne [12] provide sound pressure level plots of the acoustic spectra for two transducers, number 7 and number 12, along with measurements of ambient wind tunnel spectra for the wind tunnel for transducer 7, shown in Fig. 5.7 below.

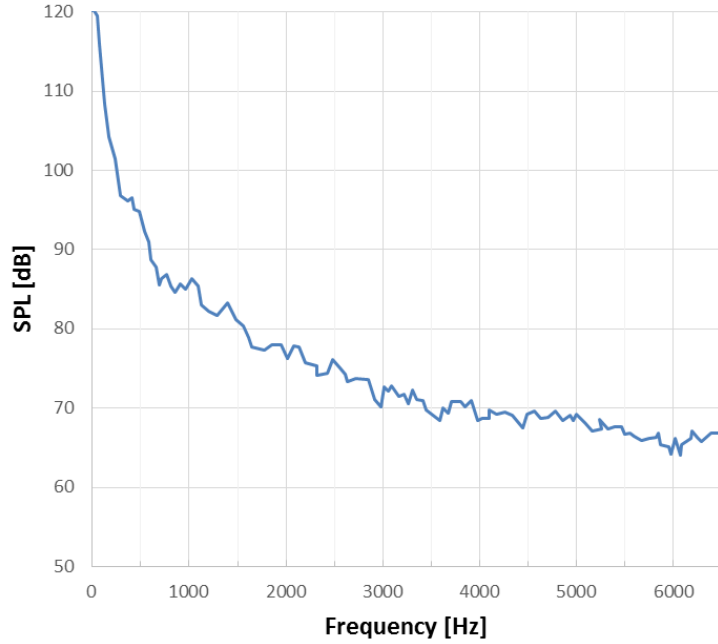


**Fig. 5.7:** Wind tunnel data measured at transducer 7 (from [12]).

The key results to predict are the magnitudes of the Blade Passage Frequencies (BPFs), which define peak noise values for propellers. In STAR CCM+, there are two methods for the unsteady prediction of noise via the Ffowcs Williams-Hawkins method, as described in Section 3.1.4.2. In this simulation, both impermeable and permeable surfaces were utilized separately. The impermeable surface was selected as the blade and spinner surfaces, and the permeable surface was chosen to be the rotating domain.

**Table 5.11: Blade Passage Frequency Noise Predictions for SR-2 Test Case 1**

BPF	Frequency (Hz)	Experimental Data (dB)	STAR CCM+ (dB)		SmartRotor (dB)
			Impermeable FW-H Surface	Permeable FW-H Surface	
<b>Transducer 7</b>					
1	547	101	120.6	105.6*	104
2	1093	94	118.5	97.5*	95
3	1640	88	113.9	95.8*	87
4	2187	81	108.2	95.0*	79
5	2733	76	101.6	83.3*	72
<b>Transducer 12</b>					
1	547	101	111.6	99.7*	95
2	1093	96	110.3	92.5*	87
3	1640	91	106.5	91.3*	81
4	2187	83	101.5	92.1*	75
5	2733	77	95.5	87.3*	70

\*Though these magnitudes are correct, they do not emerge in clear harmonic fashion and do not describe the only peaks in the system.

It should be noted that transducer 7 is located only 2.4 diameters away from the propeller, as opposed to transducer 12 which is located 7.3 diameters from the propeller. As transducer 7 is located in the near field, it is not expected that the Ffowcs Williams-Hawkins equations, which are based on far field noise, will give as good comparison as for transducer 12. Moreover, Soderman and Horne[12] discuss skepticism over the reliability of transducer 7. The remainder of the discussion will focus on transducer 12.

The STAR CCM+ impermeable results overpredict the noise by 10 dB at the first harmonic with increasing overprediction up to 19 dB at the fifth harmonic. The permeable results under predict reasonable magnitudes around the peaks, but do not produce a spectra representative of a propeller, as seen in Fig. 5.12 and Fig. 5.15. SmartRotor predicts noise within 10 dB, not increasing with harmonic but rather predicting between 6 and 10 dB below experimental values. It should be noted that the ambient noise in the wind tunnel would contribute to some of the difference between experimental and numerical results in SmartRotor, alongside contribution of quadrupole noise, which, likely, is minimal in accordance with Section 3.1.4.2. The SmartRotor data matches that obtained by Boots [55], [58] for transducer 12.

Pressure time history for one revolution at transducer 12 outputted from STAR CCM+ and SmartRotor, before post-processing, is shown in Fig. 5.8 - Fig. 5.10. Power spectral density plots for both STAR CCM+ and SmartRotor are shown in Fig. 5.11- Fig. 5.16: Noise at transducer 12 predicted in SmartRotor. All experimental data is taken from Soderman and Horne [12]. While the peaks of each blade passage frequency are predicted quite well, the magnitude of noise elsewhere is quite low, which is to be expected for a simulation only considering the impact of a propeller without any ambient aeroacoustic interference. This can be seen in Fig. 1.3 (also from the experimental results of this test case) which shows the difference in propeller noise when the wind tunnel is not operating and when it is operating at 62 m/s.

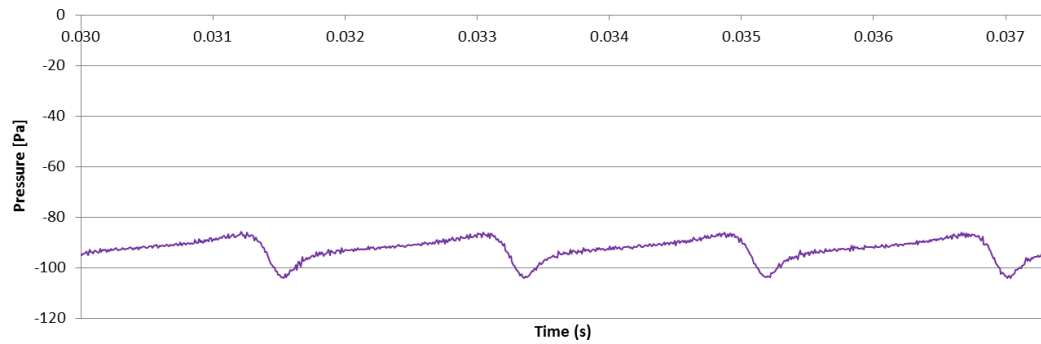


**Fig. 5.8:** Gauge pressure time history at transducer 12 predicted by an impermeable FW-H surface in STAR CCM+. Time period of revolution: 0.0073 s.

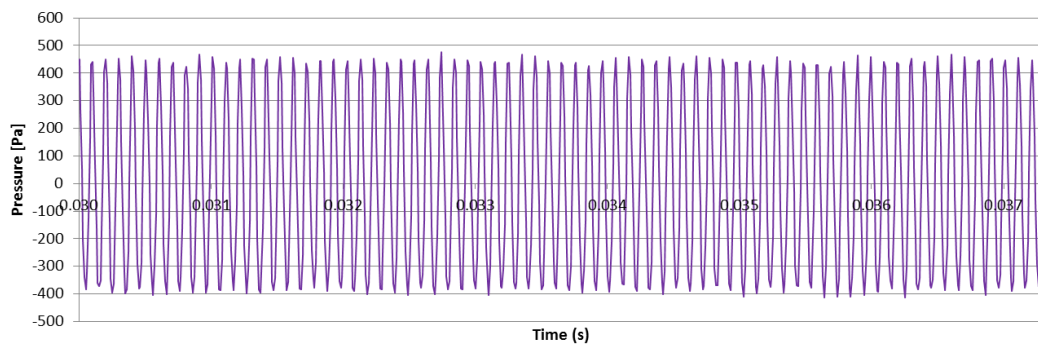


**Fig. 5.9:** Gauge pressure time history at transducer 12 predicted by a permeable FW-H surface in STAR CCM+. Time period of revolution: 0.0073 s.

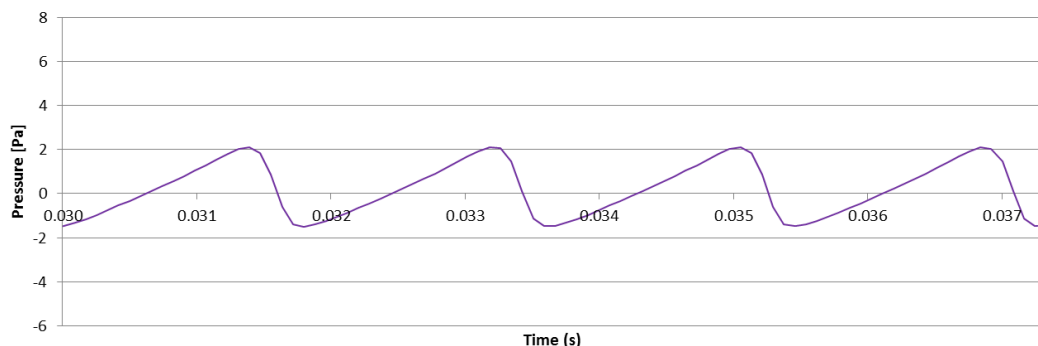


**Fig. 5.10:** Gauge pressure time history at transducer 12 predicted by SmartRotor. Time period of revolution: 0.0073 s.

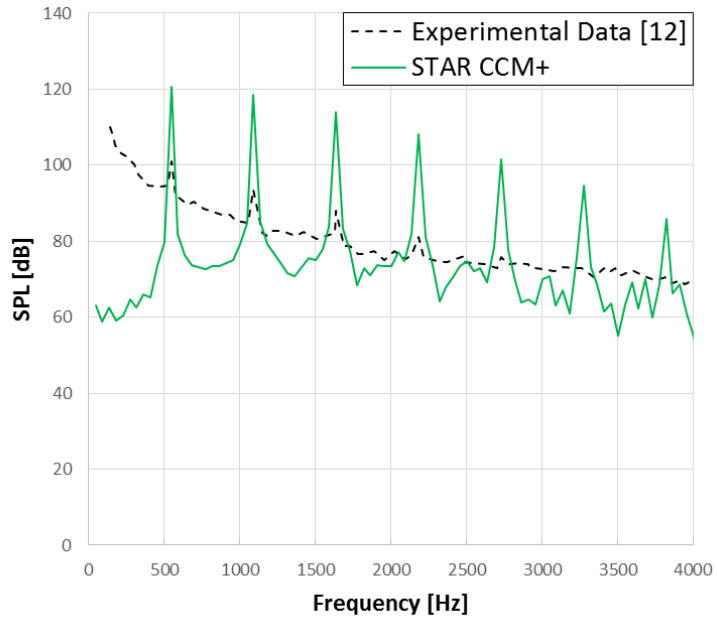


**Fig. 5.11:** Noise at transducer 7 predicted in STAR CCM+ from an impermeable FW-H surface.

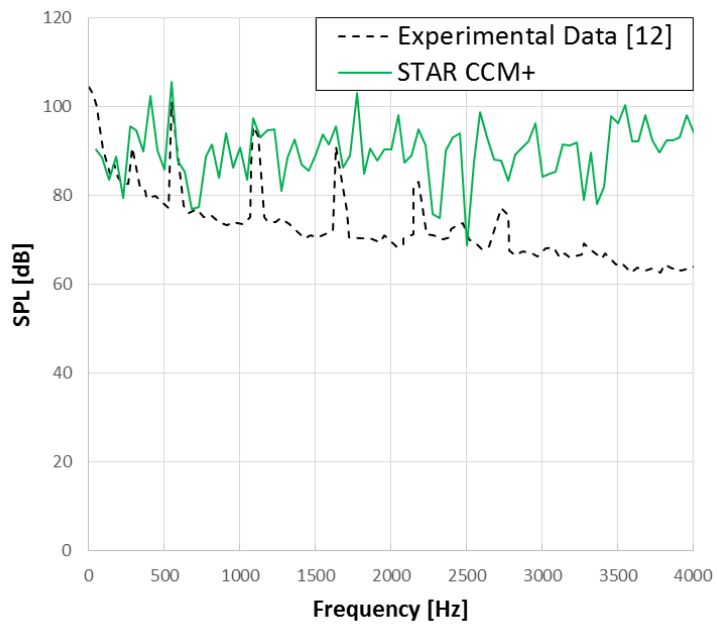


**Fig. 5.12:** Noise at transducer 7 predicted in STAR CCM+ from a permeable FW-H surface.

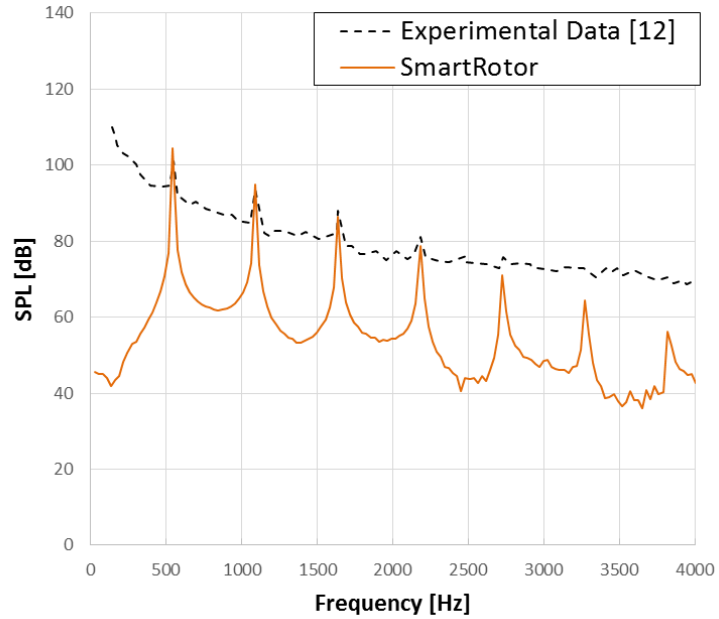


**Fig. 5.13:** Noise at transducer 7 predicted in SmartRotor.

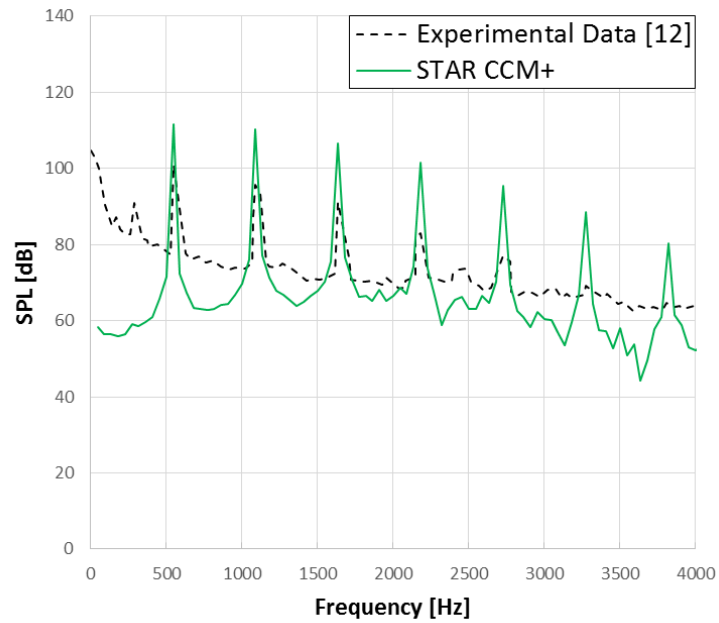


**Fig. 5.14:** Noise at transducer 12 predicted in STAR CCM+ from an impermeable FW-H surface.

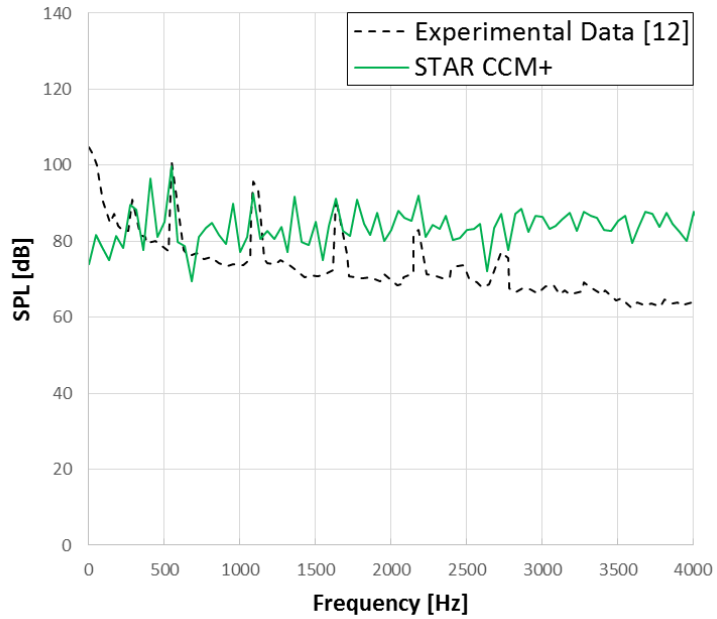


**Fig. 5.15:** Noise at transducer 12 predicted in STAR CCM+ from a permeable FW-H surface.

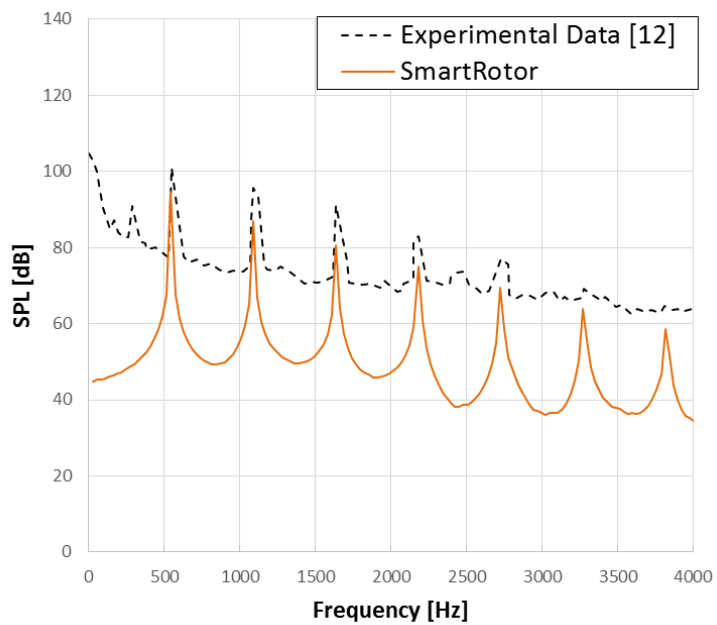


**Fig. 5.16:** Noise at transducer 12 predicted in SmartRotor.

## 5.4 Chapter Summary

Both STAR CCM+ with impermeable surfaces and SmartRotor predict harmonic results within 10 dB for the first blade passage harmonics, while the permeable surface chosen did not produce reasonable results. STAR CCM+ contains a worse prediction, overpredicting the first harmonic by 10 dB and the fifth harmonic by 18 dB. SmartRotor, on the other hand, under predicts noise at the first harmonic by 6 dB and the first five harmonics by less than 10 dB. These results will be discussed further in Chapter 8. Because the aerodynamic data did not match well to the estimates for the experiments, as well as for further validation, another validation case including aerodynamic data will be run.

# **Chapter 6: Aerodynamic and Aeroacoustic Validation of SR-2**

## **Propeller in Cruise Conditions**

This chapter presents a test case typical for a propeller in cruise. Experimental data was compared to simulation results from both STAR CCM+ and SmartRotor. Once again, the purpose of the comparisons was to assess the effectiveness of both CFD softwares at predicting propeller noise. This test case was performed in addition to the previous validation case in Chapter 5 for the following reasons:

1. To ensure correct aerodynamic prediction of an aeroacoustic test case to a measured value, rather than an estimated value from the test case performed by Soderman and Horne.
2. This case presents values typical of a turboprop at cruise conditions because of a flight speed of 0.6 Mach, providing a good base case for a study on the impact of blade count on propeller noise in Chapter 7.

The background to this experiment, along with experimental data, is described in Section 2.3.

### **6.1 STAR CCM+ Simulation Setup**

#### **6.1.1 Boundary Conditions and Grid Generation**

The structure of the grid and the simulations follow the exact same pattern as that utilized for the previous SR-2 simulation described in Section 5.1.1. The computational domain chosen consisted of a cylinder extending a distance of 10 diameters in the radial direction, 11 diameters upstream and 21.5 diameters downstream from the propeller (similar to Fig. 5.1). The propeller geometry was constructed in PTC Creo with 21 blade

elements according to the definition of the propeller in Fig. 2.4, with 8 blades, a diameter of 0.622 m, and a root pitch angle of 60.5 degrees. An area-ruled spinner was constructed according to the geometry of the SR-2 spinner from Stefko and Jeracki [49] with a shaft which extends all the way through the domain. Note that the pitch angle was selected to match the experimental  $C_P$  values based on steady state simulations, as discussed further in Section 6.2.1. A stationary region enclosed a rotating cylindrical region encapsulating the propeller, resulting in two regions for this case. The rotating region has a diameter of 0.84 m (135% of the propeller diameter), extending 0.21 m upstream and 0.42 m downstream of the propeller.

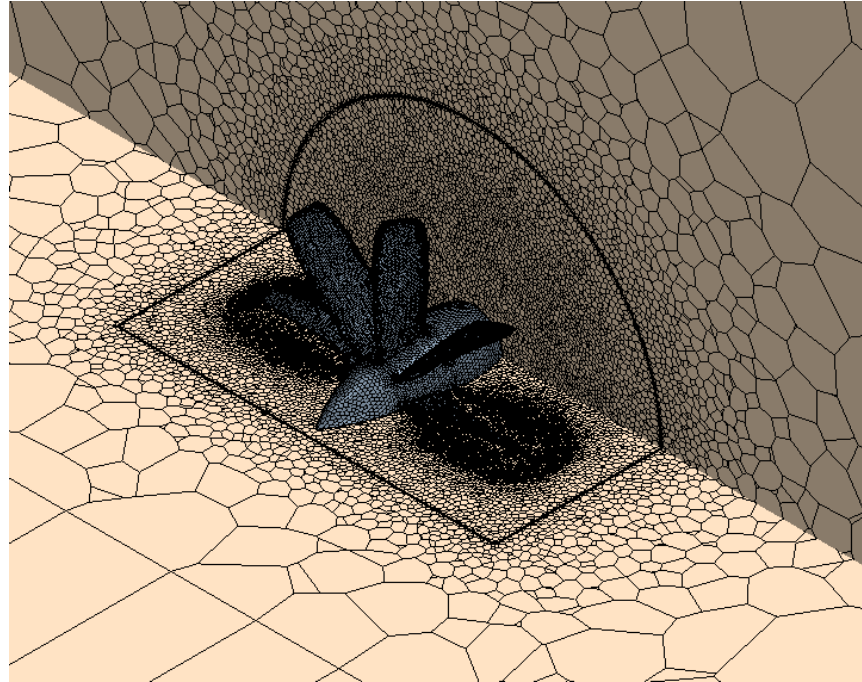


**Fig. 6.1: Grid around SR-2 Propeller for Test Case 2.**

The boundary conditions are summarized in Table 6.1. A polyhedral grid (Fig. 6.1) was constructed with general properties outlined in Table 6.2 and refinement properties outlined in Table 6.3. A grid was created for the domain extending 1 diameter upstream

and 1.5 diameters downstream of the propeller. This grid was then extruded normally upstream and downstream to fill out the entire domain, with properties listed in Table 6.4.

**Table 6.1: Boundary Conditions for SR-2 Test Case 2**

Boundary	Type	Values
<b>Radial Boundary</b>	Freestream	$M = 0.6$
<b>Domain Inlet and Outlet</b>	Freestream	$M = 0.6$
<b>Propeller, Spinner, and Shaft</b>	Wall (No-Slip)	Smooth Wall

**Table 6.2: General Grid Properties for SR-2 Test Case 2**

Grid Property	Value
<b>Number of Cells</b>	6,196,207
<b>Base Size</b>	$4 \times 10^{-3} \text{ m}$
<b>Prism Layer (Propeller and Spinner)</b>	
<b>Prism Layers</b>	15
<b>Prism Layer Stretch Function</b>	Geometric Progression
<b>Prism Layer Thickness</b>	$5 \times 10^{-4} \text{ m}$
<b>Thickness of Near Wall Prism Layer</b>	$1 \times 10^{-7} \text{ m}$
<b>Prism Layer (Stationary-Rotational Interface)</b>	
<b>Prism Layers</b>	1 (in both directions)
<b>Prism Layer Thickness</b>	$1.9 \times 10^{-3} \text{ m}$
<b>Prism Layer (Shaft)</b>	
<b>Prism Layers</b>	2
<b>Prism Layer Stretch Factor</b>	1.5
<b>Prism Layer Thickness</b>	$5 \times 10^{-4} \text{ m}$

**Table 6.3: Refinement Regions of Grid for SR-2 Test Case 2**

Refinement Surface	Cell Size (m)
<b>Outside of Stationary Domain</b>	$3.16 \times 10^{-1}$
<b>Outside of Rotating Domain</b>	$8.00 \times 10^{-3}$
<b>Shaft Surface</b>	$1.20 \times 10^{-2}$
<b>Spinner Surface</b>	$6.00 \times 10^{-3}$
<b>Blade Surface</b>	$3.00 \times 10^{-3}$
<b>Leading Edge</b>	$1.00 \times 10^{-3}$
<b>Trailing Edge</b>	$8.00 \times 10^{-4}$
<b>Tip of Propeller</b>	$1.00 \times 10^{-3}$

**Table 6.4: Grid Extrusion Parameters for SR-2 Test Case 2**

Property	Value
<b>Extrusion Method</b>	Constant Rate Normal
<b>Upstream Extrusion Length</b>	3.16 m
<b>Upstream Extrusion Layers</b>	6
<b>Downstream Extrusion Length</b>	6.31 m
<b>Downstream Extrusion Layers</b>	12

### 6.1.2 Selection of Blade Pitch Angles

Initially, it was desired to select a pitch angle to match  $C_P$  values from the experiment so that the predicted noise corresponds to the same forces on the blade. Steady state simulations were used to determine the pitch angle required to match experimental thrust. In this case, the blades had to be pitched to 60.5 degrees compared to the 59 degrees measured in the experiment. A summary of these results is provided in Table 6.5.

**Table 6.5: Comparison of Predicted Thrust and Torque for Periodic and Full Size Simulations**

Pitch Angle	Thrust (N)	Torque (N·m)	$C_T$	$C_P$
59	492.0	213.8	0.23	1.01
60	598.2	265.2	0.28	1.25
60.5	649.4	291.4	0.30	1.37
61	696.4	317.3	0.32	1.50

Note: the target value from experiment was  $C_P = 1.34$  [15].

### 6.1.3 Solver Selection and Simulation Properties

All flight conditions were set according to the experimental conditions listed in Table 2.3, except for the blade pitch angle, which was set to 61.5 degrees in accordance with Section 6.1.2. To initialize the solution, the following steps were taken:

1. The solution was initialized with a constant velocity of 206 m/s (0.6 Mach). A grid sequencing method utilizing 10 levels and 50 iterations per level was performed to initialize a steady state solution with a coupled flow solver using a CFL number of 5. This steady state solver was run for 3000 iterations, at which

point the moment and thrust values have converged in steady state. The expert solution driver was used with default properties.

2. The simulation was run using a sliding mesh method (as described in Section 3.1.6) using the parameters listed in Table 6.6 and Table 6.7.

**Table 6.6: Solver Properties for SR-2 Test Case 2**

Solver Category	Method
<b>Time</b>	Implicit Unsteady
<b>Flow</b>	Coupled Flow
<b>Turbulence Model</b>	RANS Simulation SST Menter K-Omega
<b>Temporal Discretization</b>	2 <sup>nd</sup> Order
<b>Turbulence Under-Relaxation Factor</b>	0.5
<b>Acoustic Solver</b>	Ffowcs Williams-Hawkins

**Table 6.7: Simulation Properties for SR-2 Test Case 2**

Property	Value
<b>Simulation Length</b>	0.0480 s 3737 time steps 5.2 revolutions
<b>Time step</b>	$1.28462 \times 10^{-5}$ s
<b>Inner Iterations per time step</b>	10
<b>CPUs Utilized</b>	40 (HPCVL)
<b>Wall clock time per time step</b>	186 sec
<b>Total wall clock time</b>	193 hours

#### 6.1.4 Convergence Criteria

The convergence criteria are similar to those described in Section 5.1.3, with a single order of magnitude reduction in relative residuals at each time step. Once again, the standard turbulence dissipation rate residual was the only value which did not decrease by an order of magnitude across each time step, but it was also found that even a significant variation of simulation parameters did not improve this. A CFL number of 1 was once again used.

### 6.1.5 Verification

Due to the extensive computational power required for the full unsteady simulations, only partial verification was performed for this simulation in a very similar process as in Section 5.1.4. Before performing unsteady simulations, converged thrust and torque values were compared for steady state simulations in Fig. 6.2 using meshes of 2.6, 6.2, and 10 million cells.

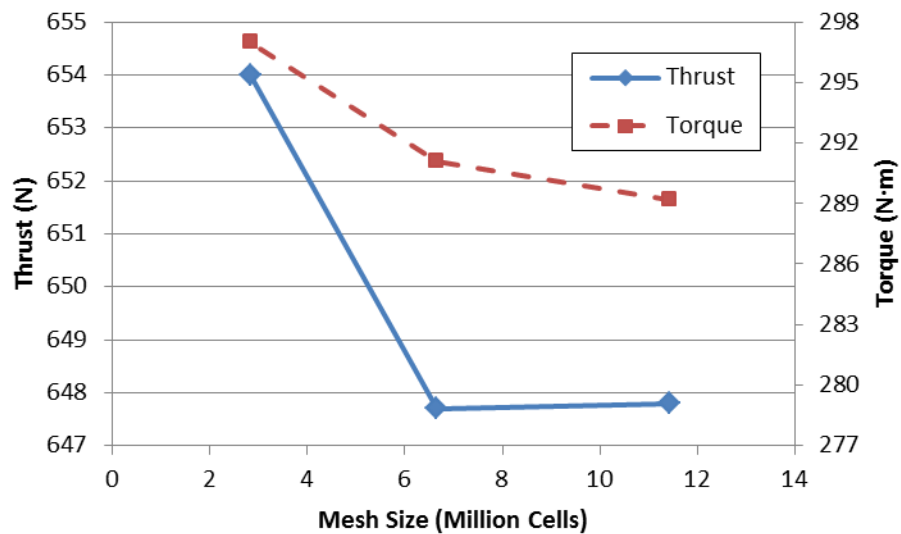


**Fig. 6.2: Convergence of thrust and torque values with grid size for steady state simulations.**

There is less than a 2% change in both thrust and torque between the 6.2 and 10 million cell grid. Hence, the 6.2 million cell grid is utilized. The unsteady values for thrust and torque compare very well with the steady state simulations once again. Additionally, two tests were performed varying the near-wall prism layer mesh characteristics to ensure correct capturing of the propeller and spinner boundary layer, with all other meshing characteristic held the same.

**Table 6.8: Verification of Boundary Layer Thickness and Refinement**

Grid Size (Million Cells)	Boundary Layer Thickness	Number of Prism Layers	Thrust (N)	Torque (Nm)
6.2*	$5 \times 10^{-4}$ m*	15*	649.4*	291.4*
7.9	$5 \times 10^{-4}$ m	30	654.7	293.7
7.6	$1 \times 10^{-3}$ m	30	659.2	295.0

\*simulated parameters

The values compare to within 2% for both thrust and torque for the base case, which is simulated in this chapter. Once again, a proper verification study would perform an additional unsteady simulation to compare the acoustic results of a grid finer than 6.2 million cells, but because of time constraints and good comparison of numerical results to experiment as discussed in Section 6.3, such a simulation was not performed.

For the same reasons discussed in Section 5.1.4, the simulation length was chosen to be five revolutions and the time step was chosen once again with 720 time steps per revolution was chosen. No additional verification studies of time step were performed. In the grid design, it was ensured that the size of the cells was capable of predicting at least 5 harmonics.

## 6.2 SmartRotor Simulation Setup

The SmartRotor simulation was set up with the blade defined according to Fig. 2.4 and a pitch angle of 60.5 degrees. Rather than adjusting pitch to match thrust or torque data, the same pitch angle used for the STAR CCM+ simulations were used for the SmartRotor simulations. The flow conditions were set to the experimental conditions in Table 2.3 and the following simulation parameters listed in Table 6.9.

**Table 6.9: SmartRotor Simulation Properties for SR-2 Test Case 2**

Property	Value
<b>Simulation Length</b>	0.08324 s 900 time steps 5 revolutions
<b>Time step</b>	$5.1385 \times 10^{-5}$ s
<b>Spanwise Elements</b>	16
<b>Chordwise Elements</b>	8
<b>CPUs Utilized</b>	6 (Desktop)
<b>Wall clock time per time step</b>	182 sec
<b>Total wall clock time</b>	13 hours

### 6.2.1 Convergence Criteria

As described in Section 5.2.1 no specific convergence criteria were used, though the aerodynamic properties in the code do converge quickly, similar to that shown for the previous test case in Fig. 5.6. The analyzed data only contained values with converged aerodynamic data, which also corresponded to uniform acoustic pressure data.

### 6.2.2 Verification

Three simulations were performed with the SmartRotor code for the same simulation duration, one utilizing more blade elements and another utilizing half the time step. The results are presented in Table 6.10:

**Table 6.10: SmartRotor Verification Results for SR-2 Test Case 1**

Time Step ( $10^{-5}$ s)	Spanwise Elements	Chordwise Elements	Thrust (N)	Torque (N·m)	Harmonic Amplitudes [dB] at Transducer 6	
					First	Second
5.1385*	16*	8*	805.6*	294.7*	121.4*	99.1*
5.1385	24	8	796.0	291.8	122.1	100.0
2.56925	16	8	845.6	308.1	123.0	101.4
5.1385	16	16	812.8	298.4	122.3	100.2

\*simulated parameters

The predictions are quite close between the four simulations, with the largest difference coming with the reduction of time step, which is still within 5% of thrust and torque values of the base case which is selected for simulation. However, this does not bear a large impact on the acoustic results.

### 6.3 Validation of CFD Results

Once again, in this chapter the CFD simulation results from STAR CCM+ and SmartRotor are compared to the experiment.

#### 6.3.1 Aerodynamic Results

Table 6.11 list the values were computed for the thrust, torque,  $C_p$ , and  $C_t$ :

**Table 6.11: Aerodynamic Results for SR-2 Test Case 2**

Data	Thrust (N)	Torque (N·m)	$C_t$	$C_p$
<b>Experimental Data [15]</b>	N/A	N/A	N/A	1.32
<b>STAR CCM+</b>	649.4	291.4	0.30	1.37
<b>SmartRotor</b>	805.6	294.7	0.38	1.39

The SmartRotor thrust results, once more, are quite high relative to STAR CCM+ as with the previous test case. However, the torque values are a near perfect match. This will be discussed further in Chapter 8.

#### 6.3.2 Aeroacoustic Results

Dittmar [15] provides peak frequencies of the acoustic spectra for all of the BPFs which were visible, only going up to the second BPF at most. Data is recorded for transducers 2-12. A comparison of the peak frequencies is listed in Table 6.12. It is clear from these results and from the previous chapter that the permeable Ffowcs Williams-Hawkins

(FW-H) surfaces do not yield good results, as can be seen from Fig. 6.4, Fig. 6.7, and Fig. 6.10. Power Spectral Density plots of transducers 2, 6, and 12 which are upstream, in line, and downstream of the propeller plane, respectively, are presented in Fig. 6.3-Fig. 6.11 for both SmartRotor and STAR CCM+ simulations. All experimental data is from Dittmar [15]. The remaining results are presented in Appendix B.

The impermeable results from STAR CCM+ under predicted noise by 4 to 11 dB at all microphones for the first harmonic, and under predicts noise by 9 to 32 dB at the second harmonic. The SmartRotor results were less consistent, predicting the first harmonic within 3 to 37 dB and the second harmonic by 29 to 51 dB. The SmartRotor predictions were more dependent upon microphone orientation, predicting noise better in front of the propeller than behind, indicating that the directional characteristics of the SmartRotor predictions are different than that of STAR CCM+ and less consistent with experiment. This is shown in Fig. 6.12.

**Table 6.12: Blade Passage Frequency Noise Predictions for SR-2 Test Case 2**

<b>BPF</b>	<b>Frequency (Hz)</b>	<b>Experimental Data (dB)</b>	<b>STAR CCM+ (dB)</b>		<b>SmartRotor (dB)</b>
			<b>Permeable FW-H Surface</b>	<b>Impermeable FW-H Surface</b>	
<b>Transducer 2</b>					
<b>1</b>	865	131.5	*	124.7	128.6
<b>Transducer 3</b>					
<b>1</b>	865	136.5	*	130.0	128.9
<b>Transducer 4</b>					
<b>1</b>	865	140.5	119.7	135.1	126.6
<b>2</b>	1730	137.5	*	114.7	105.2
<b>Transducer 5</b>					
<b>1</b>	865	144.0	119.9	136.4	124.4
<b>2</b>	1730	132.0	*	117.2	103.4
<b>Transducer 6</b>					
<b>1</b>	865	145.0	119.6	136.5	121.4
<b>2</b>	1730	134.0	*	117.4	99.1
<b>Transducer 7</b>					
<b>1</b>	865	143.5	*	136.1	117.1
<b>2</b>	1730	129.5	*	116.9	92.2
<b>Transducer 8</b>					
<b>1</b>	865	142.0	*	135.4	115.3
<b>2</b>	1730	125.0	*	115.7	89.2
<b>Transducer 9</b>					
<b>1</b>	865	139.5	*	133.9	112.4
<b>2</b>	1730	122.0	*	113.1	86.4
<b>Transducer 10</b>					
<b>1</b>	865	136.0	*	131.4	108.3
<b>2</b>	1730	124.5	*	108.8	78.2
<b>Transducer 11</b>					
<b>1</b>	865	133.5	*	129.9	106.1
<b>2</b>	1730	125.0	*	106.1	73.8
<b>Transducer 12</b>					
<b>1</b>	865	134.0	*	123.5	97.4
<b>2</b>	1730	127.5	*	95.4	*

\*Peak not visible above background noise

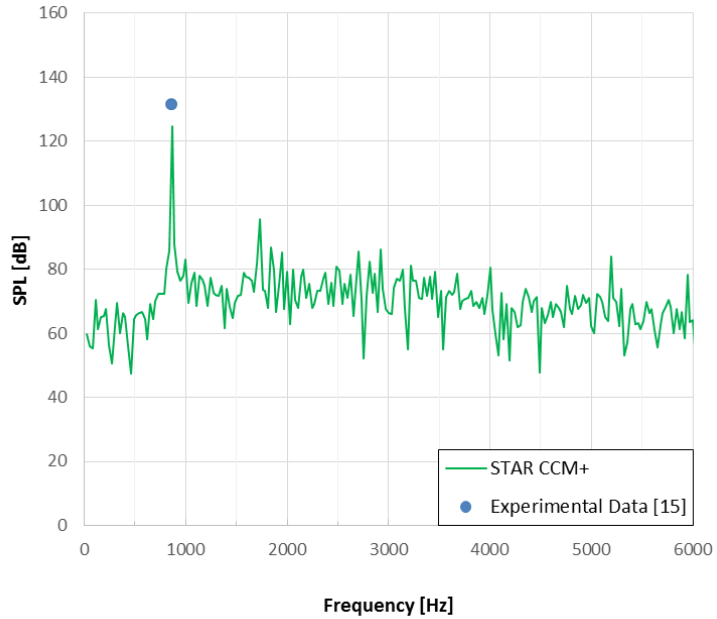


**Fig. 6.3: Noise at transducer 2 predicted in STAR CCM+ from an impermeable FW-H surface.**

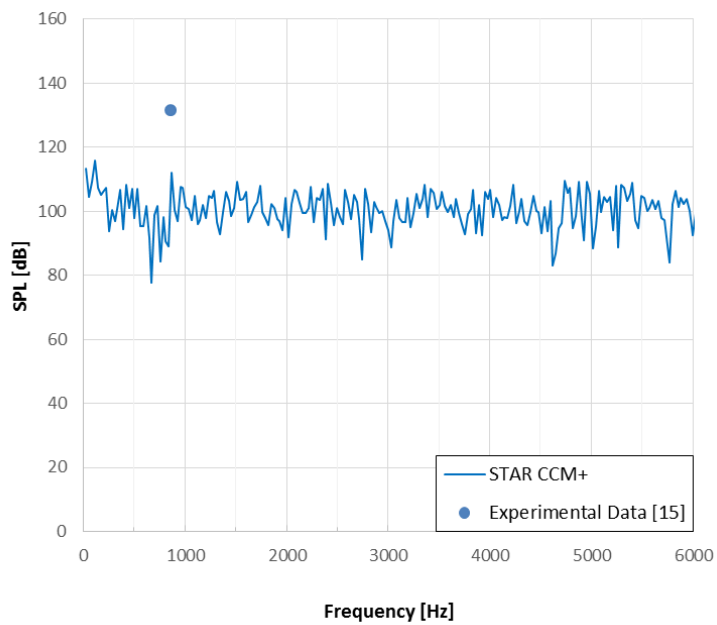


**Fig. 6.4: Noise at transducer 2 predicted in STAR CCM+ from a permeable FW-H surface.**

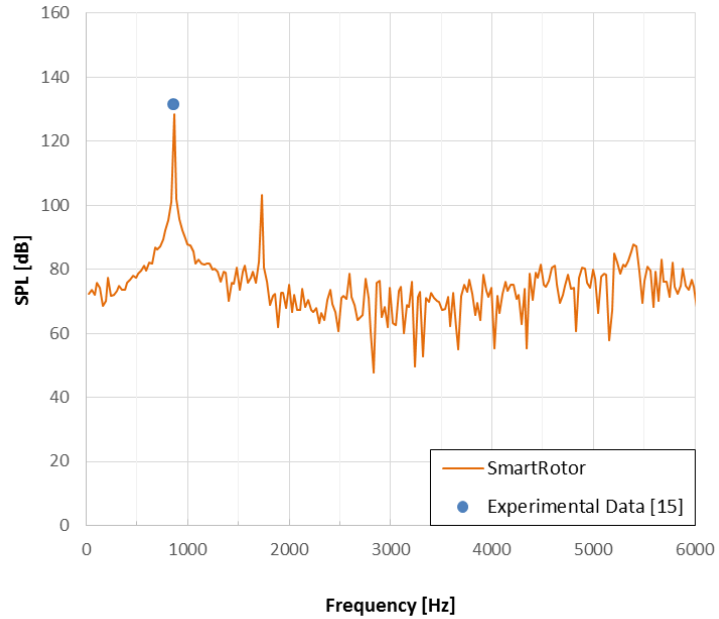


**Fig. 6.5: Noise at transducer 2 predicted in SmartRotor.**

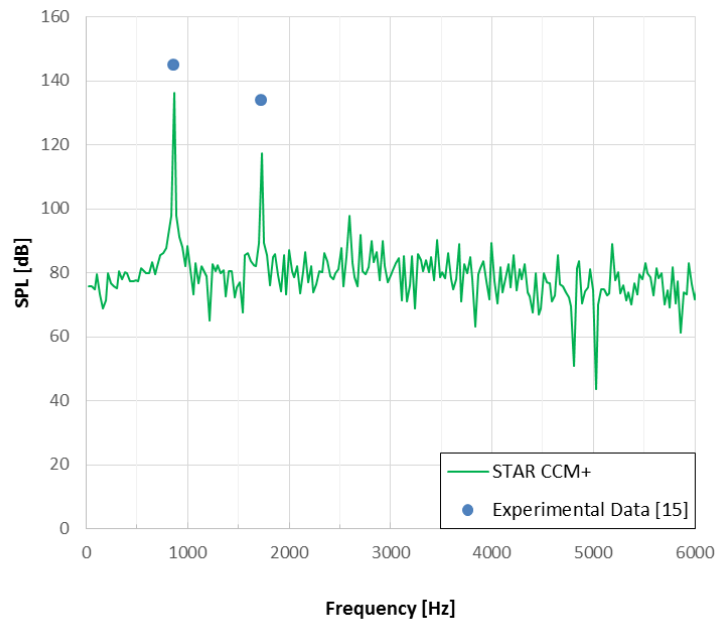


**Fig. 6.6: Noise at transducer 6 predicted in STAR CCM+ from an impermeable FW-H surface.**

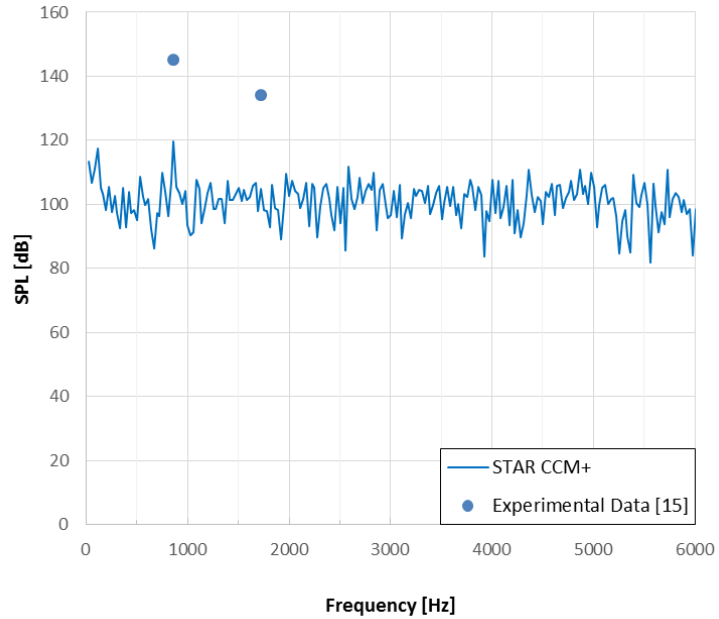


**Fig. 6.7: Noise at transducer 6 predicted in STAR CCM+ from a permeable FW-H surface.**

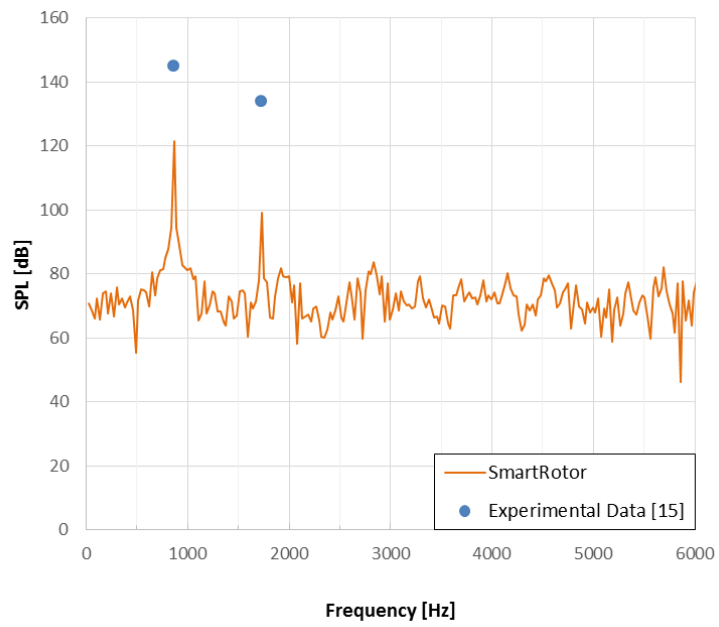


**Fig. 6.8: Noise at transducer 6 predicted in SmartRotor.**

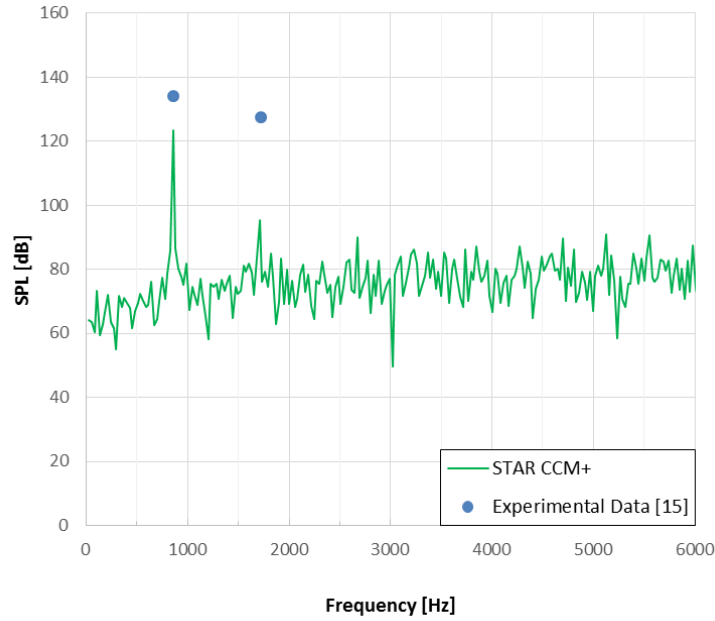


**Fig. 6.9: Noise at transducer 12 predicted in STAR CCM+ from an impermeable FW-H surface.**

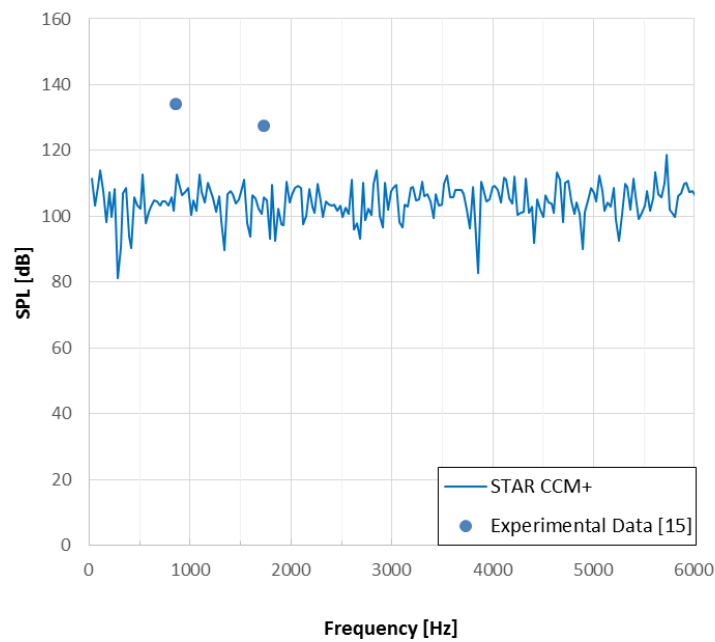


**Fig. 6.10: Noise at transducer 12 predicted in STAR CCM+ from a permeable FW-H surface.**

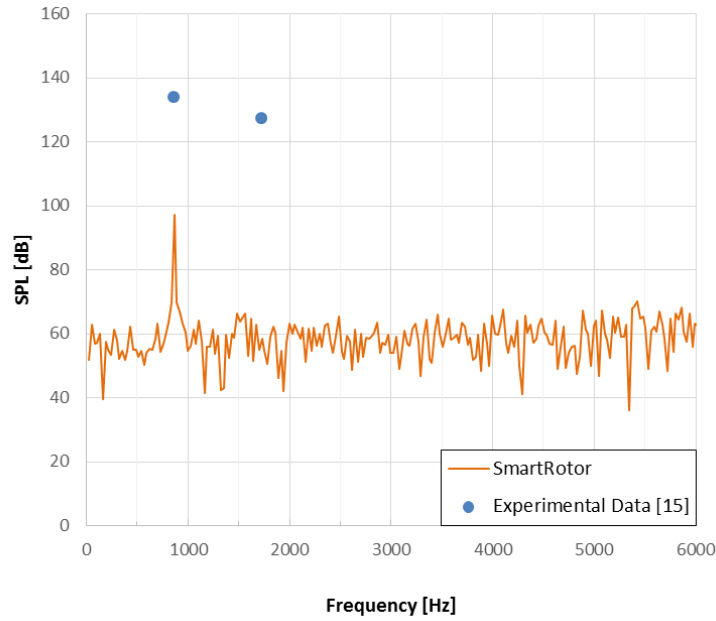


**Fig. 6.11: Noise at transducer 12 predicted in SmartRotor.**

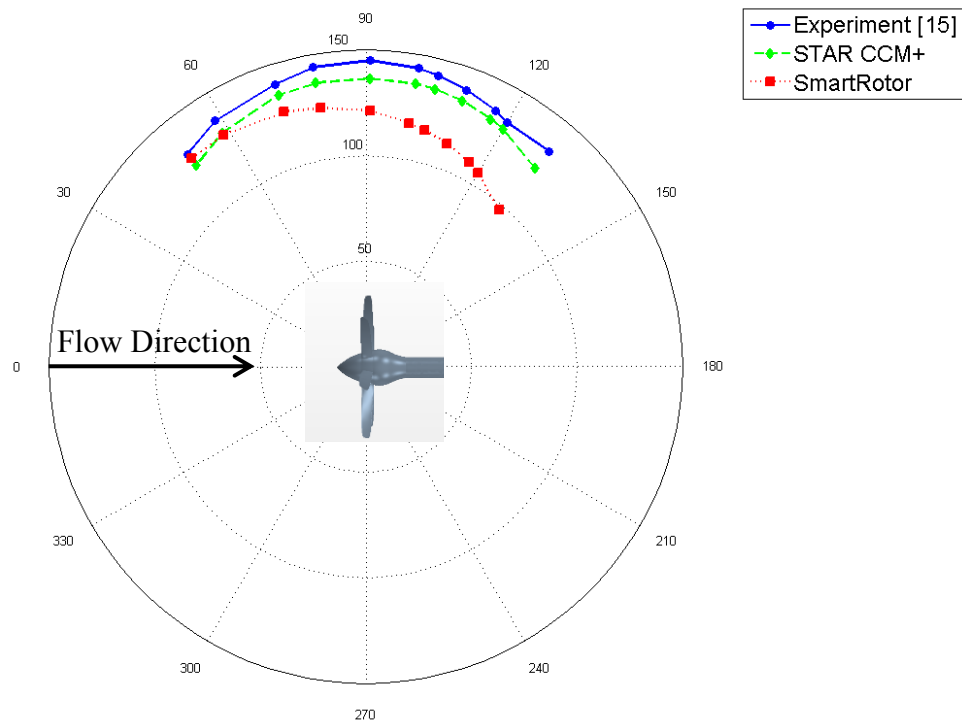


**Fig. 6.12: A polar plot of the first harmonic at the microphone locations around the propeller, located at the origin.**

## **6.4 Chapter Summary**

Now that a basic method for predicting propeller noise has been tested on two validation cases, with first harmonic results within 11 dB for the STAR CCM+ impermeable Ffowcs Williams-Hawkins formulation and within 37 dB for SmartRotor in and behind the propeller plane, a parametric study will be performed following the method developed in the previous two chapters. These results will be discussed further in Chapter 8.

# Chapter 7: Parametric Study on the Impact of Blade Count on Propeller Noise

## 7.1 Background

Since the 1950s, it has been well established that increasing the number of blades results in a decrease in overall noise, largely through the work of Hubbard [13] in producing his propeller noise charts from the analytical methods of Gutin [8] for thickness and loading noise and the analytical method of Yudin [126] for broadband noise after he had validated them experimentally [21]. An example of one of Hubbard's charts, showing the effect of the number of blades on propeller noise, is shown below.

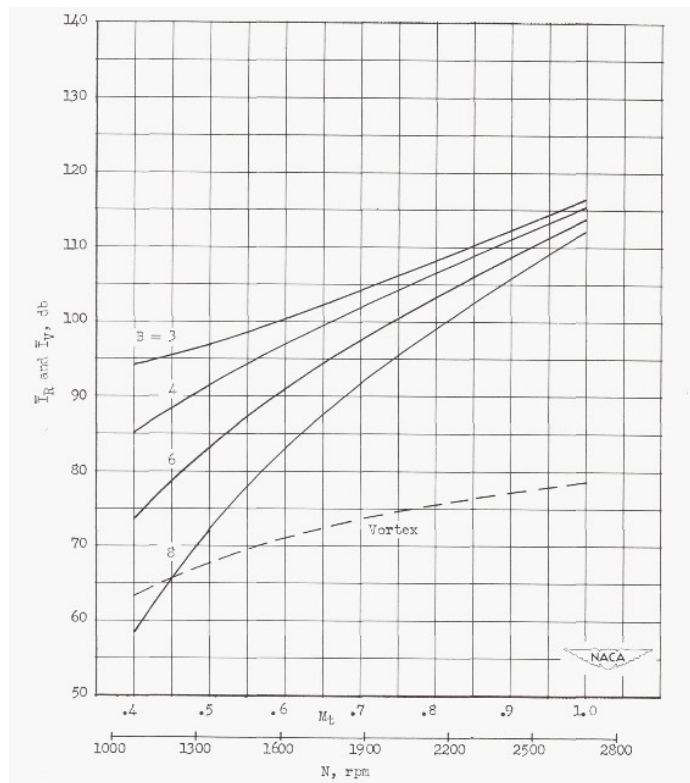


**Fig. 7.1: Propeller sound pressure levels with varying number of blades (B) and rotational mach tip number (M<sub>T</sub>) for an 8 foot diameter propeller [13].**

As can be seen from the chart, increasing the number of blades for a propeller decreases the overall sound level, with a greater effect at lower tip mach numbers. For a given thrust, the increase of blade count is always beneficial in reducing loading and quadrupole noise, resulting in particularly high benefit at lower speeds where loading noise dominates. However, if blade count is increased simply through the addition of blades, thickness noise will increase because the number of sources of thickness noise increases. However, this can be abated by decreasing the blade volume [1].

It should be noted that increasing the number of blades also increases the fundamental blade passage frequency as more blades pass during a given revolution. This results in a set of peak frequencies, which are higher for a larger number of blades. Because the human ear is more sensitive to certain frequencies, as expressed by equal level loudness contours (Fig. 7.2), this change in frequency can make the perceived noise louder.

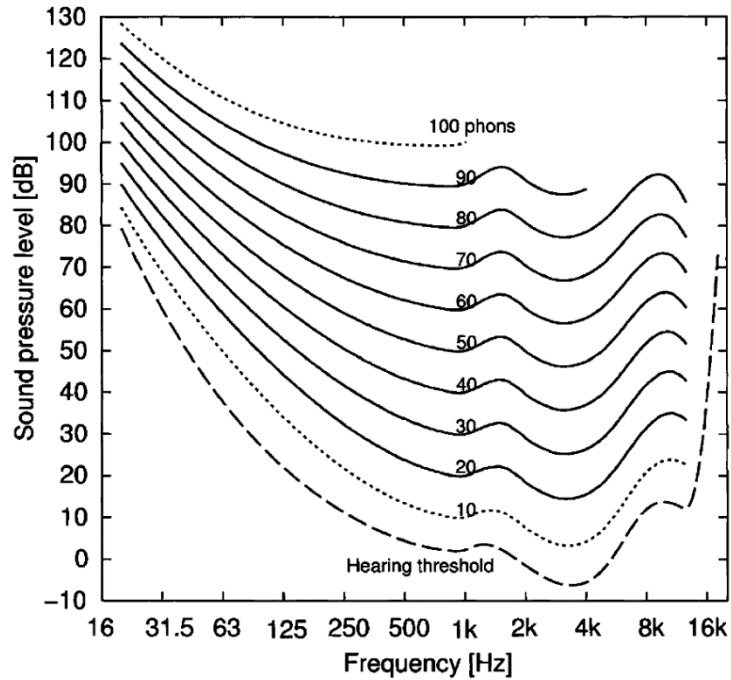


**Fig. 7.2: Equal level loudness contours showing the sensitivity of the human ear [127].**

For example, an 8-bladed propeller operating at 1000 RPM will have harmonic frequencies which are integer multiples of 133 Hz. If this propeller is to have two blades added, the harmonic frequencies will now be multiples of 166 Hz. This puts the first few harmonics in a frequency range which is more sensitive to the human ear, resulting in a relative increase in perceived noise for a given noise level. In addition it should also be noted that increasing blades has an effect on aerodynamic efficiency, weight, and cost.

## 7.2 Parametric Study Setup

The 8-bladed propeller studied in Chapter 6, based on the experiment by Dittmar [15], is selected as the base case for this study because it represents a case of a turboprop at cruise conditions. This study sets all conditions the same as that base case for each propeller other than the number of blades, pitch angle, chord length, and thickness. The propeller was modeled with half of the chord and half of the thickness as a result of an error. However, as the meshing parameters and simulation setup follow the same as those developed in Chapter 5 and Chapter 6, it follows the same simulation methodology which worked well for the previous validation cases. Thus, the data is still presented even though it is less representative of a turboprop propeller. In addition, the simulation times varied from previous simulations: ten revolutions were simulated in STAR CCM+ and nine revolutions were simulated in SmartRotor.

The pitch angle is adjusted to match thrust in each case based on steady state STAR CCM+ simulations. Propellers using 7, 8, and 10 blades are simulated, as shown in Fig. 7.3. A simulation using 6 blades was attempted, but it was not possible to match the thrust for such a propeller at the above conditions. The transducer locations chosen for

this parametric study are shown in Fig. 7.4, with microphones 2, 6, and 12 retained from the SR-2 Test Case 2 in Fig. 2.7. The simulations performed had the parameters listed in Table 7.1.

**Table 7.1: Simulation Conditions for Propeller Blade Count Study**

Property	Value
<b>Propeller</b>	Modified SR-2
<b>Propeller diameter</b>	0.622 m
<b>Mach Number</b>	0.6
<b>RPM</b>	6487

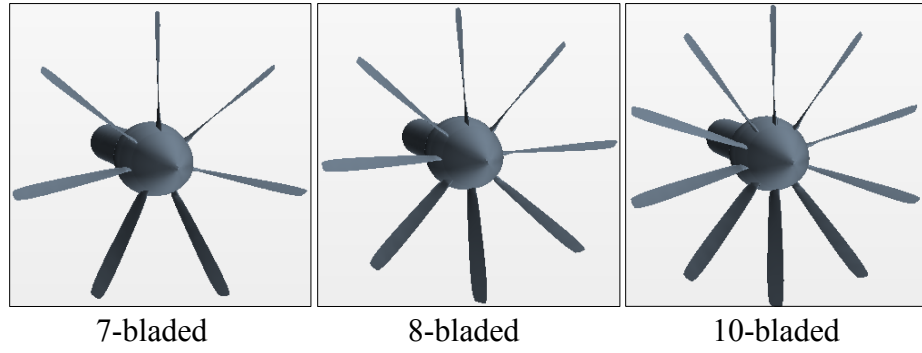


**Fig. 7.3: Propellers studied in blade number study.**

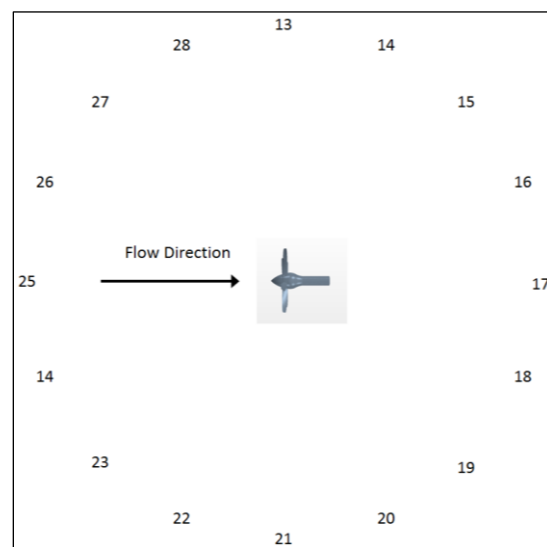


**Fig. 7.4: Transducer locations for parametric study, all located  $16D$  from the propeller.**

### 7.3 Selection of Blade Pitch Angles

The following table shows the selected pitch angles used for each simulation, which were selected by matching thrust to that of the 8-bladed case studied in Chapter 6 using steady state simulations in STAR CCM+.

**Table 7.2: Pitch angles used for blade count study**

Number of Blades	Pitch Angle
7	64.0
8	61.5
10	60.5

### 7.4 STAR CCM+ Simulation Setup

#### 7.4.1 Boundary Conditions and Grid Design

The structure of the grid and simulation utilized for this experiment follows the exact same pattern as that utilized for the validation cases described in Section 5.1.1 and 6.1.1. The domain consisted of a cylinder extending a distance of 10 diameters radially from the propeller, extending a distance of 11 diameters upstream and 21.5 diameters downstream of the propeller (similar to Fig. 5.1). The propeller was constructed according to the airfoil distribution and twist in Fig. 2.4, with a diameter of 0.622 m. However, the thickness and chord length were constructed to be half of the curves listed. A spinner constructed according to Stefko and Jeracki [49] with a shaft which extends all the way through the domain. A stationary region enclosed a rotating cylindrical region which encapsulated the propeller, resulting in two regions for this case. The rotating cylinder has a diameter of 0.84 m (135% of the propeller diameter), extending 0.21 m upstream and 0.42 m downstream of the propeller. The grid for the 8-bladed propeller is similar to

that shown in Fig. 6.1, while the grids for the 7-bladed and 10-bladed propeller are shown in Fig. 7.5.

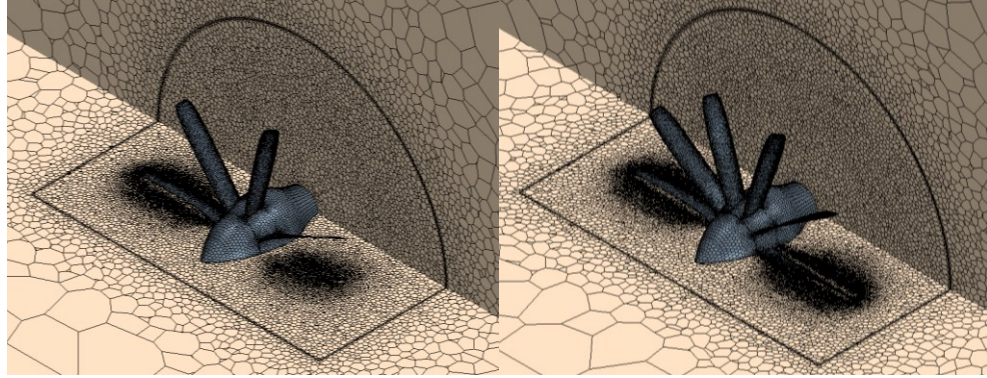


**Fig. 7.5: Grid generated for 7-bladed (left) and 10-bladed (right) Propeller.**

As this case is based upon the 8-bladed case in the previous Chapter, the boundary conditions are the same as listed in Table 6.1. A polyhedral grid was constructed with the same general and refinement properties described in the previous chapter (Table 6.2 and Table 6.3), other than grid size. A grid was created for the domain extending 1 diameter upstream and 1.5 diameters downstream of the propeller. This grid was then extruded normally upstream and downstream to fill out the entire domain, with the same properties described in the previous chapter (Table 6.4). The grid sizes are listed in the table below.

**Table 7.3: Grid Sizes for Blade Count Parametric Study**

Simulation	Number of Cells
<b>7-Bladed Propeller</b>	5,388,297
<b>8-Bladed Propeller</b>	6,196,207
<b>10-Bladed Propeller</b>	7,391,436

The convergence criteria are the same as those for the 8-bladed SR-2 validation case listed in Section 6.1.4. Grid refinement studies were not performed for the 7- and 10-bladed propeller, though both simulations used the same grid setup procedure utilized for

the two previous validation studies. For the 8-bladed simulation, the following results for thrust and torque were obtained for mesh sizes of 2.6, 6.2, and 10 million cells:

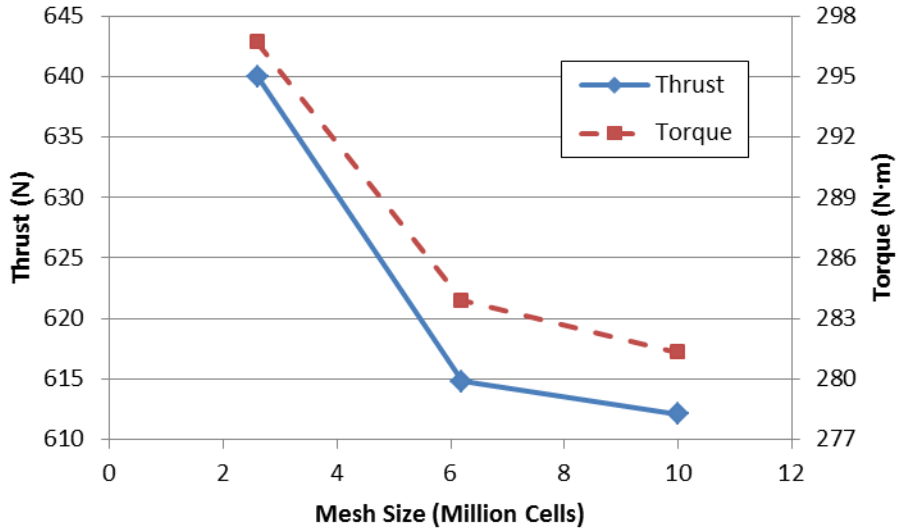


**Figure 7.6: Grid refinement study for 8-bladed propeller used in parametric study.**

#### 7.4.2 STAR CCM+ Solver Selection and Simulation Properties

All flight conditions were set according to the experimental conditions listed in Table 2.3. To initialize the solution, the same steps were taken as listed in Section 6.1.2. The unsteady parameters utilized are listed in the simulations match those done in the previous chapter in Table 6.6. Impermeable FW-H surfaces were used for all acoustic calculations in STAR CCM+. Simulation properties for each case are listed in Table 7.4.

**Table 7.4: Simulation Properties for Blade Count Parametric Study**

Property	7-Bladed Propeller	8-Bladed Propeller	10-Bladed Propeller
<b>Simulation Length</b>	0.0925 s 7200 time steps 10 revolutions	0.0925 s 7200 time steps 10 revolutions	0.0925 s 7200 time steps 10 revolutions
<b>Time step</b>	$1.28462 \times 10^{-5}$ s	$1.28462 \times 10^{-5}$ s	$1.28462 \times 10^{-5}$ s
<b>Inner Iterations per time step</b>	10	10	10
<b>CPUs Utilized</b>	40 (HPCVL)	40 (HPCVL)	40 (HPCVL)
<b>Wall clock time per time step</b>	135 sec	143 sec	158 sec
<b>Total wall clock time</b>	282 hours	297 hours	317 hours

## 7.5 SmartRotor Simulation Setup

The SmartRotor simulation geometry was set up according to the airfoil distribution and twist in Fig. 2.4, with a diameter of 0.622 m. However, the thickness and chord length were constructed to be half of the curves listed. The flow conditions were set to the experiment conditions in Table 2.3, and the following simulation parameters listed in Table 7.5.

**Table 7.5: SmartRotor Simulation Properties for Blade Count Parametric Study**

Property	7-Bladed Propeller	8-Bladed Propeller	10-Bladed Propeller
<b>Simulation Length</b>	0.08324 s 1620 time steps 9 revolutions	0.08324 s 1620 time steps 9 revolutions	0.08324 s 1620 time steps 9 revolutions
<b>Time step</b>	$5.1385 \times 10^{-5}$ s	$5.1385 \times 10^{-5}$ s	$5.1385 \times 10^{-5}$ s
<b>Spanwise Elements</b>	16	16	16
<b>Chordwise Elements</b>	8	8	8
<b>CPUs Utilized</b>	6 (Desktop)	6 (Desktop)	6 (Desktop)
<b>Wall clock time per time step</b>	140 sec	182 sec	282 sec
<b>Total wall clock time</b>	63 hours	82 hours	127 hours

As described in Section 5.2.1 and 6.2.1 no specific convergence criteria were used.

The analyzed data only contained values with converged aerodynamic data, which also corresponded to uniform acoustic pressure data. Verification studies in SmartRotor were not performed for any of these cases.

## 7.6 Results of Parametric Study

The following aerodynamic performance results were calculated from the unsteady simulations:

**Table 7.6: Aerodynamic Results for Blade Count Parametric Studies**

Simulation	Software	Thrust (N)	Torque (N·m)	$C_T$	$C_P$
<b>7-Bladed Propeller</b>	<b>STAR CCM+</b>	608.4	315.0	0.28	1.48
	<b>SmartRotor</b>	628.2	224.8	0.29	1.06
<b>8-Bladed Propeller</b>	<b>STAR CCM+</b>	616.3	284.3	0.29	1.34
	<b>SmartRotor</b>	563.8	198.7	0.26	0.94
<b>10-Bladed Propeller</b>	<b>STAR CCM+</b>	620.6	277.6	0.29	1.31
	<b>SmartRotor</b>	603.8	213.5	0.28	1.01

Plots showing the PSD values for transducers 13, 15, and 17, all located at a distance of  $16D$  from the propeller, are shown in Fig. 7.7-Fig. 7.15 for both STAR CCM+ and SmartRotor. Table 7.7 lists the magnitudes of the BPFs for all of the simulations.

As can be seen from the data, the increase of blade count decreases the noise in every case according to both STAR CCM+ and SmartRotor, by an amount that varies depending on direction. In the rotational axis, where noise is the highest (transducer 13 and 21), the reduction in noise for an 8-bladed and 10-bladed propeller compared to a 7-bladed propeller is about 2 and 7 dB, respectively, for the first harmonic according to

STAR CCM+ simulations. SmartRotor predicts a reduction of about 4 and 10 dB, respectively.

The maximum predicted reduction occurs at the 45 degree angle (transducers 15, 19, 23, and 27). For the 8-bladed propeller, compared to the 7-bladed propeller, STAR CCM+ predicts a noise reduction of 5 dB and SmartRotor predicts a reduction of 6-8 dB in this direction. Similarly, for the 10-bladed propeller, compared to the 7-bladed propeller, STAR CCM+ predicts a noise reduction of about 15 dB and SmartRotor predicts a reduction of between 14 and 21 dB. There is an even greater reduction in noise at higher harmonics, though it should be noted that in the previous validation studies the higher harmonics were not as accurately predicted.

There is discrepancy between the directionality of radiated noise between the two codes, as shown in Fig. 7.16 - Fig. 7.18. This was also seen earlier in the second propeller validation case in Fig. 6.12. SmartRotor predicts higher noise in front of the propeller, while STAR CCM+ predicts higher noise behind the propeller, as is typical with the theoretical distribution of loading noise as described in [128].

**Table 7.7: Total Noise in dB at BPFs for 7-, 8-, and 10- Bladed Propellers**

Transducer	BPF	7-Bladed Propeller		8-Bladed Propeller		10-Bladed Propeller	
		STAR-CCM+	SmartRotor	STAR-CCM+	SmartRotor	STAR-CCM+	SmartRotor
13	1	113.3	98.3	110.9	94.4	106.6	88.8
	2	96.7	78.4	91.7	72.0	83.0	61.6
	3	79.0	59.9	72.4	51.7	*	40.7
14	1	109.5	84.8	106.5	79.7	101.1	71.7
	2	88.8	56.7	83.0	47.7	73.7	*
	3	65.6	*	*	*	*	*
15	1	94.8	63.2	89.7	55.3	79.2	42.0
	2	58.1	*	*	*	*	*
16	1	63.4	27.5	*	*	59.2	*
	2	53.4	*	*	*	*	*
17	1	51.9	*	59.9	*	55.5	*
18	1	60.3	*	*	*	*	*
	2	49.3	*	*	*	*	*
19	1	92.4	63.3	87.2	55.3	77.3	42.0
	2	58.0	*	*	*	*	*
20	1	109.5	84.9	106.5	79.7	101.2	71.7
	2	89.0	56.2	83.0	47.7	69.9	*
	3	66.6		*	26.9	*	*
21	1	113.3	98.3	110.9	94.4	106.6	88.8
	2	96.7	78.5	91.8	72.0	82.4	61.6
	3	79.2	59.9	73.1	51.7	*	*
22	1	108.3	106.4	105.2	102.7	99.8	97.2
	2	87.5	87.0	81.5	80.6	68.6	70.0
	3	65.5	67.2	87.4	58.3	*	*
23	1	92.4	100.2	*	94.4	77.3	86.1
	2	58.0	66.3	*	56.6	*	*
24	1	55.1	48.3	*	*	*	
	2	*	*	*	*	*	
25	1	*	*	*	*	*	
26	1	54.3	46.9	*	*	*	
	2	*	*	*	*	*	
27	1	92.4	100.2	87.2	94.4	76.9	86.1
	2	59.3	66.2	*	56.7	*	*
28	1	108.3	106.4	105.2	102.7	99.7	97.2
	2	87.6	87.2	81.1	80.6	72.6	70.0
	3	64.8	67.3	*	58.3	*	*

\*Peak not visible above background noise

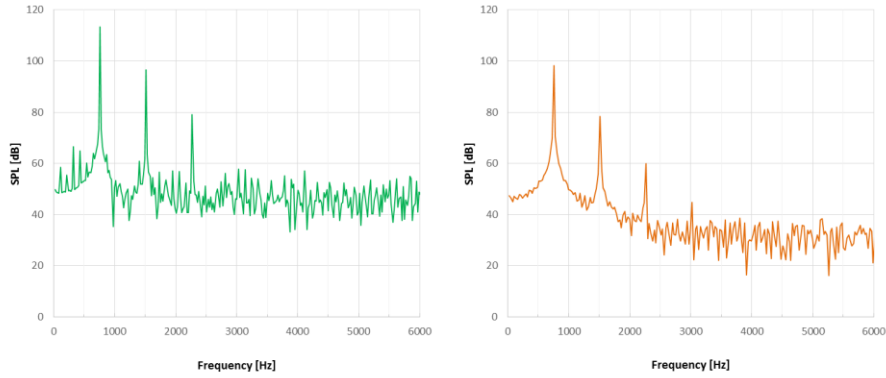


**Fig. 7.7: Noise predicted at transducer 13 in STAR CCM+ (left) and SmartRotor (right) for 7-Bladed Propeller.**

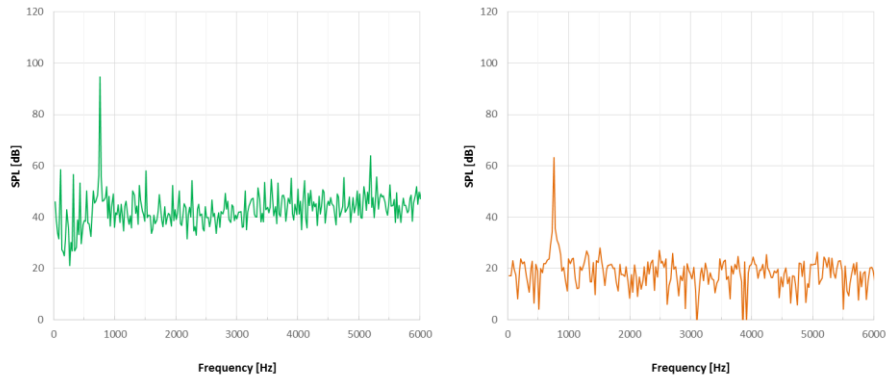


**Fig. 7.8: Noise predicted at transducer 15 in STAR CCM+ (left) and SmartRotor (right) for 7-Bladed Propeller.**

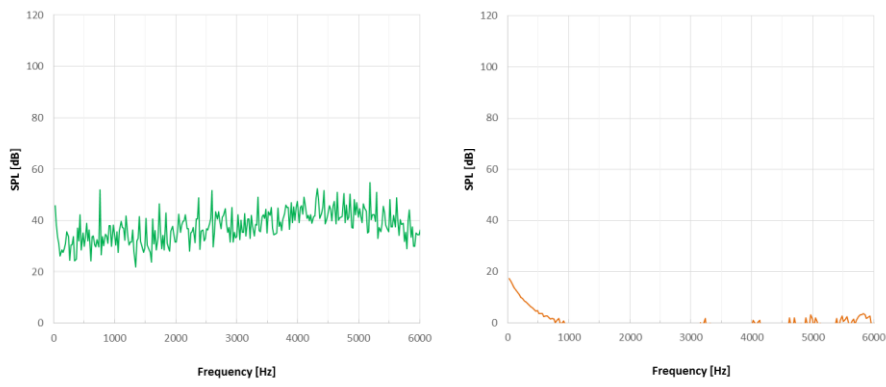


**Fig. 7.9: Noise predicted at transducer 17 in STAR CCM+ (left) and SmartRotor (right) for 7-Bladed Propeller.**

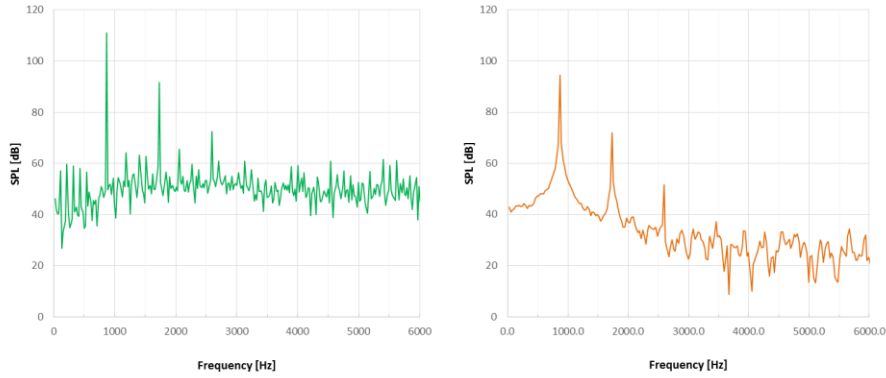


**Fig. 7.10: Noise predicted at transducer 13 in STAR CCM+ (left) and SmartRotor (right) for 8-Bladed Propeller.**

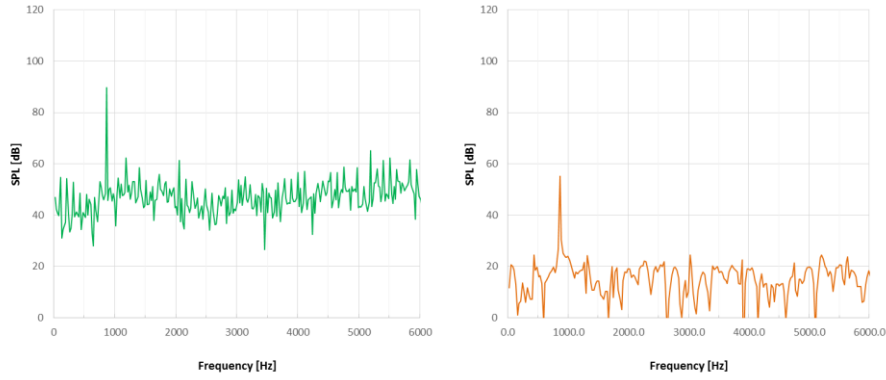


**Fig. 7.11: Noise predicted at transducer 15 in STAR CCM+ (left) and SmartRotor (right) for 8-Bladed Propeller.**

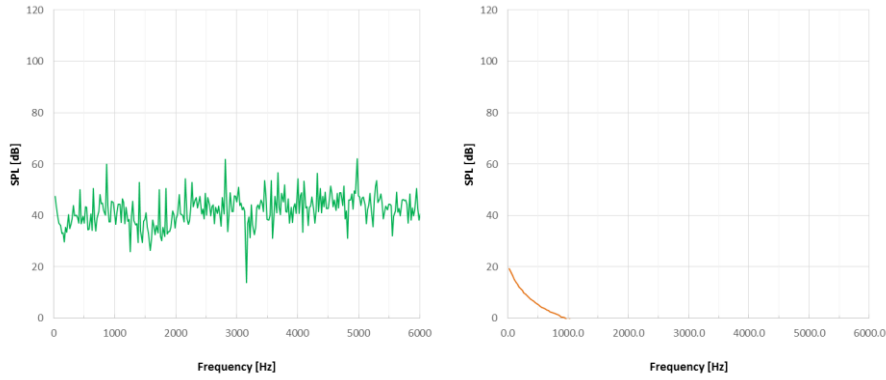


**Fig. 7.12: Noise predicted at transducer 17 in STAR CCM+ (left) and SmartRotor (right) for 8-Bladed Propeller.**

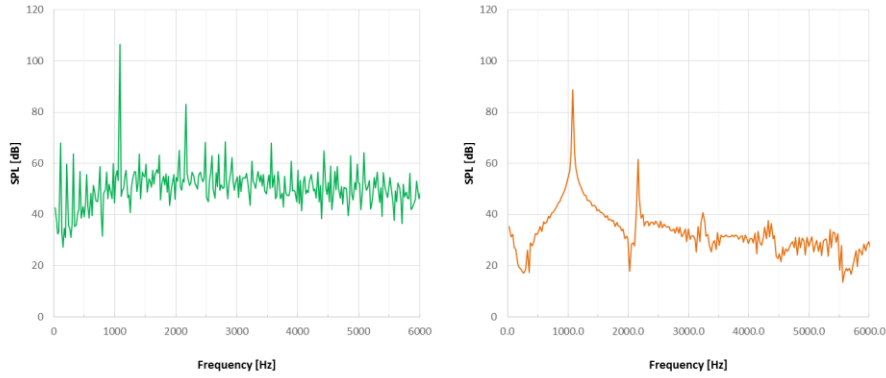


**Fig. 7.13: Noise predicted at transducer 13 in STAR CCM+ (left) and SmartRotor (right) for 10-Bladed Propeller.**

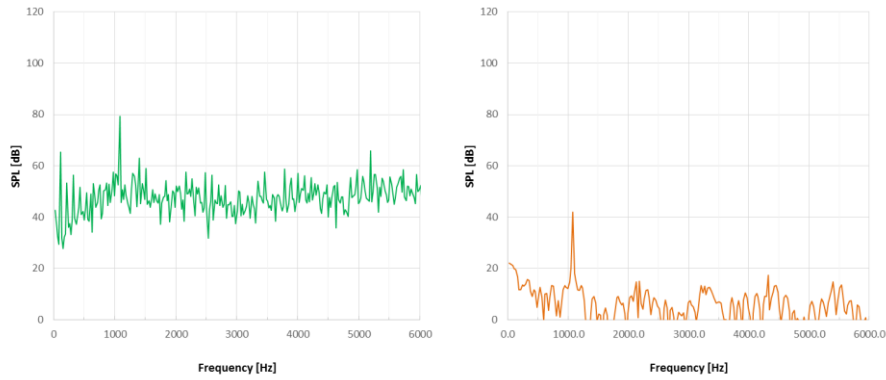


**Fig. 7.14: Noise predicted at transducer 15 in STAR CCM+ (left) and SmartRotor (right) for 10-Bladed Propeller.**

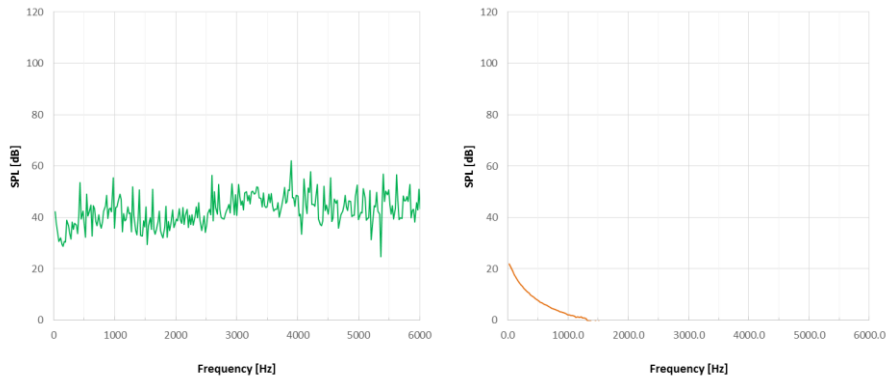


**Fig. 7.15: Noise predicted at transducer 17 in STAR CCM+ (left) and SmartRotor (right) for 10-Bladed Propeller.**

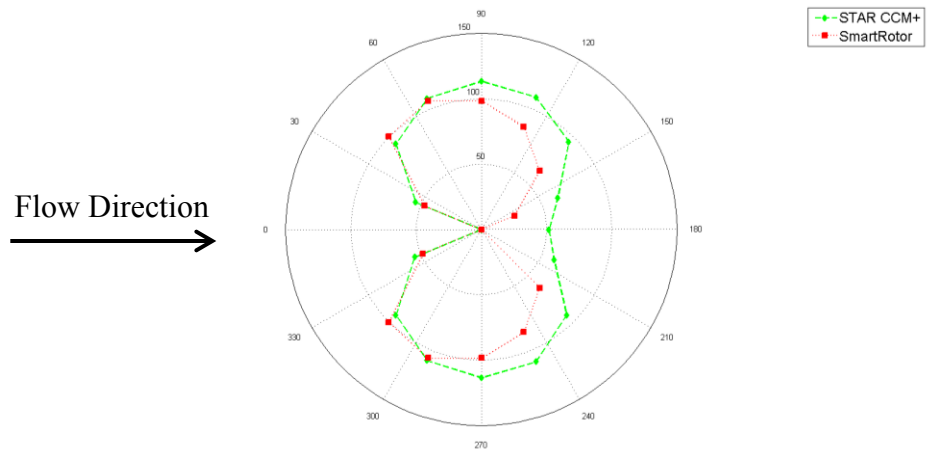


**Fig. 7.16:** Predicted directivity of first harmonic of 7-Bladed Propeller.

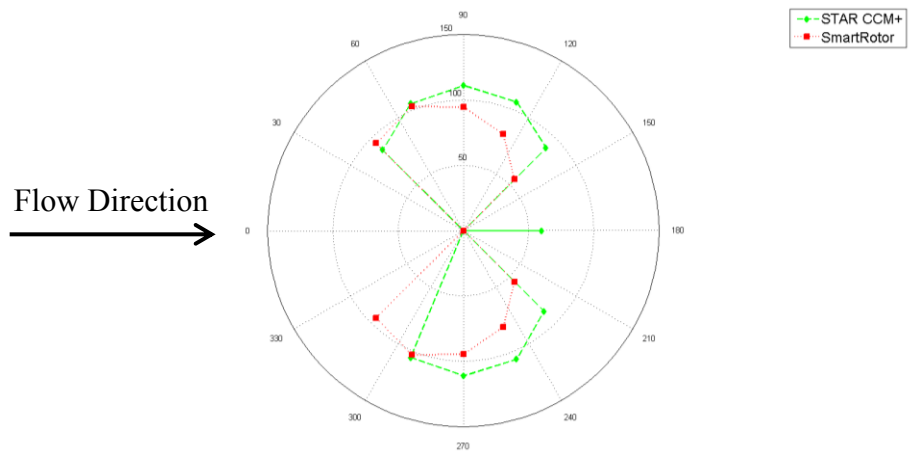


**Fig. 7.17:** Predicted directivity of first harmonic of 8-Bladed Propeller.

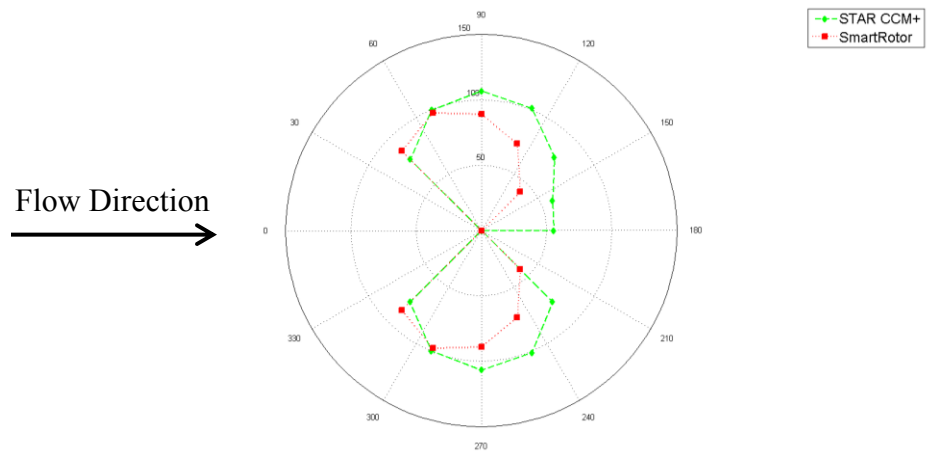


**Fig. 7.18:** Predicted directivity of first harmonic of 10-Bladed Propeller.

# **Chapter 8: Conclusions and Recommendations for Future Work**

## **8.1 STAR CCM+ Code Validation**

The tandem cylinder case resulted in predictions for  $C_p$  which fell very close to the experimental results. Peak frequencies were predicted within 10 dB of experiment and matching the shedding frequency within 1 Hz using a grid size of only 5.2 million cells. To put the grid size in perspective, at the First Workshop on Benchmark problems for Airframe Noise Computations in 2011, grid sizes were typically in the range of 10 to 133 million cells, with only one solution submission composed of a grid smaller than the one employed in this thesis. This illustrates that reasonable results for noise emission can be obtained with a relatively small grid in simulating a very complex flow condition, though finer grids should be employed to better verify the solution's grid dependence.

Both propeller validation cases showed very good comparison to experimental results relative to other available propeller simulations when impermeable surfaces were used. For the first test case, harmonic predictions within 20 dB of the experiment were predicted for all five harmonics, with the first harmonic being over predicted by 10 dB above experimental results without any added adjustments. For the second test case, the first harmonics were all within 11 dB of experimental values. Based on correction factors utilized in the literature as described in Section 2.4, a pressure correction could be added, but this will be less than one dB for the speeds tested in the first case. In the second case, with the operating wind tunnel pressure of 90 kPa [29], this adjustment would only amount to one dB according to Eq. 2.1 based on the simulation pressure of 101 kPa,

bringing the results one dB closer to the experimental results. Additionally, an adjustment factor could be added in for the effect of the wind tunnel since the wind tunnel alone noise spectra is provided by Soderman and Horne [12]. For the impermeable results, this would result in an addition of 0.9, 0.3, and 0.2 dB for the first three harmonics, respectively, at Mic 7. Assuming that the wind tunnel noise is the same, correcting for the distance between the mics, at Mic 12 as at Mic 7, an adjustment can also be made for the wind tunnel at Mic 12. This would result in an addition of 0.5, 0.2, and 0.1 dB at the first, second, and third harmonics, respectively, for Mic 12. As the second test case does not provide any wind tunnel data, this effect cannot be quantified.

The permeable surface formulation of the Ffowcs Williams-Hawkins equation did not produce good results, perhaps influenced by a poor choice of a permeable surface.

## 8.2 SmartRotor Code Validation

The SmartRotor propeller validation results were varying in their accuracy, being more dependent upon microphone location than the STAR CCM+ impermeable results. For the first test case, the harmonics were all predicted within 10 dB. The second test case had first harmonics predicted to between 3 and 37 dB different than experimental results depending on the location of the microphones. The aerodynamic results of thrust and torque appear to be over-predicted in the code for reasons unknown at this time.

One possibility for the discrepancy is that the input airfoil data into SmartRotor may not be correct. The data is based on previous 2D simulations in CFD not performed by the author, as experiments for the tested airfoil sections could not be found in literature. This

data is presented in Appendix C. As the data has been used in BEMT and SmartRotor with reasonable results, the data has not been verified. Additionally, SmartRotor interpolates between the Mach numbers supplied in the input data, and the linear interpolation may be resulting in inaccurate data because of the limited input data. This also may be the cause of the directivity discrepancy if the relative thrust and torque along the blade are not being correctly predicted. It also may explain why SmartRotor over or under predicted thrust data relative to STAR CCM+ in the blade count study depending on the pitch angle.

As discussed in the Section 8.1, an adjustment could be made to add one dB to the simulated result to adjust for pressure differences according to Eq. 2.1., bringing the results one dB closer to the experimental results for the second test case. The adjustment for pressure differences in the first case would account for less than one dB. Additionally, an adjustment factor could be added in for the effect of the wind tunnel since the wind tunnel alone noise spectra is provided by Soderman and Horne [12]. This would result in an addition of 4.7, 5.3, and 4.5 dB for the first three harmonics, respectively, at Mic 7. Assuming that the wind tunnel noise is the same, correcting for the distance between the mics, at Mic 12 as at Mic 7, an adjustment can also be made for the wind tunnel at Mic 12. This would result in an addition of 3.3, 2.1, and 1.8 dB at the first, second, and third harmonics, respectively, for Mic 12. As the second test case does not provide any wind tunnel data, this effect cannot be quantified. This brings the results slightly closer to experiment, but still under-predicts experimental data. For the second validation test case, wind tunnel noise data was not provided and thus an adjustment cannot be quantified.

### **8.3 Parametric Study Results**

Both simulation softwares predicted a decrease in noise with an increasing number of propeller blades, in accordance with theory. For a 7-bladed SR-2 propeller, the loudest harmonic (in the propeller plane) was predicted to be 113 dB in STAR CCM+ and 98 dB in SmartRotor. It was found that the loudest harmonic was decreased by 2 dB (STAR CCM+ simulation) and 4 dB (SmartRotor simulation) in increasing the number of blades from 7 to 8 with an adjustment in pitch angle to maintain thrust. If the blades are increased to 10, again maintaining thrust by adjusting pitch, the loudest harmonic was reduced by 7 dB (STAR CCM+) and 10 dB (SmartRotor). At successive harmonics, the reduction in noise is even more significant.

It should be noted that if the propeller was not a scale model, with high RPM values to match tip speeds, the blade passage frequencies would be lower and increasing the number of blades may bring the perceived noise level higher because of a shifting of frequency.

### **8.4 Feasibility of Using the Codes for Propeller of Propeller Noise**

Good comparison to the experiment was shown in this work, however, results were still being predicted with discrepancies of up to 20 dB for first harmonics in STAR CCM+ and up to 37 dB in SmartRotor, though this was highly dependent upon transducer location. This margin of error is quite high for most purposes. Consequently, further work should be performed on this work to understand any adjustments that should be made to the simulated or experimental data, as well as to understand why noise was over

predicted by STAR CCM+ in the first case and under predicted in the second case. As STAR CCM+ predicted the noise much better in the second validation case in terms of magnitude and directivity, more investigation should be performed into the reasons for this.

SmartRotor run times were significantly less, on the order of hours compared to days even on a much smaller computing system. Additionally, the simulation setup is relatively simple. If the reasons for the directivity discrepancy are discovered, this code shows good promise for fast and accurate calculation of propeller noise.

## 8.5 Recommendations for Future Work

Many of the simulations here used less extensive grids and time parameters than typically employed for computational aeroacoustics. In order to fully evaluate the effectiveness of the grid or panel sizes and time steps utilized, further verification of the simulations should be performed particularly to increase confidence in the parametric study results. Particularly, the verification studies on the first propeller validation case should be done as the grid refinement still yielded discrepancies of 5% in thrust and torque compared to a lower value in the first test case.

Regarding improving the propeller simulations in STAR CCM+, the impact of domain size was not explored at all and should be studied for a more comprehensive method for reliable propeller noise prediction. Though Permeable Ffowcs Williams-Hawkins surfaces in STAR CCM+ have been shown to provide good results, such as in [57], the

results obtained in this work were poor. Thus, further exploration of permeable surface definition for good practice can be explored. However, given the good performance of the predictions of the impermeable surfaces, the main advantages are likely not going to be realized except for simulations which contain significant quadrupole noise.

As discussed in Section 8.2, the input curves into SmartRotor should be verified. Additionally, the directional characteristics of the acoustic solver in SmartRotor seem to be inconsistent with experiment and STAR CCM+, which has directional characteristics which compare to the experiment more reliably. This is likely due to how the acoustic path is calculated and modified with flight speed as it seems to over-predict in front of the propeller and under-predict behind the propeller, relatively. Understanding the reasons for these discrepancies is important in the continuing evolution of the code.

Finally, steady state simulations are significantly faster than the unsteady simulations in STAR CCM+. If an acoustic model were to simply rotate steady propeller results in time, including the computed turbulence properties, this would be a much faster way to predict noise and is worth exploring. Though STAR CCM+ has a steady state Ffowcs Williams-Hawkins solver, it was not found to give reasonable results for the simulations performed in this work.

## References

- [1] B. Maglizzzi, D. B. Hanson, and R. K. Amiet, "Propeller and Propfan Noise," *Aeroacoustics of Flight Vehicles: Theory and Practice*. pp. 1–61, 2004.
- [2] D. C. Mikkelsen, G. A. Mitchell, and L. J. Bober, "Summary of Recent NASA Propeller Research," *Nasa TM 83733*. 1984.
- [3] N. Dickson, "ICAO Noise Standards," in *ICAO Symposium on Aviation and Climate Change*, 2013.
- [4] A. Betz, "Considerations on Propeller Efficiency," *NACA TM 481*. Washington, 1928.
- [5] W. E. Sullivan, J. E. Turnberg, and J. A. Violette, "Large-Scale Advanced Prop-Fan (LAP) Blade Design," *NASA CR 174790*. 1984.
- [6] F. J. H. Lynam and H. A. Webb, "The Emission of Sound by Airscrews," *NACA TM 624*. London, pp. 792–801, 1919.
- [7] F. B. Metzger, "An Assessment of Propeller Aircraft Noise Reduction Technology," *NASA Contract. Rep.*, 1995.
- [8] L. Gutin, "On the Sound Field of a Rotating Propeller," *NACA TM 1195*. 1936.
- [9] M. J. Lighthill, "On Sound Generated Aerodynamically -I. General Theory," *Proc. R. Soc.*, pp. 564–587, 1952.
- [10] J. E. Ffowcs Williams and D. L. Hawkings, "Sound Generation by Turbulence and Surfaces in Arbitrary Motion," *Philos. Trans. R. Soc. London*, vol. A264, pp. 321–342, 1969.
- [11] W. Dobrzhynski, H. Heller, J. Powers, and J. Densmore, "Propeller Noise Tests in the German-Dutch Wind Tunnel DNW," *FAA Report No. AEE 86-3*. 1986.
- [12] P. T. Soderman and W. C. Horne, "Acoustic and Aerodynamic Study of a Pusher-Propeller Aircraft Model," *NASA TP 3040*, 1990.
- [13] H. Hubbard, "Propeller-Noise Charts for Transport Airplanes," *NACA TN 2968*. Washington, DC, 1953.
- [14] "Prediction Procedure for Near-Field and Far-Field Propeller Noise," *AIR 1407*. Society of Automotive Engineers, Inc., 1977.
- [15] J. H. Dittmar, "Cruise Noise of the SR-2 Propeller Model in a Wind Tunnel," 1989.
- [16] D. B. Hanson, "Influence of Propeller Design Parameters on Far-Field Harmonic Noise in Forward Flight," *AIAA J.*, vol. 18, no. 11, pp. 1313–1319, 1980.
- [17] E. Paris, "No Title," *Philos. Mag.*, vol. 13, no. 99, 1932.
- [18] C. F. B. Kemp, "Some properties of the sound emitted by airscrews," *Proc. Physical Soc.*, vol. 44, p. 151, 1933.
- [19] W. Hicks and H. Hubbard, "Comparison of Sound Emission from Two-Blade, Four-Blade, and Seven-Blade Propellers," 1947.
- [20] H. Hubbard, "Sound Measurements for Five Shrouded Propellers at Static Conditions," 1950.
- [21] H. Hubbard, "Sound from a two-blade propeller at supersonic tip speeds," in *NACA Report 1079*, 1952.
- [22] M. Karbjun, "Noise Survey of a 10-Foot Four-Blade Turbine-Driven Propeller Under Static Conditions," *NACA TN 3422*, 1955.
- [23] M. Karbjun, "Noise Survey of a Full-Scale Supersonic Turbine-Driven Propeller

- Under Static Conditions," 1957.
- [24] D. Brown and J. B. Ollerhead, "Propeller Noise at Low Tip Speeds," 1973.
- [25] J. H. Dittmar, R. J. Jeracki, and J. B. Bernard, "Tone noise of three supersonic helical tip speed propellers in a wind tunnel at 0.8 Mach Number," 1978.
- [26] J. H. Dittmar, R. J. Jeracki, and J. B. Bernard, "Tone noise of three supersonic helical tip speed propellers in a wind tunnel," 1980.
- [27] J. H. Dittmar and R. J. Jeracki, "Additional Noise Data on the SR-3 Propeller," 1981.
- [28] J. H. Dittmar and R. J. Jeracki, "Noise of the SR-3 propeller model at 2 degree and 4 degree angle of attack," 1981.
- [29] J. H. Dittmar and P. L. Lasagna, "A preliminary comparison between the SR-3 propeller noise in flight and in a wind tunnel," no. TM-82805, 1982.
- [30] J. H. Dittmar, G. L. Stefko, and R. J. Jeracki, "Noise of the 10-Bladed, 40 Degree Swept SR-6 Propeller in a Wind Tunnel," *NASA TM 82950*, 1982.
- [31] G. P. Succi, D. H. Munro, and J. A. Zimmer, "Experimental Verification of Propeller Noise Prediction," *AIAA J.*, vol. 20, no. 11, pp. 1483–1491, 1982.
- [32] J. Sulc, J. Hofr, and L. Benda, "Exterior noise on the fuselage of light propeller driven aircraft in flight," *J. Sound Vib.*, vol. 84, pp. 105–120, Sep. 1982.
- [33] J. H. Dittmar, G. L. Stefko, and R. J. Jeracki, "Noise of the SR-6 Propeller Model at 2 and 4 Degrees Angles of Attack," 1983.
- [34] J. H. Dittmar and P. L. Lasagna, "A Preliminary Comparison Between the SR-6 Propeller Noise in Flight and in a Wind Tunnel," *NASA RM-83341*, 1983.
- [35] W. J. G. Trebble, J. Williams, and R. P. Donnelly, "Propeller noise at model- and full-scale," *J. Aircr.*, vol. 20, no. 1, pp. 34–41, 1983.
- [36] P. J. W. Block and G. L. J. Gentry, "Directivity and Trends of Noise Generated by a Propeller in a Wake," *NASA Tech. Pap.*, 1986.
- [37] R. P. Woodward, I. J. Loeffler, and J. H. Dittmar, "Measured Far-Field Flight Noise of a Counterrotation Turboprop at Cruise Conditions," 1989.
- [38] J. H. Dittmar and D. B. Stang, "Cruise Noise of the 2/9 Scale Model SR-7A Propeller," *J. Aircr.*, vol. 8, no. 8, pp. 740–746, 1988.
- [39] J. B. H. M. Schulten, "Frequency-Domain Method for the Computation of Propeller Acoustics," *AIAA J.*, vol. 26, no. 9, pp. 1027–1035, 1988.
- [40] J. H. Dittmar and D. Hall, "The effect of swirl recovery vanes on the cruise noise of an advanced propeller," vol. 30, no. 2, pp. 221–226, 1990.
- [41] T. Zandbergen, S. Sarin, and R. P. Donnelly, "Experimental/theoretical investigation of the sound field of an isolated propeller, including angle of incidence effects," in *13th Aeroacoustics Conference*, 1990.
- [42] J. H. Dittmar, D. G. Hall, and B. Park, "Detailed Noise Measurements on the SR-7A Propeller : Tone Behavior With Helical Tip Mach Number," no. December, 1991.
- [43] J. Schulten, "Comparison of measured and predicted noise of the Brite-EuRam SNAAP advanced propellers," *3rd AIAA/CEAS Aeroacoustics Conf.*, pp. 923–933, 1997.
- [44] G. Sinibaldi and L. Marino, "Experimental analysis on the noise of propellers for small UAV," *Appl. Acoust.*, vol. 74, no. 1, pp. 79–88, 2013.
- [45] M. Nallasamy, R. P. Woodward, and J. F. Groeneweg, "High-Speed Propeller

- Performance and Noise Predictions at Takeoff/Landing Conditions," *J. Aircr.*, vol. 26, no. 6, pp. 563–569, 1989.
- [46] R. Woodward, "Measured noise of a scale model high speed propeller at simulated takeoff/approach conditions," *Nasa Tm 88920*, 1987.
- [47] C. E. Whitefield, P. R. Gliebe, R. Mani, and P. Mungur, "High Speed Turboprop Aeroacoustic Study ( Single Rotation )," *NASA CR 182257*, 1989.
- [48] "Jetstar Propeller Flight Test Program Acoustic Data Report," 1982.
- [49] G. L. Stefko and R. J. Jeracki, "Wind-Tunnel Results of Advanced High-Speed Propellers at Takeoff, Climb, and Landing Mach Numbers," *Nasa Tm-87030*, 1985.
- [50] G. L. Stefko, G. E. Rose, and G. G. Podboy, "Wind Tunnel Performance Results of an Aeroelastically Scaled 2/9 Model of the PTA Flight Test Prop-Fan," *AIAA/ASME/SAE/ASEE 23rd Jt. Propuls. Conf.*, vol. 5, 1987.
- [51] J. H. M. Schulten, "Effects of Asymmetric Inflow on Near-Field Propeller Noise," vol. 34, no. 2, 1996.
- [52] J. Schulten, "Comparison of measured and predicted noise of the Brite-EuRam SNAAP advanced propellers," *3rd AIAA/CEAS Aeroacoustics Conf.*, pp. 923–933, 1997.
- [53] M. De Gennaro, D. Caridi, and M. Pourkashanian, "Ffowcs Williams-Hawkings Acoustic Analogy for Simulation of Nasa SR2 Propeller Noise in Transonic Cruise Condition," in *V European Conference on Computational Fluid Dynamics*, 2010.
- [54] A. Pagano, M. Barbarino, D. Casalino, and L. Federico, "Tonal and Broadband Noise Calculations for Aeroacoustic Optimization of a Pusher Propeller," *J. Aircr.*, vol. 47, no. 3, pp. 835–848, 2010.
- [55] D. Boots and D. Feszty, "Numerical Investigation of the Effect of Wing Position on the Aeroacoustic Field of a Propeller," in *52nd AIAA/SAE/ASEE Joint Propulsion Conference*, 2016.
- [56] D. Caridi, "Industrial CFD Simulation of Aerodynamic Noise," Universita degli Studi di Napoli Federico II, 2008.
- [57] K. Moussa, "Computational Modeling of Propeller Noise : NASA SR-7A Propeller," University of Waterloo, Waterloo, ON, 2014.
- [58] D. Boots, "Numerical Predictions of Propeller-Wing Interaction Induced Noise in Cruise and Off-Design Conditions," Carleton University, 2016.
- [59] S. Subramanian, "Experimental and Computational Studies on Propeller Noise Due to Inflow Distortion," *Arbor Cienc. Pensam. Y Cult.*, 2000.
- [60] B. Marinus, "Multidisciplinary Optimization of Aircraft Propeller Blades," Centrale Lyon - University Lyon, 2011.
- [61] L. N. Jenkins, D. Neuhart, and C. McGinley, "Measurements of unsteady wake interference between tandem cylinders," in *36th AIAA Fluid Dynamics Conference and Exhibit*, 2006.
- [62] L. N. Jenkins, M. R. Khorrami, M. Choudhari, and C. B. McGinley, "Characterization of unsteady flow structures around tandem cylinders for component interaction studies in airframe noise," *AIAA Pap.*, no. 2812, 2005.
- [63] D. Neuhart, L. N. Jenkins, M. Choudhari, and M. R. Khorrami, "Measurements of the Flowfield Interaction Between Tandem Cylinders," *AIAA Pap.*, vol. 3275, 2009.

- [64] F. Hutcheson and T. F. Brooks, “Noise Radiation from Single and Multiple Rods Configurations,” *Int. J. Aeroacoustics*, vol. 11, no. 3&4, pp. 291–334, 2012.
- [65] F. Hutcheson, T. F. Brooks, D. P. Lockard, M. Choudhari, and D. J. Stead, “Acoustics and surface pressure measurements from tandem cylinder configurations,” in *20th AIAA/CEAS Aeroacoustics Conference*, 2014, no. 2762, pp. 1–17.
- [66] G. A. Brès, D. Freed, M. Wessels, S. Noelting, and F. Pérot, “Flow and noise predictions for the tandem cylinder aeroacoustic benchmark,” *Phys. Fluids*, vol. 24, no. 3, 2012.
- [67] M. Caraeni, O. Aybay, and S. Holst, “Tandem Cylinder and Idealized Side Mirror Far-Field Noise Predictions Using DES and An Efficient Implementation of FW-H Equation,” in *17th AIAA/CEAS Aeroacoustics Conference*, 2011.
- [68] T. Deloze, F. Deliancourt, Y. Hoarau, and M. Braza, “Turbulent Simulation of the Flow around Two Cylinders in Tandem Configuration,” in *Turbulence and Interactions*, Springer Berlin Heidelberg, 2014, pp. 47–53.
- [69] Y. Detandt, M. Cabrol, R. Leneveu, D. D. Udekem, F. Mendonca, and D. Burd, “Computational Aero-Acoustics.” 2011.
- [70] C. Doolan, “Flow and noise simulation of the NASA tandem cylinder experiment using OpenFOAM,” in *15th AIAA/CEAS Aeroacoustics Conference (30th AIAA Aeroacoustics Conference)*, 2009, no. September, pp. 1–22.
- [71] A. Eltawee, M. Wang, D. Kim, F. O. Thomas, and A. V. Kozlov, “Numerical investigation of tandem-cylinder noise reduction using plasma-based flow control,” *J. Fluid Mech.*, vol. 756, pp. 422–451, 2014.
- [72] A. Frendi and Y. Sun, “Noise Radiation from Two Circular Cylinders in Tandem Arrangement Using High-Order Multidomain Spectral Difference Method,” in *15th AIAA/CEAS Aeroacoustics Conference (30th AIAA Aeroacoustics Conference)*, 2009.
- [73] T. Imamura, T. Hirai, S. Enomoto, and K. Yamamoto, “Tandem Cylinder Flow Simulations Using Sixth Order Compact Scheme,” in *17th AIAA/CEAS Aeroacoustics Conference*, 2011.
- [74] D. P. Lockard, M. R. Khorrami, F. Hutcheson, T. F. Brooks, and D. J. Stead, “Tandem Cylinder Noise Predictions,” in *13th AIAA/CEAS Aeroacoustics Conference*, 2007.
- [75] E. Peers, “Physical-Based Aeroacoustic Modelling of Bluff -Bodies,” University of Southampton, 2009.
- [76] M. G. Skopek, M. Braza, Y. Hoarau, and F. Thiele, “Hybrid RANS-LES modeling of a strongly detached turbulent flow around a tandem cylinders configuration,” in *4th Symposium on Hybrid RANS-LES Methods*, 2011, pp. 219–229.
- [77] A. F. Tinetti and M. H. Dunn, “Acoustic Simulations of an Installed Tandem Cylinder Configuration,” in *15th AIAA/CEAS Aeroacoustics Conference (30th AIAA Aeroacoustics Conference)*, 2009.
- [78] F. Vuillot, F. Houssen, E. Manoha, S. Redonnet, and J. Jacob, “Applications of the CEDRE unstructured flow solver to landing gear unsteady flow and noise predictions,” in *17th AIAA/CEAS Aeroacoustics Conference*, 2011.
- [79] M. Weinmann and R. D. Sandberg, “Flow and noise predictions for a tandem cylinder configuration using novel hybrid RANS / LES approaches,” in *16th*

- AIAA/CEAS Aeroacoustics Conference*, 2010.
- [80] M. Weinmann, R. D. Sandberg, and C. Doolan, “Tandem cylinder flow and noise predictions using a hybrid RANS/LES approach,” *Int. J. Heat Fluid Flow*, vol. 50, pp. 263–278, 2014.
  - [81] Z. Xiao, J. Liu, J. Huang, and S. Fu, “Numerical Dissipation Effects on Massive Separation Around Tandem Cylinders,” *AIAA J.*, vol. 50, no. 5, pp. 1119–1136, 2012.
  - [82] Z. Xiao and K. Luo, “Improved delayed detached-eddy simulation of massive separation around triple cylinders,” *Acta Mech. Sin.*, vol. 31, no. 6, pp. 799–816, 2015.
  - [83] Z. Xiao and K. Luo, “Numerical Simulations of Tandem Cylinders with Subcritical Spacing,” in *19th AIAA/CEAS Aeroacoustics Conference*, 2013.
  - [84] Z. Xiao and K. Luo, “Numerical Simulations of the Near-field Flows past Cylinders in Tandem Arrangements,” in *51st AIAA Aerospace Sciences Meeting including the New Horizons Forum and Aerospace Exposition*, 2013.
  - [85] Y. Zhang, W. G. Habashi, and R. A. Khurram, “Zonal Detached-Eddy Simulation of Turbulent Unsteady Flow over Iced Airfoils,” *J. Aircr.*, vol. 53, no. 1, pp. 168–181, 2016.
  - [86] K. Frendi, M. Zreik, and A. Tosh, “A Computational Study of the Unsteady Flow Past Tandem Cylinders,” in *36th AIAA Fluid Dynamics Conference and Exhibit*, 2006.
  - [87] S. Freudiger, J. Hegewald, and M. Krafczuk, “A parallelisation concept for multi-physics lattice Boltzmann prototype based on hierarchical grids,” *Prog. Comput. Fluid Dyn.*, vol. 8, no. 1–4, pp. 168–178, 2008.
  - [88] M. R. Khorrami, M. Choudhari, D. P. Lockard, L. N. Jenkins, and C. B. McGinley, “Unsteady Flowfield Around Tandem Cylinders as Prototype Component Interaction in Airframe Noise,” *AIAA J.*, vol. 45, no. 8, pp. 1930–1941, 2007.
  - [89] R. Maduta, “An eddy-resolving Reynolds stress model for unsteady flow computations: development and application,” Technischen Universitat Darmstadt, 2013.
  - [90] B. Sainte-Rose, O. Allain, C. Leca, and A. Dervieux, “A Study of LES Models for the Simulation of a Turbulent Flow Around Supercritical Tandem Cylinders,” in *ASME 33rd International Conference on Ocean, Offshore, and Arctic Engineering*, 2014.
  - [91] R. Satti, Y. Li, R. Shock, and S. Noelting, “Unsteady flow predictions around tandem cylinders with sub-critical spacing,” in *49th AIAA Aerospace Sciences Meeting Including the New Horizons Forum and Aerospace Exposition*, 2011.
  - [92] E. F. Sheta, A. Tosh, S. D. Habchi, and A. Frendi, “Wavelet-Based Adaptive Multiresolution Methodology For Tandem Cylinder Noise,” in *36th AIAA Fluid Dynamics Conference and Exhibit*, 2006.
  - [93] A. Uzun and M. Yousuff Hussaini, “An application of delayed detached eddy simulation to tandem cylinder flow field prediction,” *Comput. Fluids*, vol. 60, pp. 71–85, 2012.
  - [94] D. P. Lockard, “Summary of the Tandem Cylinder Solutions from the Benchmark problems for Airframe Noise Computations-I Workshop,” in *49th AIAA Aerospace Sciences Meeting including the New Horizons Forum and Aerospace Exposition*,

- 2011.
- [95] Z. Xiao, J. Liu, J. Huang, and S. Fu, “Comparisons of Three Improved DES Methods on Unsteady Flows Past Tandem Cylinders \*,” in *4th Symposium on Hybrid RANS-LES Methods*, 2012, pp. 231–243.
  - [96] J. H. Dittmar and D. J. Leciejewski, “An Experimental Investigation of the Effect of Boundary Layer Refraction on the Noise from a High Speed Propeller,” 1984.
  - [97] D. B. Hanson and M. R. Fink, “The importance of quadrupole sources in prediction of transonic tip speed propeller noise,” *J. Sound Vib.*, vol. 62, no. 1, pp. 19–38, 1979.
  - [98] S. V. Patankar and D. B. Spalding, “A Calculation Procedure for Heat, Mass, and Momentum Transfer in Three-Dimensional Parabolic Flows,” *Int. J. Heat Transf.*, vol. 15, pp. 1787–1806, 1972.
  - [99] A. Jameson, “Time Dependent Calculations Using Multigrid, with Applications to Unsteady Flows Past Airfoils and Wings,” *AIAA paper*, vol. 1596, no. AIAA-91–1596, p. 1991, 1991.
  - [100] R. H. Nichols, “Turbulence models and their application to complex flows,” *Univ. Alabama Birmingham*, 2001.
  - [101] J. Boussinesq, “Essai sur la théorie des eaux courantes,” *Mémoires présentés par Divers savants à l'Académie des Sci.*, vol. 23, no. 1, pp. 1–680, 1877.
  - [102] F. R. Menter, “Two-equation eddy-viscosity turbulence modeling for engineering applications,” *AIAA J.*, vol. 32, no. 8, pp. 1598–1605, 1994.
  - [103] M. S. Liou, “A Sequel to AUSM: AUSM+,” *J. Comput. Phys.*, vol. 129, pp. 364–382, 1996.
  - [104] *STAR CCM+ User Guide*, 11.04 ed. CD-adapco, 2016.
  - [105] M. J. Lighthill, “On Sound Generated Aerodynamically. II. Turbulence as a Source of Sound,” *Proc. R. Soc. London A Math. Phys. Eng. Sci.*, vol. 222, no. 1148, pp. 1–32, Feb. 1954.
  - [106] J. E. Ffowcs Williams and D. L. Hawkings, “Sound Generation by Turbulence and Surfaces in Arbitrary Motion,” *Philos. Trans. R. Soc. London*, vol. A264, pp. 321–342, 1969.
  - [107] F. Farassat, “Derivation of Formulations 1 and 1A of Farassat,” *NASA TM 214852*, pp. 1–25, 2007.
  - [108] W. Johnson, “Rotorcraft Aerodynamics Models for a Comprehensive Analysis,” in *American Helicopter Society 54th Annual Forum*, 1998.
  - [109] D. A. Wachspress, T. R. Quackenbush, and A. H. Boschitsch, “Rotorcraft Inerntional Aerodynamics Calculations with Fast Vortex/Panel Methods,” in *American Helicopter Society 56th Annual Forum*, 2000.
  - [110] J. G. Leishman, “Principles of Helicopter Aerodynamics.” p. 4, 2006.
  - [111] S. G. Voutsinas, “A GENeralized Unsteady Vortex Partical Method for Solving the Unsteady Flow around Multi-component Configurations,” National Technical University of Athens, Greece, 1990.
  - [112] S. G. Voutsinas, M. A. Belissis, and K. G. Rados, “Investigation of the Yawed Operation of Wind Turbines by Means of a Vortex Particle Method,” in *FDP Symposium on Aerodynamics and Aeroacoustics of Rotorcraft (AGARD CP552)*, 1995.
  - [113] S. G. Voutsinas and D. G. Triantos, “High-resolution Aerodynamic Analysis of

- Full Helicopter Configurations,” in *25th European Rotorcraft Forum*, 1999.
- [114] S. G. Voutsinas and D. G. Triantos, “Aeroacoustics of Full Helicopter Configurations using Vortex Particle Flow Approximations,” in *CEAS Forum on Aeroacoustics of Rotors and Propellers*, 1999.
- [115] S. McTavish, “Advanced Aeroelastic Simulations for Practical Fixed-wing and Rotary-wing Applications,” Carleton University, 2008.
- [116] D. G. Opoku, “Aeroelastic and Aeroacoustic Modelling of Rotorcraft,” Carleton University, 2002.
- [117] T. Cheng, “Structural Dynamics Modeling of Helicopter Blades for Computational Aeroelasticity,” pp. 1–180, 2002.
- [118] M. G. Martin, “Articulated Rotor Hub Model for 3D Aeroelastic Simulation of Helicopter Rotors,” Carleton University, 2011.
- [119] D. G. Triantos, “Aerodynamic and Aeroacoustic Analysis of Helicopter Rotors,” National Technical University of Athens, 2002.
- [120] J. L. Hess and A. M. O. Smith, “Calculation of Non-Lifting Potential Flow About Arbitrary Three-Dimensional Boundaries,” 1962.
- [121] J. L. Hess, “Calculation of Potential Flow About Arbitrary Three-Dimensional Lifting Bodies,” 1972.
- [122] J. T. Beale and A. Majda, “High Order Accurate Vortex Methods with Explicit Velocity Kernels,” *J. Comput. Phys.*, vol. 58, pp. 188–208, 1985.
- [123] J. T. Beale and A. Majda, “Vortex Methods 1: Convergence in Three Dimensions,” *Math. Comput.*, vol. 39, no. 159, pp. 1–27, 1982.
- [124] C. Penny, “Personal Communication.”
- [125] J. Wiebe, “Development of a Simulation and Optimization Framework for Improved Aerodynamic Performance of R/C Helicopter Rotor Blades,” Carleton University, 2015.
- [126] E. Y. Yudin, “On the Vortex Sound from Rotating Rods,” *NACA TM 11*, vol. 14, no. 9, 1947.
- [127] Y. Suzuki and H. Takeshima, “Equal-loudness-level contours for pure tones.,” *J. Acoust. Soc. Am.*, vol. 116, no. 2, pp. 918–933, 2004.
- [128] I. J. Sharland and J. W. Leverton, “Propeller and Helicopter and Hovercraft Noise,” in *Noise and Acoustic Fatigue in Aeronautics*, 1968, p. 188.

## Appendix A: Geometry Definition Used for SR-2 Propeller in SmartRotor Code

This section describes the geometrical inputs into the SmartRotor code. Because both of the propeller tests utilized the SR-2 propeller, the same input is used for both test cases with a different definition of diameter, root pitch angle, and the number of blades. A root cutout of 24% of the span of the propeller was used

**Table A.1: Geometrical Inputs of SR-2 Propeller Into SmartRotor**

<b>Pitch Distribution</b>		<b>Chord Distribution</b>		<b>Airfoil Distribution</b>	
Spanwise Position (%)	Pitch Angle (degree)	Spanwise Position (%)	Chord/Diameter	Spanwise Position (%)	Airfoil
0.0%	23.7	0.0%	0.151	0.0%	NACA 65-(-2.2)20
24.0%	23.7	24.0%	0.151	24.0%	NACA 65-(-2.2)20
25.0%	21.3	30.0%	0.152	25.0%	NACA65-(-2)15
27.5%	18.6	40.0%	0.152	27.5%	NACA65-010
30.0%	16.6	50.0%	0.152	30.0%	NACA65 -107
35.0%	13.6	60.0%	0.152	35.0%	NACA 16-105
40.0%	11.8	70.0%	0.149	40.0%	NACA 16-203
50.0%	8.5	75.0%	0.148	50.0%	NACA 16-203
60.0%	5.0	80.0%	0.145	60.0%	NACA 16-203
70.0%	1.7	85.0%	0.140	70.0%	NACA 16-102
80.0%	-1.7	90.0%	0.133	80.0%	NACA 16-102
90.0%	-4.6	92.5%	0.127	90.0%	NACA 16-002
100.0%	-6.8	95.0%	0.117	100.0%	NACA 16-002
		97.5%	0.103		
		99.0%	0.087		
		100.0%	0.053		

## Appendix B: SR-2 Validation Data for SR-2 Test Case 2

This appendix presents additional data which was obtained in the validation case of the SR-2 propeller in cruise condition. Data listed are from transducers 3-5 and 7-11.

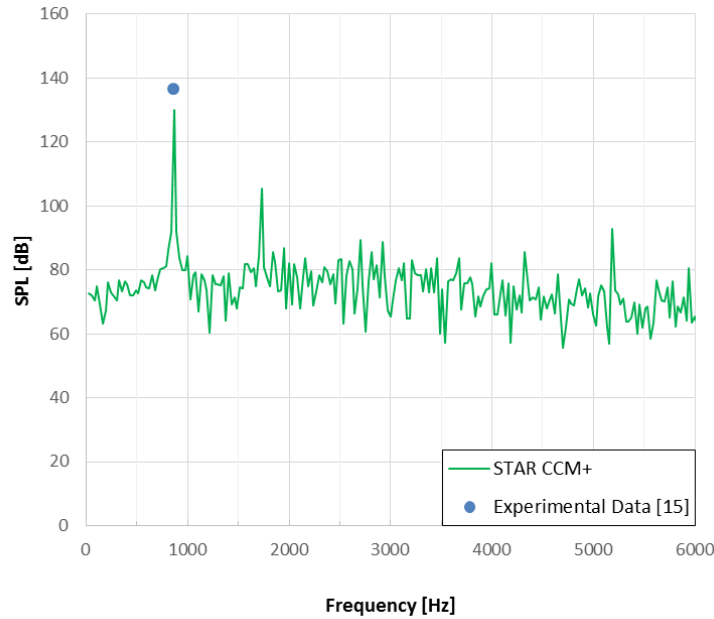


**Fig. B.1:** Noise at transducer 3 predicted in STAR CCM+ from an impermeable FW-H surface.

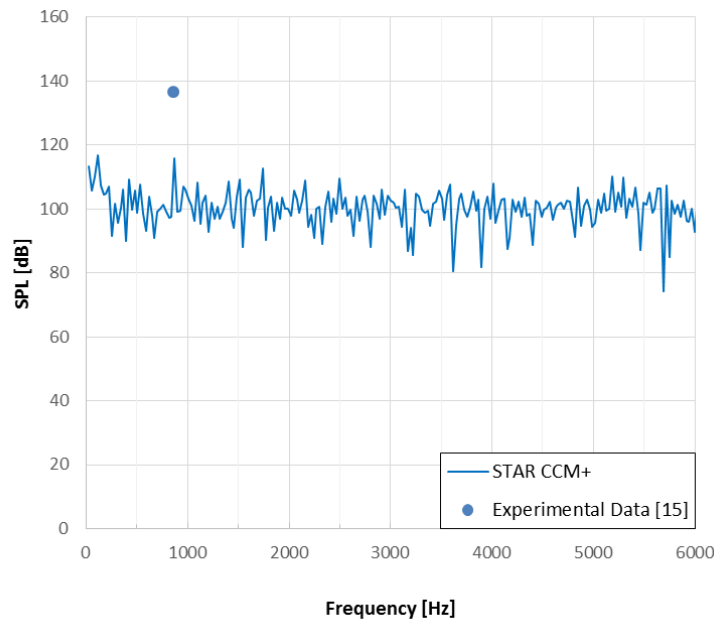


**Fig. B.2:** Noise at transducer 3 predicted in STAR CCM+ from a permeable FW-H surface.

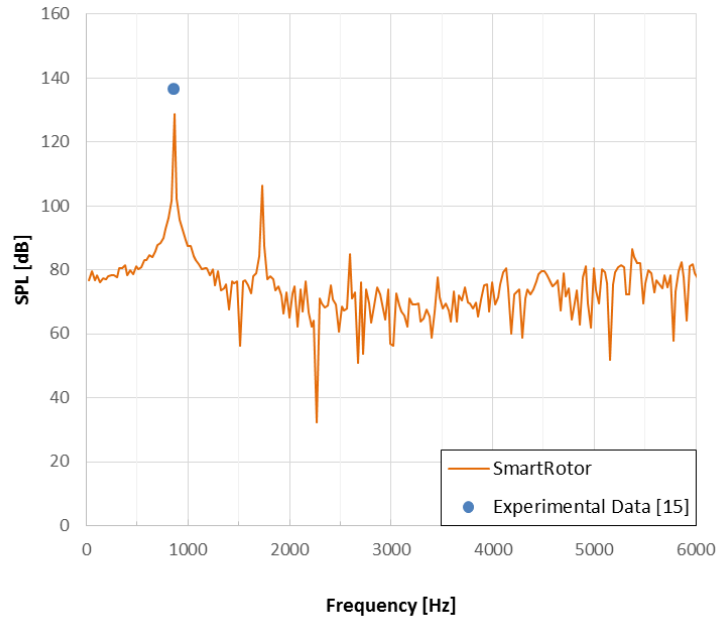


**Fig. B.3:** Noise at transducer 3 predicted in SmartRotor.

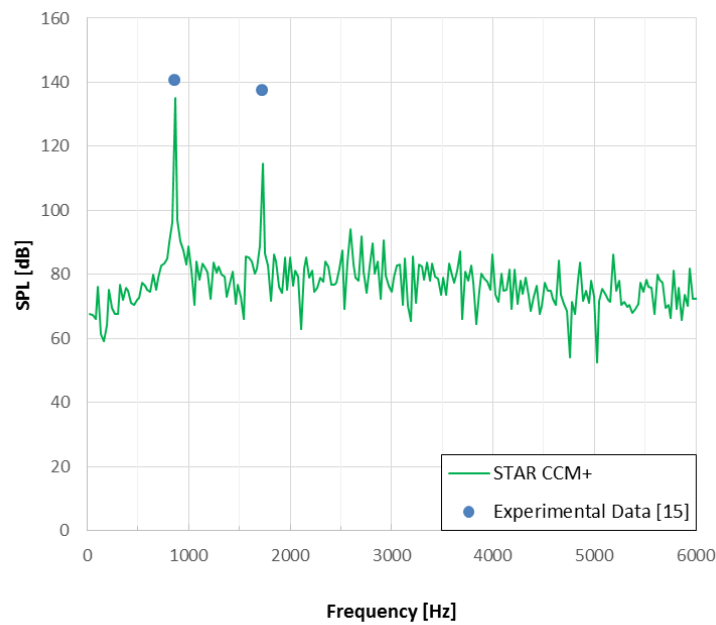


**Fig. B.4:** Noise at transducer 4 predicted in STAR CCM+ from an impermeable FW-H surface.

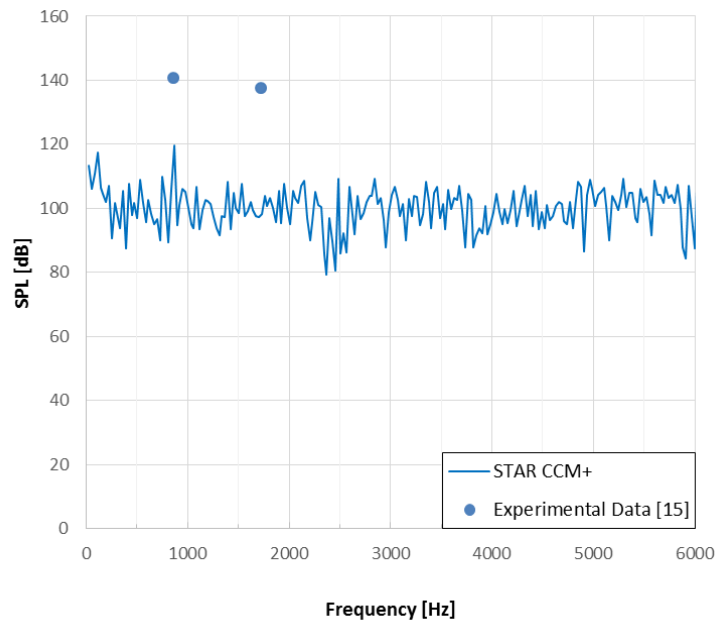


**Fig. B.5:** Noise at transducer 4 predicted in STAR CCM+ from a permeable FW-H surface.

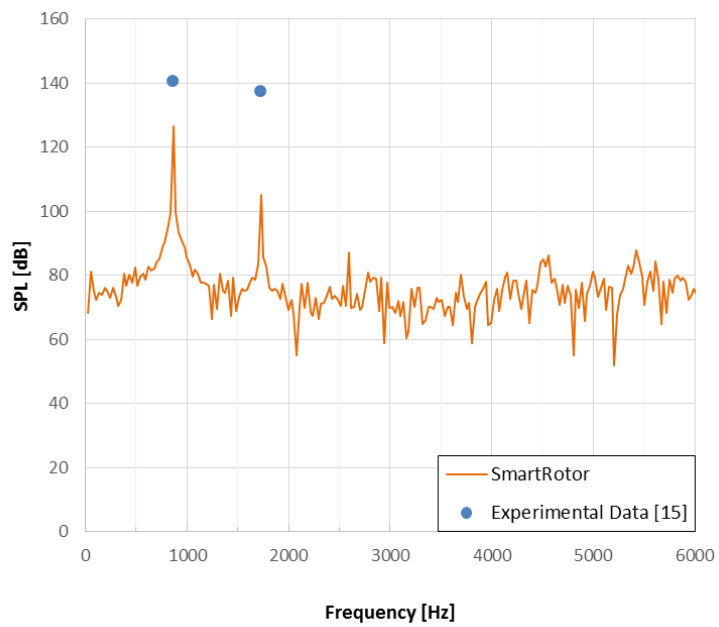


**Fig. B.6:** Noise at transducer 4 predicted in SmartRotor.

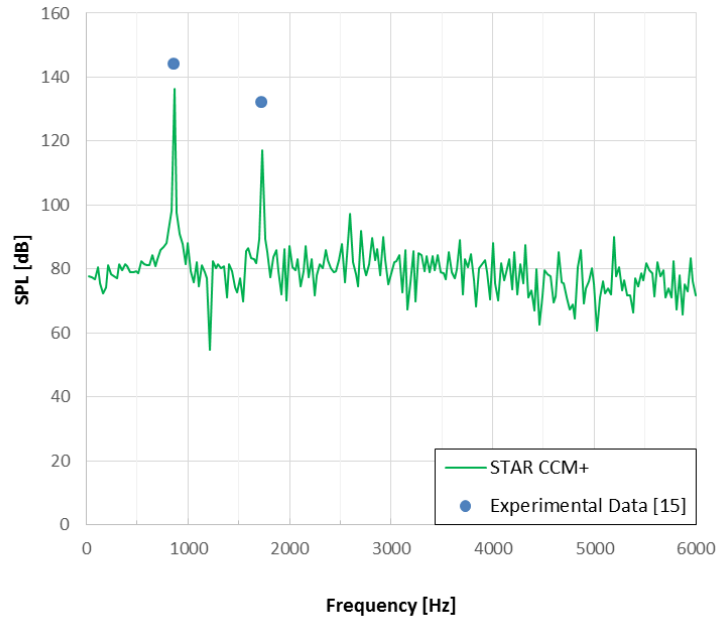


**Fig. B.7:** Noise at transducer 5 predicted in STAR CCM+ from an impermeable FW-H surface.

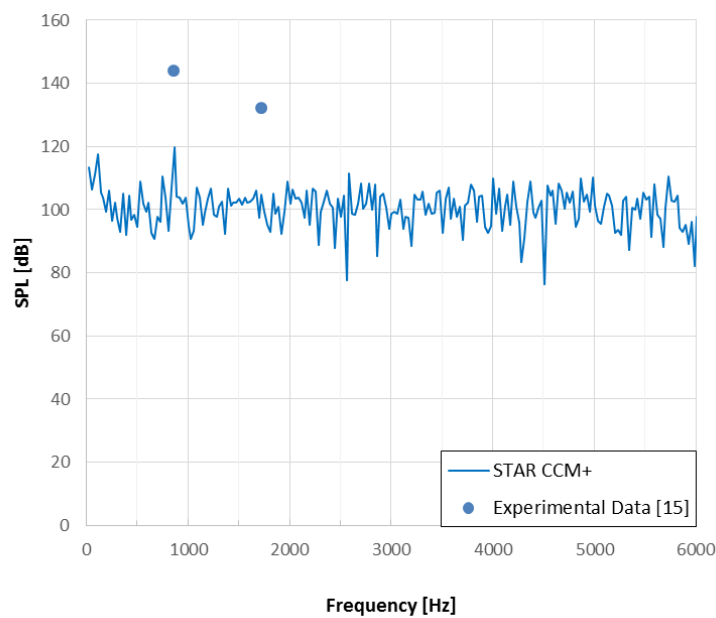


**Fig. B.8:** Noise at transducer 5 predicted in STAR CCM+ from a permeable FW-H surface.

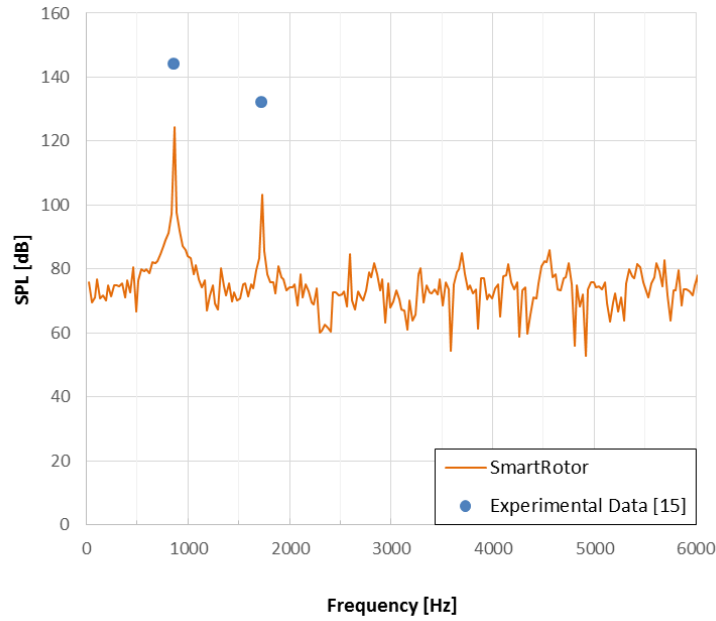


**Fig. B.9: Noise at transducer 5 predicted in SmartRotor.**

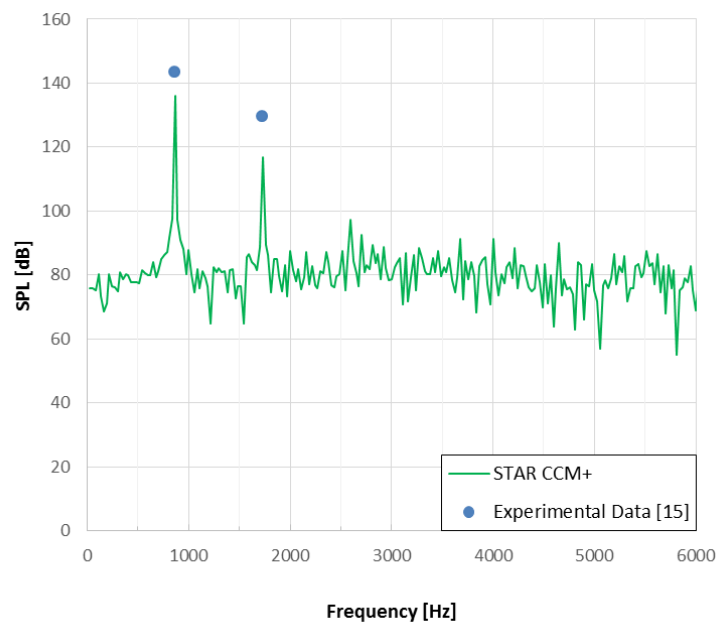


**Fig. B.10: Noise at transducer 7 predicted in STAR CCM+ from an impermeable FW-H surface.**

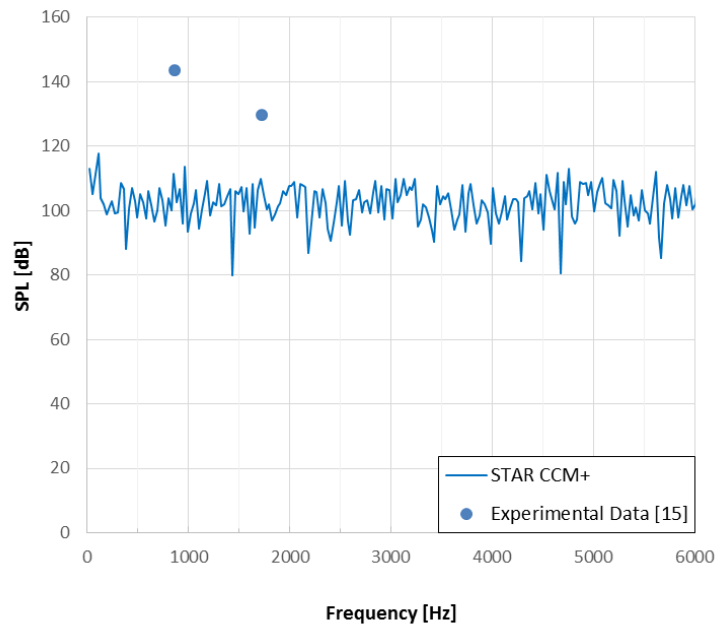


**Fig. B.11:** Noise at transducer 7 predicted in STAR CCM+ from a permeable FW-H surface.

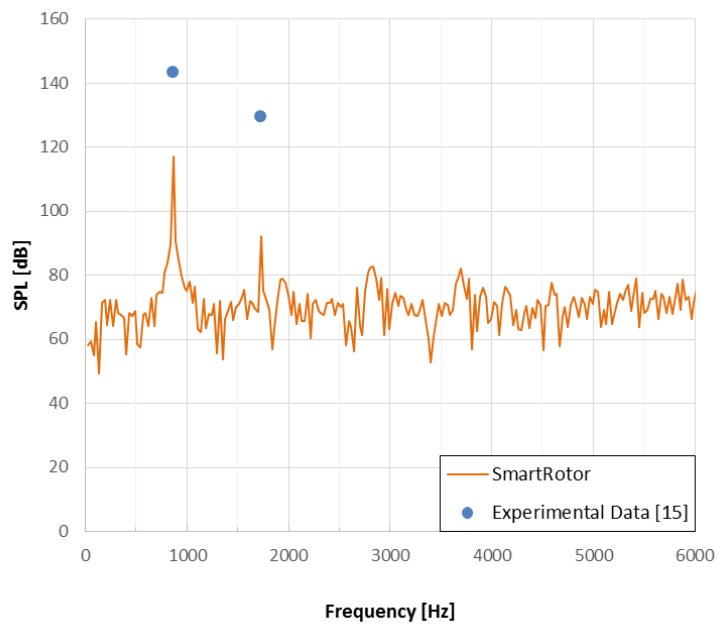


**Fig. B.12:** Noise at transducer 7 predicted in SmartRotor.

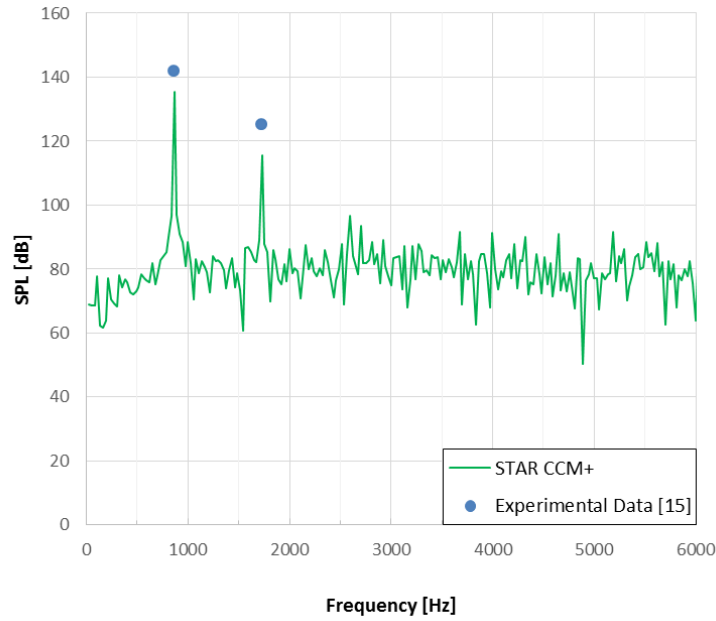


**Fig. B.13:** Noise at transducer 8 predicted in STAR CCM+ from an impermeable FW-H surface.

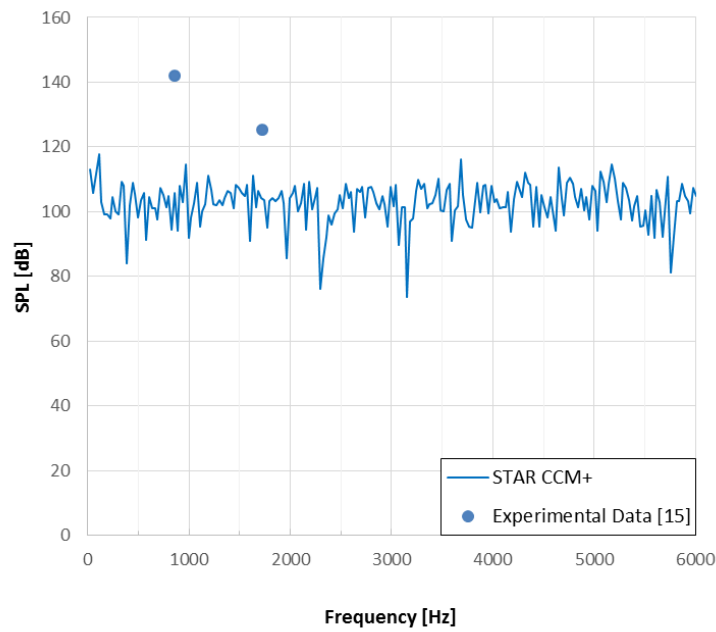


**Fig. B.14:** Noise at transducer 8 predicted in STAR CCM+ from a permeable FW-H surface.

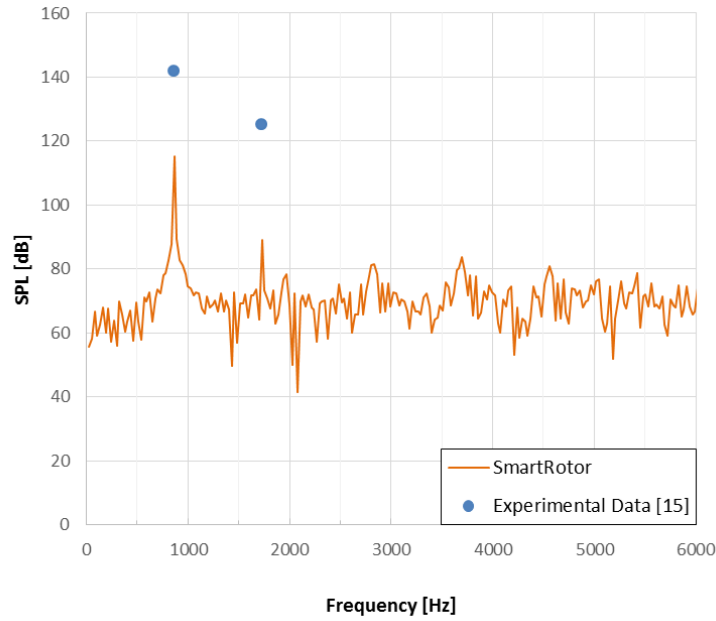


**Fig. B.15:** Noise at transducer 8 predicted in SmartRotor.

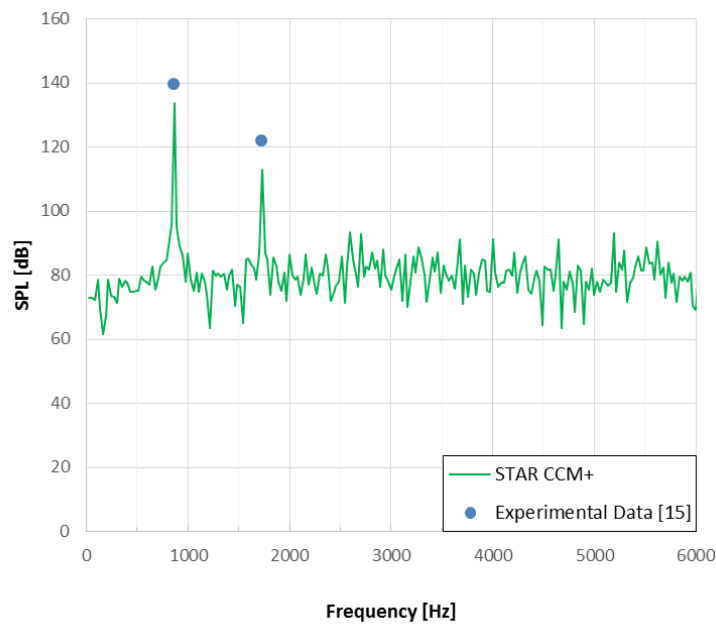


**Fig. B.16:** Noise at transducer 9 predicted in STAR CCM+ from an impermeable FW-H surface.

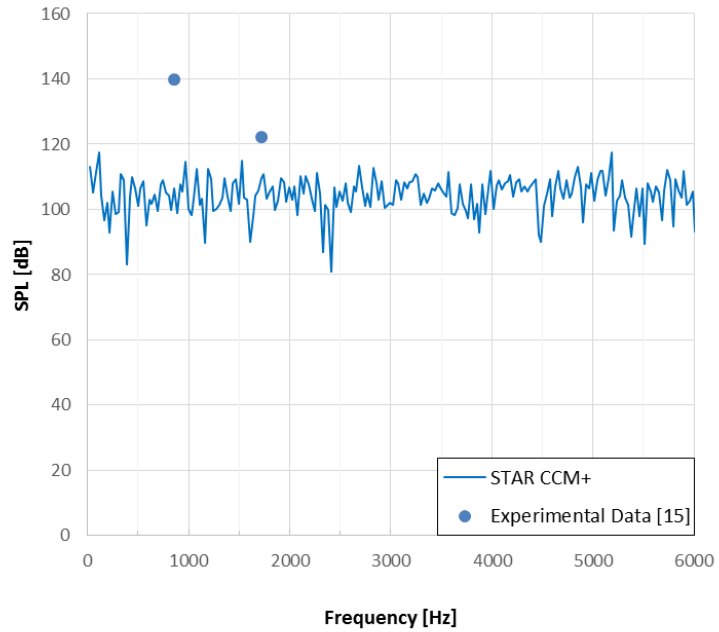


**Fig. B.17:** Noise at transducer 9 predicted in STAR CCM+ from a permeable FW-H surface.

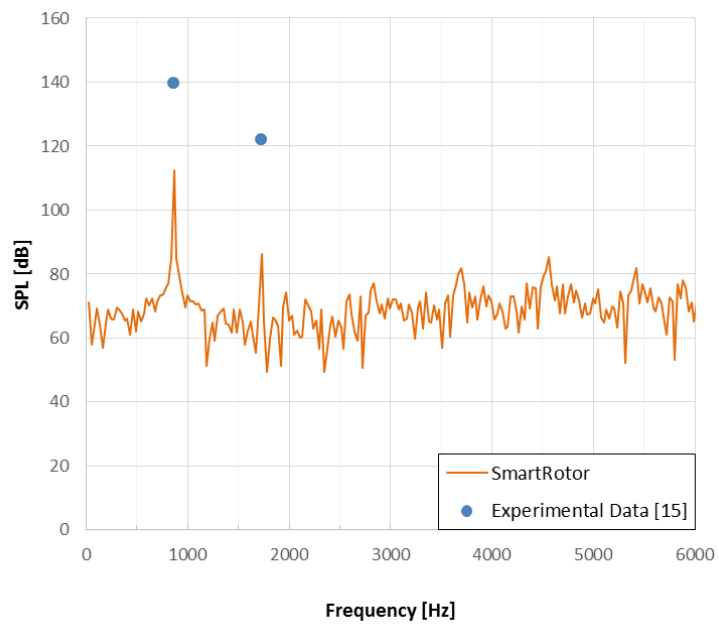


**Fig. B.18:** Noise at transducer 9 predicted in SmartRotor.

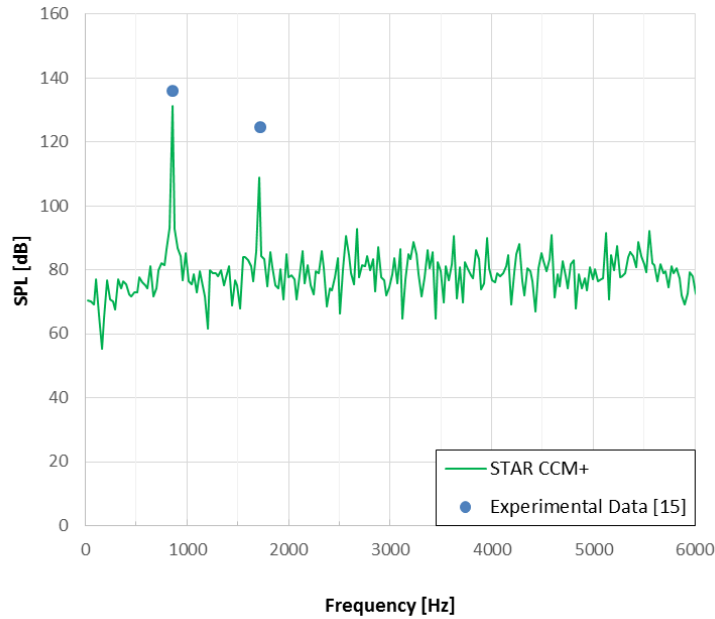


**Fig. B.19:** Noise at transducer 10 predicted in STAR CCM+ from an impermeable FW-H surface.

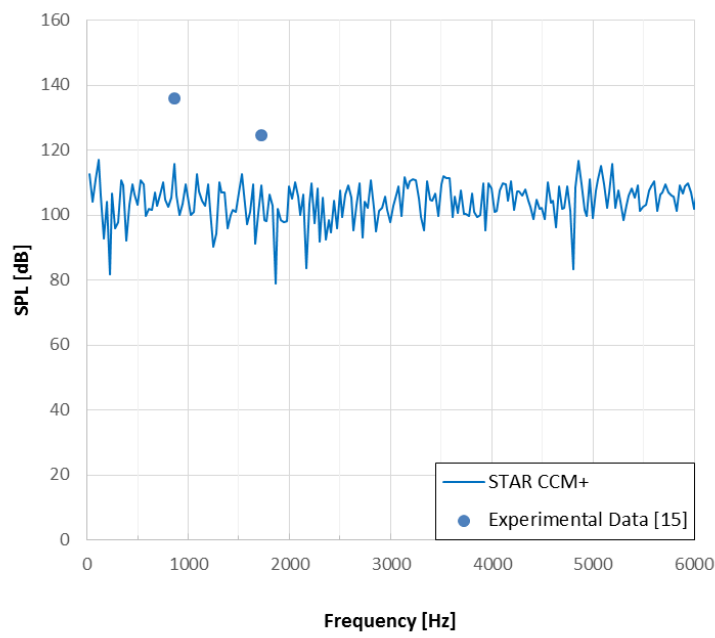


**Fig. B.20:** Noise at transducer 10 predicted in STAR CCM+ from a permeable FW-H surface.

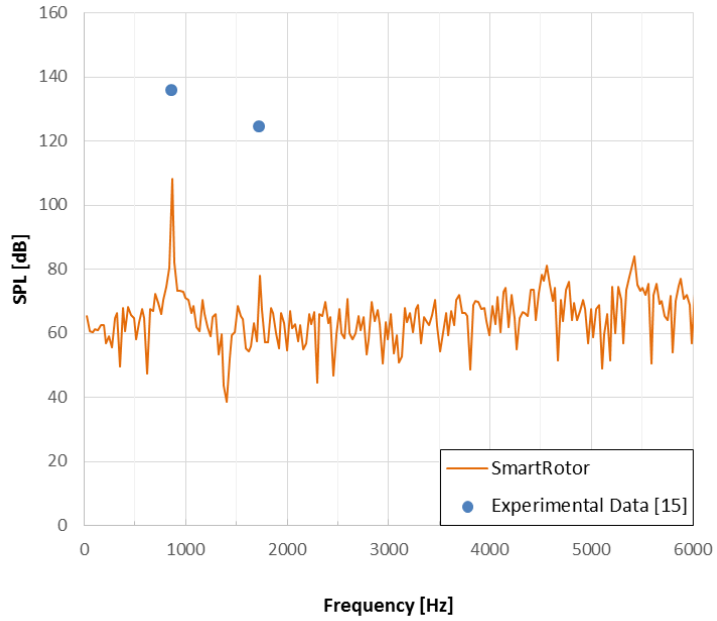


**Fig. B.21:** Noise at transducer 10 predicted in SmartRotor.

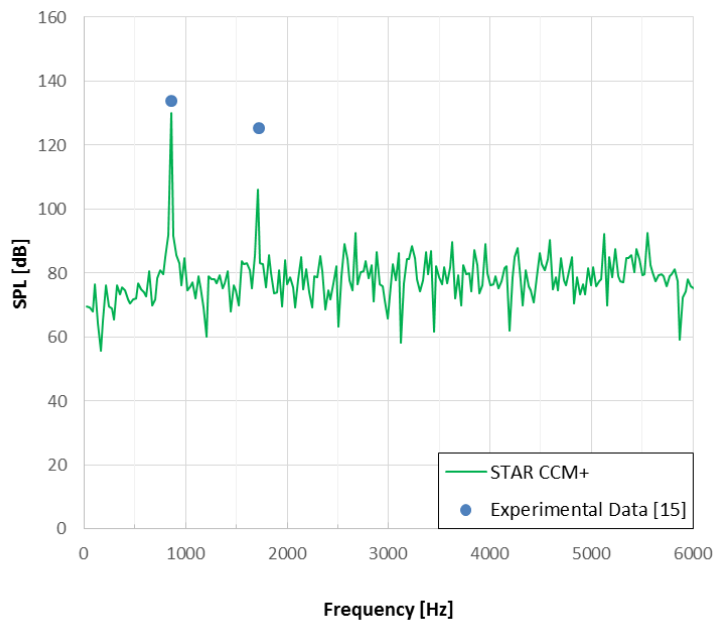


**Fig. B.22:** Noise at transducer 11 predicted in STAR CCM+ from an impermeable FW-H surface.

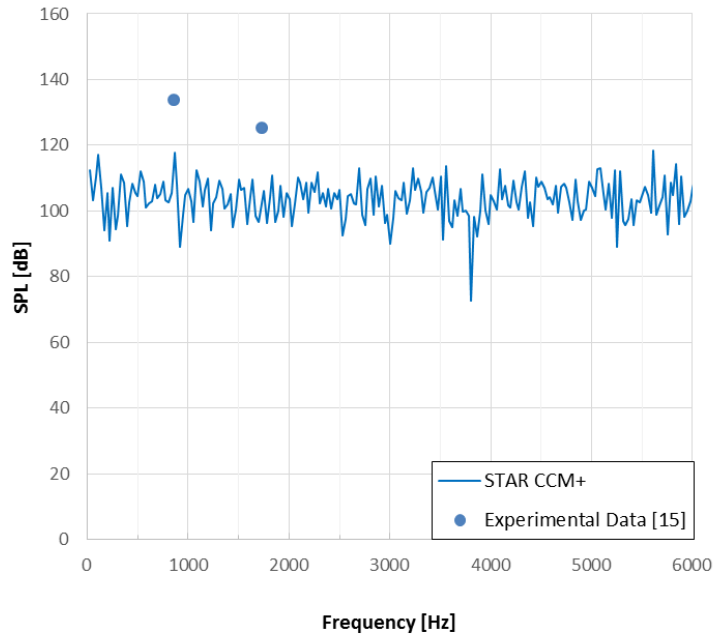


**Fig. B.23:** Noise at transducer 11 predicted in STAR CCM+ from a permeable FW-H surface.

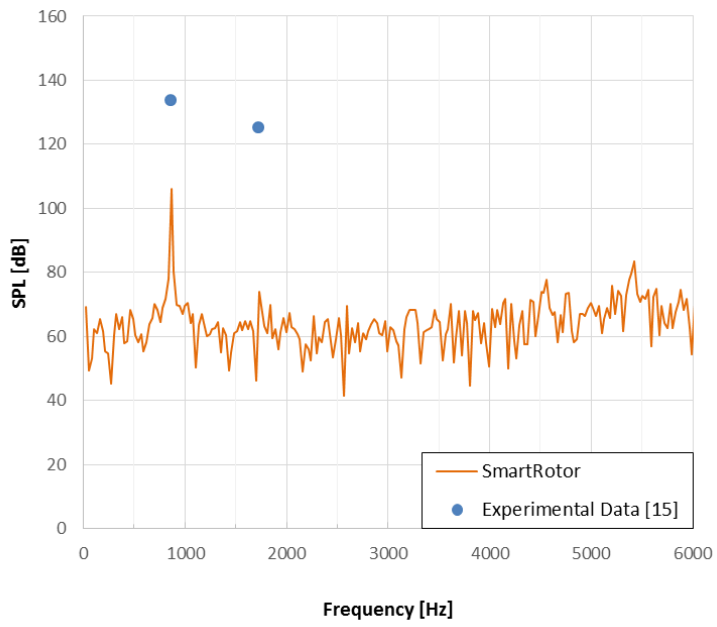


**Fig. B.24:** Noise at transducer 11 predicted in SmartRotor.

## Appendix C: Airfoil Data Used for Aerodynamic Input in SmartRotor

This appendix supplies the airfoil curves used to simulate the SR-2 propellers in this thesis.

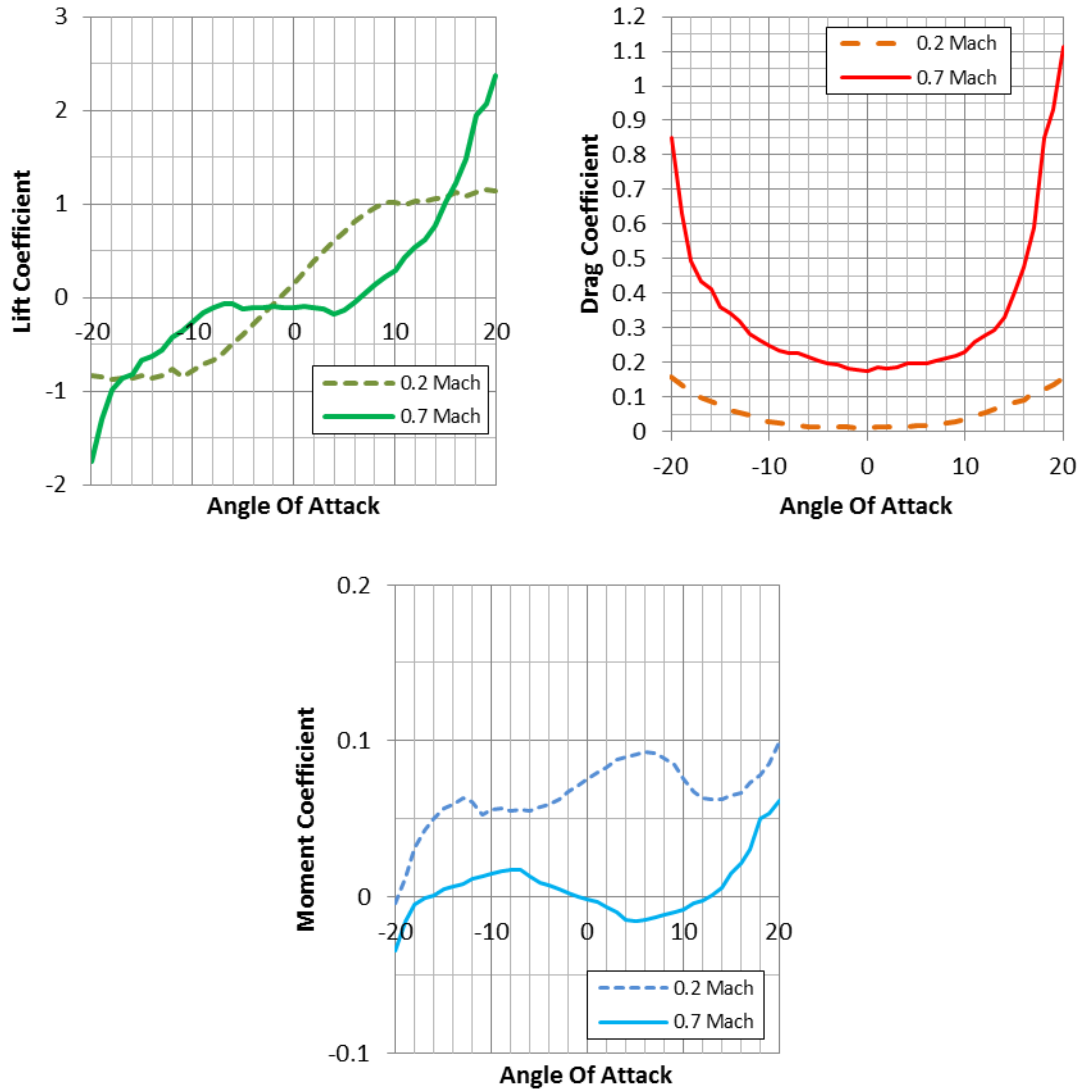
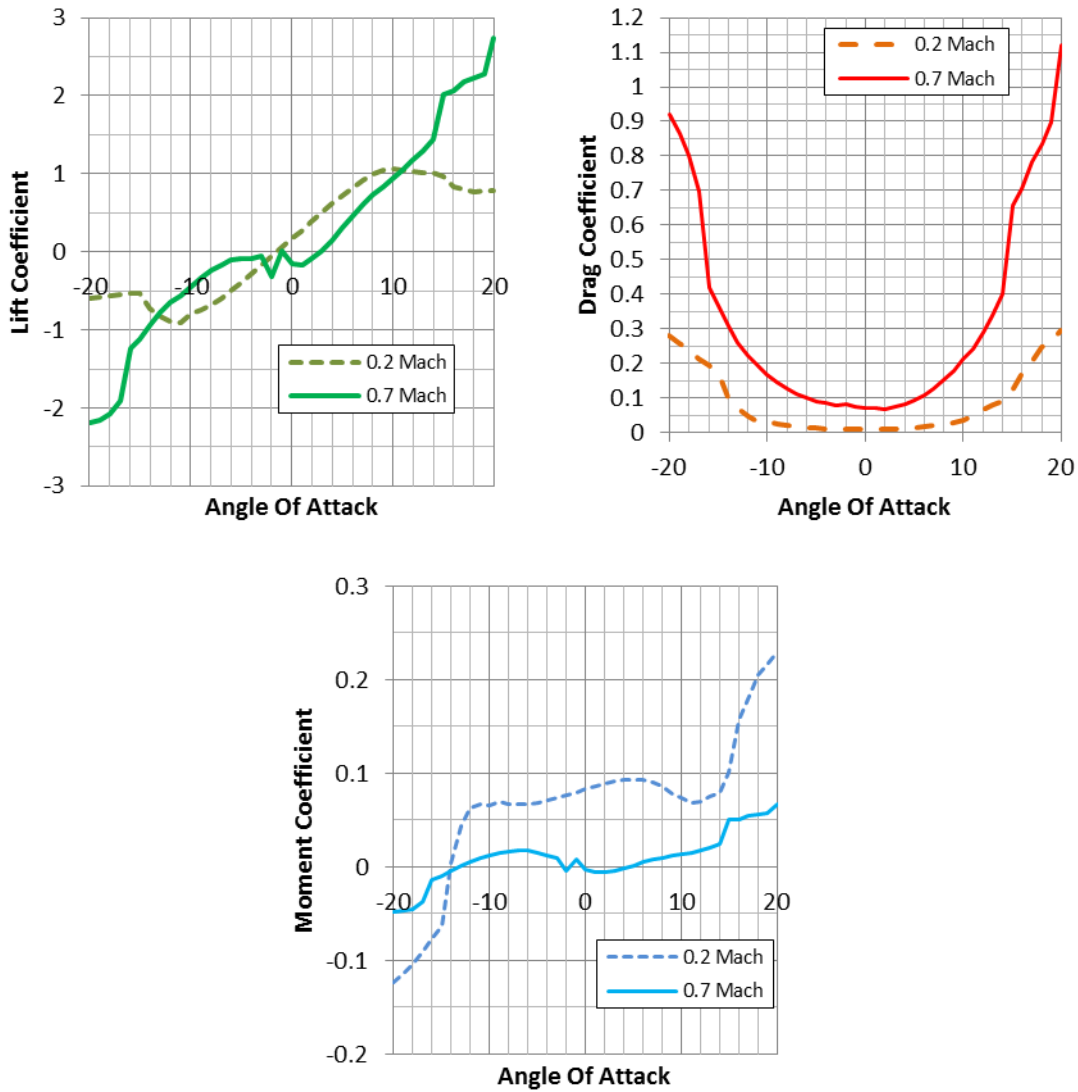


Fig. C.1: Lift (Top Left), Drag (Top Right), and Moment (Bottom) Coefficient Curves for the NACA 65-(2.2) 20 Airfoil.



**Fig. C.2: Lift (Top Left), Drag (Top Right), and Moment (Bottom) Coefficient Curves for the NACA 65-(-2) 15 Airfoil.**

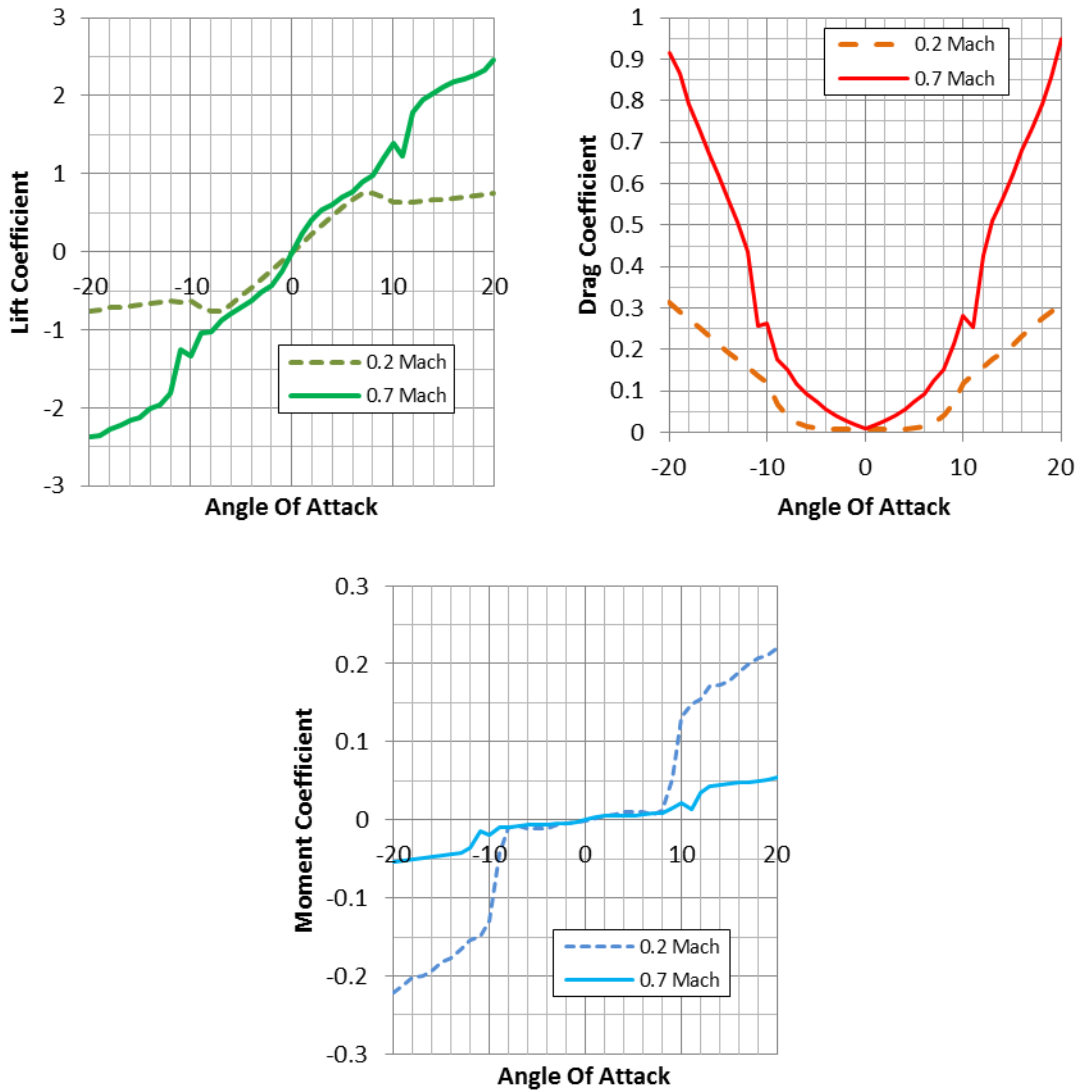


Fig. C.3: Lift (Top Left), Drag (Top Right), and Moment (Bottom) Coefficient Curves for the NACA 65-010 Airfoil.

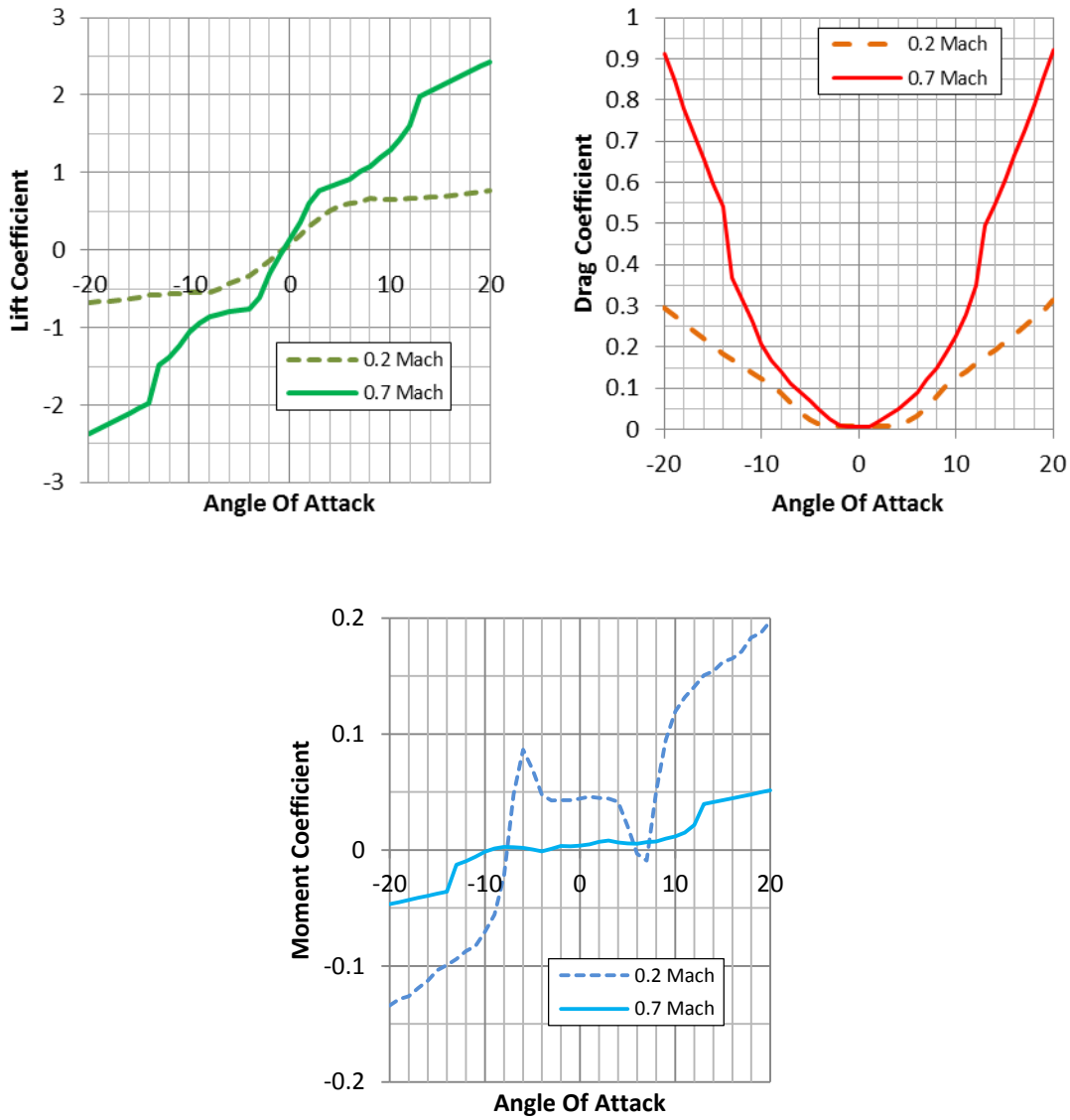
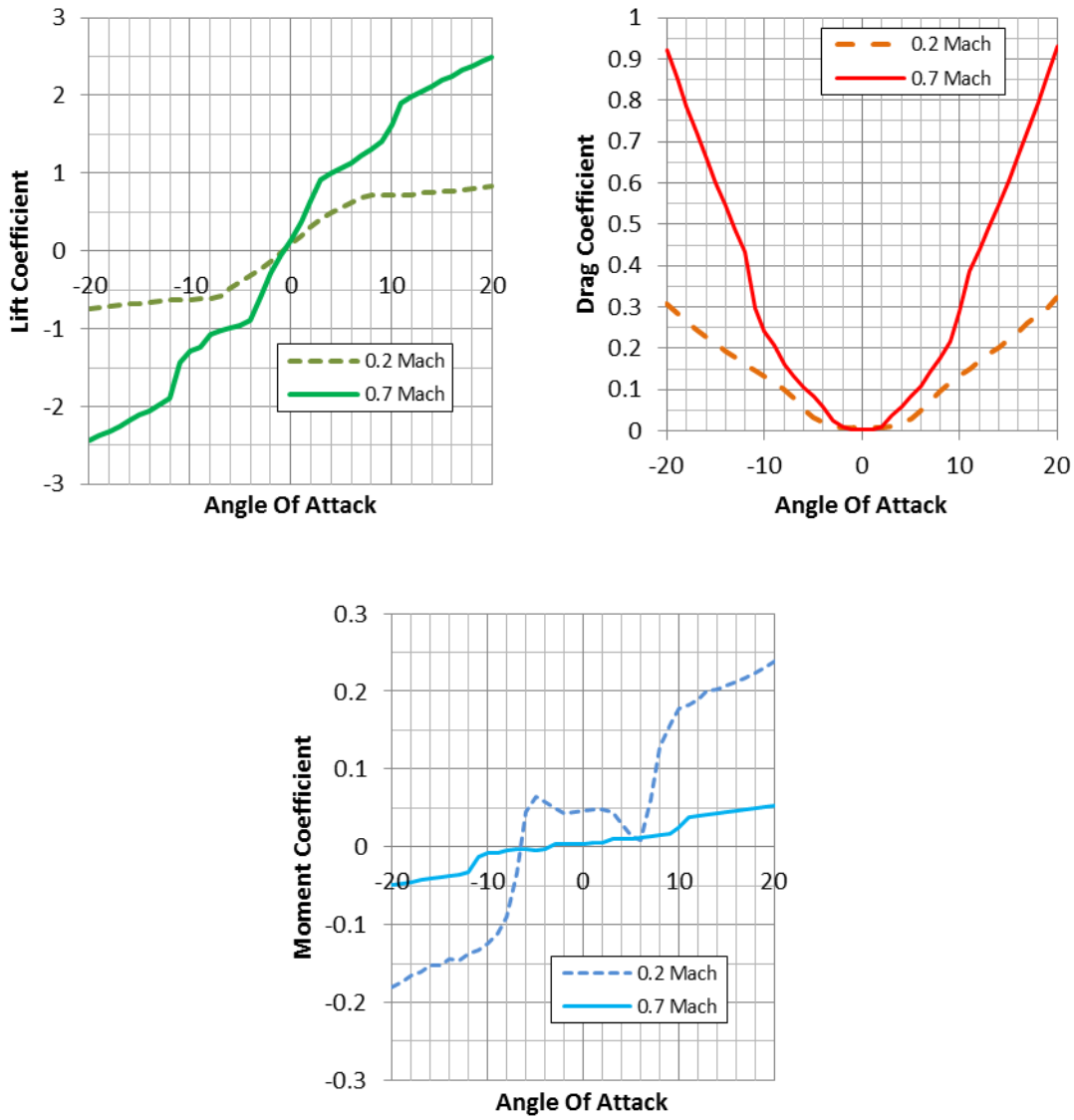
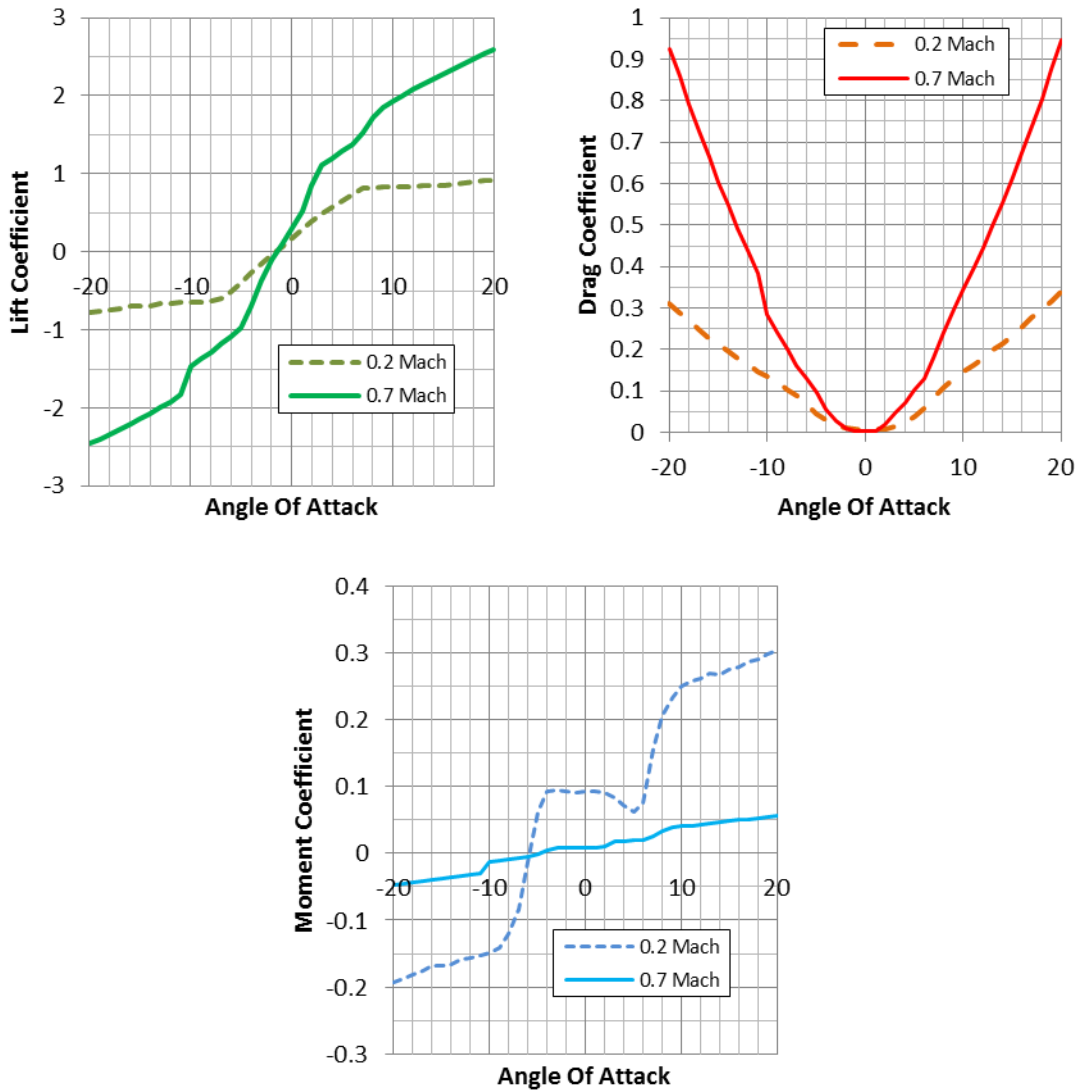


Fig. C.4: Lift (Top Left), Drag (Top Right), and Moment (Bottom) Coefficient Curves for the NACA 65-107 Airfoil.

65-107 Airfoil.



**Fig. C.5: Lift (Top Left), Drag (Top Right), and Moment (Bottom) Coefficient Curves for the NACA 16-105 Airfoil.**



**Fig. C.6: Lift (Top Left), Drag (Top Right), and Moment (Bottom) Coefficient Curves for the NACA 16-203 Airfoil.**

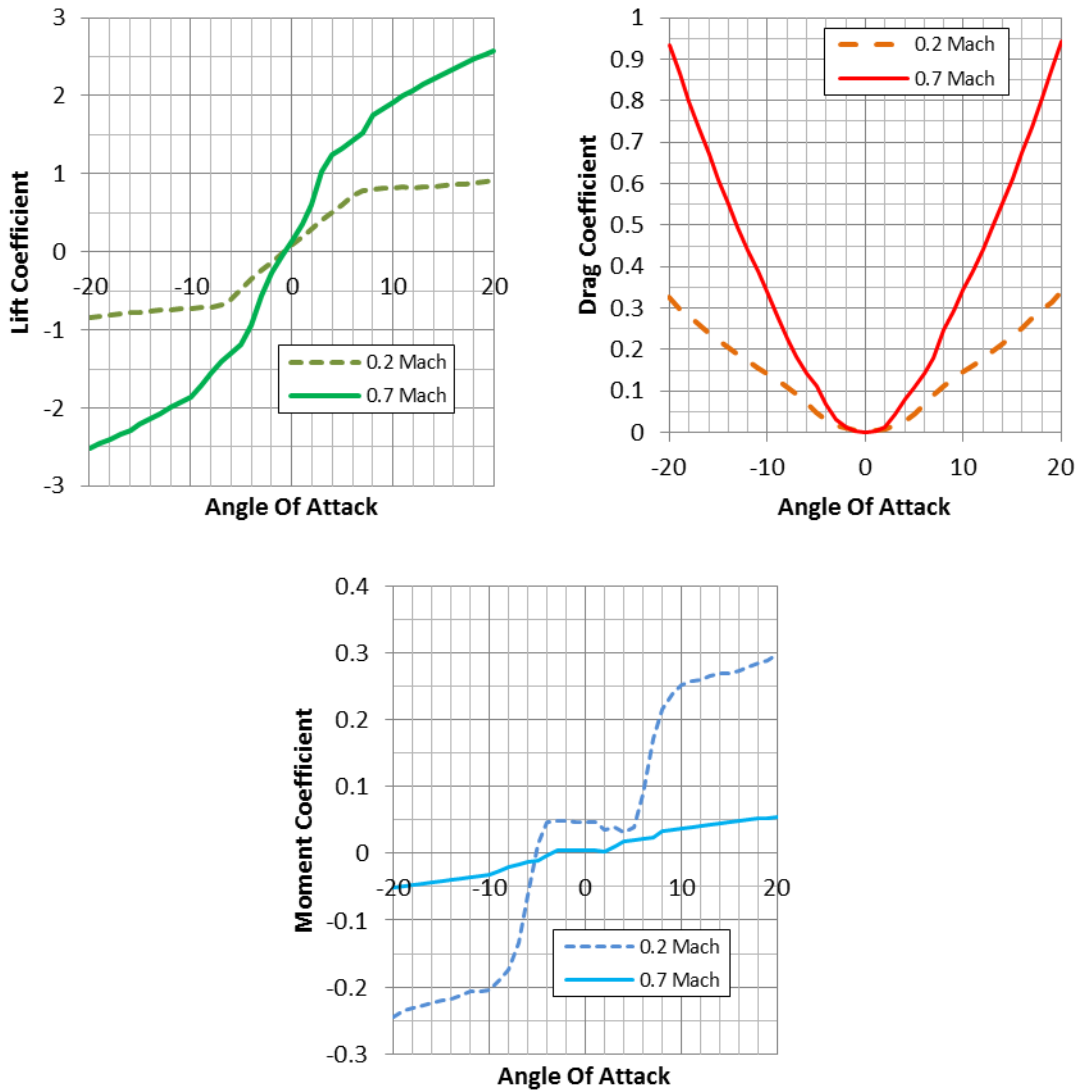


**Fig. C.7: Lift (Top Left), Drag (Top Right), and Moment (Bottom) Coefficient Curves for the NACA 16-102 Airfoil.**

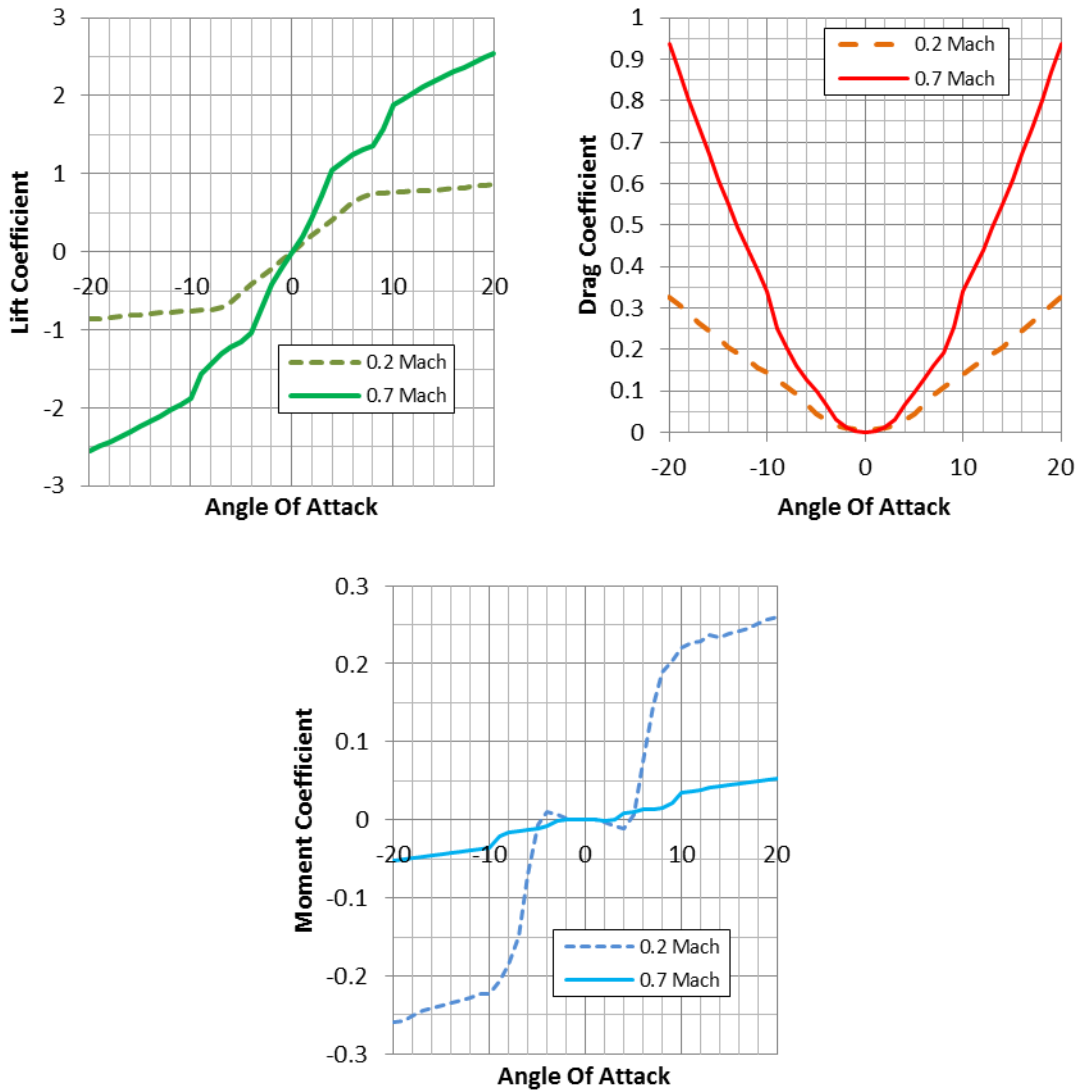


**Fig. C.8: Lift (Top Left), Drag (Top Right), and Moment (Bottom) Coefficient Curves for the NACA 16-002 Airfoil.**